Electrical Characterisation of particle irradiated 4H-SiC

By

Alexander Tapera Paradzah

University of Pretoria

Submitted in partial fulfilment of the requirements of the degree

Magister Scientiae

In the Faculty of Natural and Agricultural Science at the University of Pretoria

Supervisor / Promoter: Prof. F. D. Auret

Co-Supervisor: Dr M. M. Diale

JANUARY 2014

Electrical Characterisation of particle irradiated 4H-SiC

By

Alexander Tapera Paradzah

*Submitted in partial fulfilment of the requirements of the degree **Magister Scientiae** in the Faculty of Natural and Agricultural Science at the University of Pretoria*

Supervisor / Promoter: Prof. F. D. Auret

Co-Supervisor: Dr M. M. Diale

Silicon Carbide is a wide bandgap semiconductor with excellent physical and opto-electrical properties. Among these excellent properties are its radiation hardness, high temperature operation and high electric field breakdown. SiC can therefore be used in the fabrication of electronic devices capable of operating in harsh environments, e.g. radiation detectors. Like any other semiconductor, the success of SiC in device fabrication depends on elimination of defects that are detrimental to desired devices or controlled introduction of desired energy levels. The first step in so doing is understanding the defects that are either found in as grown material, introduced during device fabrication or introduced during device operation.

In this study nickel ohmic and Schottky contacts were resistively fabricated on *n*-type 4*H*-SiC with a net doping density of 4×10^{14} cm^{-3}. Current-Voltage (*I-V*), Capacitance-Voltage (*C-V*), Deep Level Transient Spectroscopy (DLTS) and Laplace-DLTS measurement techniques were used to electrically characterize the fabricated Schottky diodes. The diodes were then irradiated with low energy electrons, alpha particles and protons. The characterization measurements were repeated after irradiation to evaluate the effect of irradiation on the electrical properties of SiC.

It was observed from *I-V* measurements that electron, alpha particle and proton irradiations do not significantly affect the rectification of Ni/SiC Schottky contacts. *C-V* measurements indicated that the free carrier removal rate is higher for alpha particle irradiation as compared to electron irradiation. The irradiated diodes were annealed in argon ambient and significant recovery in the free carrier concentration was observed below 600 °C. The free carrier concentration of proton irradiated Schottky contacts, which was decreased to below detection levels was also partly recovered after heat treatment of up to 400 °C.

DLTS and Laplace-DLTS measurements revealed the presence of four defect levels in as-grown 4*H*-SiC. These defects have been labelled $E_{0.10}$, $E_{0.12}$, $E_{0.17}$ and $E_{0.69}$ where the subscripts indicate the activation energies of the respective defects. Electron, alpha particle and proton irradiations were observed to induce three more defect levels with activation energies of 0.42 eV, 0.62 eV and 0.76 eV. Additionally, these irradiations were also observed to enhance the concentration of level $E_{0.69}$. All the radiation induced defects were annealed out at temperatures below 600 °C. In proton irradiated diodes, another defect with activation energy of 0.31 eV was observed after annealing the irradiated diodes at 625 °C.

Acknowledgements

For the success of this study, I cannot fully thank the people who made it possible

- My supervisor Professor F. D Auret and Co-Supervisor Dr M. M Diale for support, guidance and discussions throughout my MSc study.
- My mentor Mr M. Legodi for guidance and discussions during the course of this work.
- Dr W. Mtangi for the helpful discussions during the writing of this dissertation.
- Johan Janse Van Rensburg for helping with the proton irradiation experiments and DLTS troubleshooting.
- I would also like to extend many thanks the following members of the Electronic material and Thin Films Group whose contribution is appreciated; Prof W. Meyer, S. Coelho, Dr M. Schmidt, Louwrens van Schalkwyk, Dr C. Zander, P. Ngoepe, H. Danga, E. Omotoso, Hannes de Meyer, A. Mayimele and Kian.
- I want to thank the Head of the Physics Department, Prof Chris Theron, his predecessor Prof Malherbe, for affording me an opportunity to do part time work in the department.
- I would like to thank my Mr and Mrs Musara for their encouragement, love and financial support.
- Lastly, I want to thank my family for their love, support and always believing in me.

Above everything else, I thank the Lord; God in heaven whom I believe makes all things possible.

Declaration

I **Alexander Tapera Paradzah** declare that this thesis, which I hereby submit for the degree of Magister Scientiae in Physics at the University of Pretoria, is my own work and has not previously been submitted by me for a degree at this or any other institution.

SIGNATURE ……..

DATE ……..

Contents

CHAPTER 1

Introduction

Silicon carbide (SiC) is a wide bandgap compound semiconductor with excellent physical and opto-electronic properties. Among the physical properties of SiC is its high radiation hardness, a property which makes it a candidate for fabrication of radiation detector devices. Despite the semiconductor having excellent opto-electronic and physical properties, the growth of high quality crystals is very important for successful use in device fabrication.

SiC was initially grown by E. Acheson in 1892 using the process that is now known as the Acheson process [1]. The crystals produced by this process are of low quality and used mainly for abrasives and cutting purposes. Other growth techniques have been applied to SiC growth and have led to better quality crystals. These include Physical Vapour Transport, Lely Growth, Chemical Vapour Deposition, etc.

One problem that has however not been eliminated is the presence of defects in grown semiconductors. Defects common in as-grown semiconductors are micropipes, dislocations, impurities and intrinsic point defects. Intrinsic point defects can be in form of silicon or carbon vacancies, interstitials, antisites and complexes thereof. In addition to as grown defects, defects are also introduced in semiconductors during device fabrication and during operation of the devices. For successful fabrication of devices, it is important to have a better understanding of the introduction and effects of defects in semiconductors.

Several studies have been done on SiC to determine the material response to irradiation by different particles. This study aims to make a contribution to the knowledge of the response of *n*-type 4*H*-SiC to electron, alpha particle and proton irradiation. While particle irradiation studies on SiC have been done before, low doped SiC will be used in this study. Additionally, electron and alpha particle irradiations will be done with small and increasing fluences for a closer monitoring of the radiation induced changes.

The change in diode characteristics of the irradiated nickel Schottky diodes was monitored by current-voltage (*I*-*V*) and capacitance-voltage (*C*-*V*) measurements. *I*-*V* measurements show the effect of irradiation on the rectification properties of Ni/SiC. *C*-*V* measurements were

used to assess the effect of irradiation on free carrier concentration and consequently the calculation of the free carrier removal rate. Particle irradiation induces defects in semiconductors. Deep Level Transient Spectroscopy (DLTS) and Laplace-DLTS were used in the identification of the irradiation induced as well as grown defects.

Annealing of the irradiated diodes will be carried out in the temperature range from 100 °C to 700 °C in argon ambient. *I-V*, *C-V*, DLTS and Laplace-DLTS measurements will be repeated after each annealing step to monitor closely the recovery of diode rectification, free carrier concentration and the annealing out of, and / or appearance of new defects as a result of annealing irradiated diodes.

A more detailed discussion of the physical and electronic properties of SiC is given in Chapter 2. A metal-semiconductor junction is a very important part of this work as all measurements are done on such a junction. The physics of metal-semiconductor junctions is given in Chapter 3 while Chapter 4 gives a discussion on ion implantation. Ion implantation mainly deals with the interaction of ions with matter. The discussion on the theoretical background of this work is concluded in Chapter 5 where an extensive discussion of defects is given together with some theoretical aspects of DLTS. The experimental techniques used during the course of this work are explained in Chapter 6 and Chapter 7 gives the Results obtained. A summary of the obtained results is given in Chapter 8 together with aspects of future work that arises from the conducted study.

References

[1] K. Byrappa, T. Ohachi, Crystal Growth Technology, Springer, 2003.

CHAPTER 2

Introduction to silicon carbide

2.1 Introduction

This chapter presents the basic properties that make silicon carbide the competitive semiconductor that it is. First the bonding is discussed and the physical and electronic properties are presented in comparison to those of other commonly used semiconductors. A brief summary of the different growth techniques is then given, from the Acheson process to the chemical vapour deposition technique together with the doping processes needed to achieve either *p*–type or *n*–type SiC.

2.2 Bonding

Silicon carbide is a semiconductor crystal composed of polar layers of silicon and carbon which are nearly covalently bonded, with 12% ionic bonding, in which silicon is the positive ion and carbon is the negative ion. Each Si atom in SiC bonds with four C atoms forming a tetrahedron. Similarly, each C atom is also bonded to four Si atoms. Silicon and carbon therefore have a 1:1 stoichiometric relationship in SiC. Carbon and silicon atoms are separated by 1.89 Å whereas silicon atoms are separated by 3.08 Å [1]. A schematic of a SiC tetrahedron is shown in Figure 2.1.

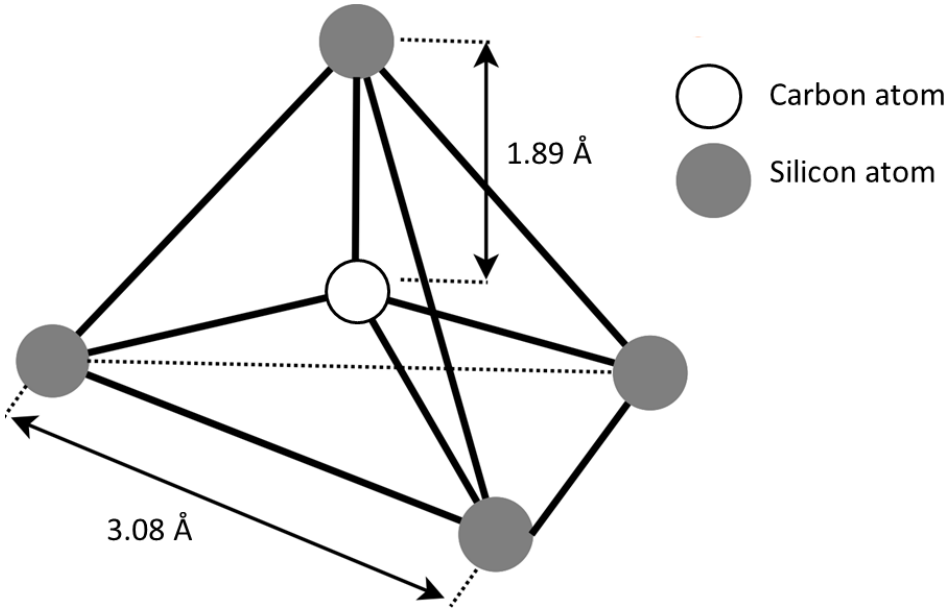

Figure 2.1 A silicon carbide tetrahedron redrawn from *ref*. [2]

The angle between two adjacent carbon atoms in a tetrahedron is 120°. SiC appears in different crystalline structures called polytypes. These are cubic, hexagonal or rhombohedral polytypes. 4*H*-SiC is a hexagonal polytype of SiC.

2.3 SiC and polytypism

One property that make SiC a unique and interesting semiconductor is its ability to form in dozens of different crystallographic configurations called polytypes where the stacking sequence of the SiC double layers along the c-axis differs from one polytype to the other. Over 200 different types of polytypes of SiC are known. The polytypes can be broadly grouped into three: cubic (C), hexagonal (H) and rhombohedral (R) following the cubic, hexagonal and rhombohedral crystalline structures in which the respective polytypes crystallizes. The Ramsdell notation: ‹ number ›‹ letter ›, is commonly used to name the different polytypes [3] where the number represents the number of layers before the sequence repeats and the letter signifies the crystal structure. For enlightenment, the 4*H*-SiC means there are four different layers that are repeated throughout the material and the structure is hexagonal. SiC is a polar semiconductor in that one side normal to the c-axis is silicon terminated and is referred to as the “silicon face” while the opposite side is carbon terminated and is known as the “carbon face” [4].

Only 3*C*-SiC, also known as β-SiC, exists in cubic form with a zinc-blend structure. If the layers are to be represented by letters A B C, then the 3C-SiC polytypes has the sequence A B C …. Among the hexagonal polytypes, 2*H*-, 4*H*-, and 6*H*-SiC are the most common types while the 15*R*-SiC is the most common rhombohedral polytype. The hexagonal polytypes are commonly referred to as α-SiC. 4*H*-SiC has the sequence A B A C …, 2*H*-SiC has the sequence A B ..., and 6H-SiC has sequence A B C A C B …. It is important to note that only 2*H*-SiC is purely hexagonal, 4*H*- and 6*H*- polytypes are 50 % and 33% hexagonal respectively with local cubic characteristics [3]. β-SiC is 100% cubic. Figure 2.2 shows the schematic representations of the 2*H*-, 3*C*-, 4*H*-, and 6*H*-SiC polytypes.

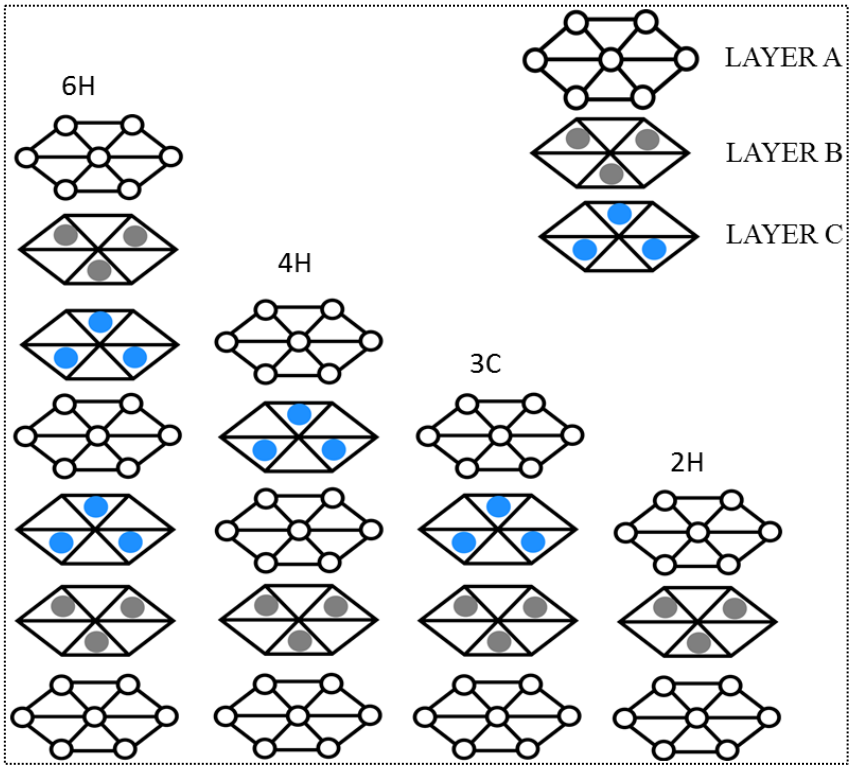

Figure 2.2 Schematic representation of the 6*H*-, 4*H*-, 3C-, and 2*H*-SiC polytypes redrawn from *ref.* [5].

Different polytypes have different physical, electronic, and optical properties. It is for this reason that some polytypes are preferred ahead of others. To date the 4*H*- and 6*H*- polytypes have been most widely studied and the former is being more widely used in the electronics industry.

2.4 Physical and electrical properties of SiC

Different polytypes of SiC have different physical, chemical and opto-electronic properties.

Table 2.1 gives a comparison of the electrical properties of common SiC polytypes; 6*H*-, 4*H*- and 3*C*-, and other wide band gap semiconductors; gallium arsenide (GaAs) and gallium nitride (GaN). Since silicon is currently the most widely used semiconductor in the devices industry, its properties are also included in Table 2.1.

Table 2.1 Comparisons of some important electrical properties of common SiC polytypes, Silicon (Si), gallium arsenide (GaAs) gallium nitrite (GaN) at 300K. The table has been compiled from *refs*. [6-8]

	4*H*-SiC	6*H*-SiC	3*C*-SiC	Si	GaAs	GaN
Bandgap (eV)	3.26	3.02	2.36	1.12	1.42	3.4
Relative dielectric constant	9.7	9.7	9.3	11.9	13.1	9.5
Breakdown field ($MVcm^{-1}$)	//c-axis 3.0 ⊥c-axis 2.5	//c-axis 3.2 ⊥c-axis >1	>1.5	0.6	0.6	2-3
Thermal conductivity (W/cm-K)	3-5	3-5	3-5	1.5	0.5	1.3
Electron mobility ($cm^2 V^{-1}s^{-1}$)	//c-axis 800 ⊥c-axis 800	//c-axis 800 ⊥c-axis 60	750	1200	6500	900
Saturation electron velocity ($10^7 cms^{-1}$)	2.0	2.0	2.5	1.0	1.2	2.5
Intrinsic carrier concentration (cm^{-3})	$\sim 10^{-7}$	$\sim 10^{-5}$	~ 10	10^{10}	2×10^{6}	10^{-10}

2.4.1 Bandgap and intrinsic carrier concentration

SiC is a wide bandgap semiconductor with the bandgap energy varying from 3.26 eV for 3*C*-SiC to 3.33 eV for 2*C*-SiC [8]. The wide bandgap energy of SiC makes it suitable for high temperature device operation due to a restriction on leakage currents that would arise from thermal ionisation of electrons from the valence band. The low intrinsic carrier concentration of SiC also helps in ensuring that conduction is controlled by dopant impurities even at relatively higher temperatures as the intrinsic carrier concentration remains negligible. SiC has a distinct advantage especially ahead of silicon as it has a larger bandgap and lower intrinsic carrier concentration. SiC can therefore operate at temperatures as high as 800 °C whereas Si can only efficiently operate at temperatures of up to 300 °C.

2.4.2 Breakdown electric field

The applied voltage on devices creates an electric field across the depletion region. This field sweeps out any carriers in the depletion region that may have been created by generation-recombination or might have diffused from adjacent quasi-neutral regions [9]. As the voltage increases, the electric field also increases accelerating the charge carriers to greater velocity and consequently increasing their kinetic energy. The carriers may gain sufficient energy such that their interaction with lattice atoms produces electron excitation from the valence band, a phenomenon known as impact ionisation. Impact ionisation is a multiplicative phenomenon in that the produced electrons may also participate in the ionisation of more atoms and eventually the current flow increases significantly. When a device fails to operate due to such increases in current flow, it is said to have undergone avalanche breakdown [10]. SiC has a high breakdown voltage which is five times that of silicon, hence it can be used more conveniently in the fabrication of devices for high voltage operation.

2.4.3 Thermal conductivity and carrier mobility

Thermal conduction through conduction electrons and phonons is a dominant heat flow process in solids compared to radiation and convection [11]. An increase in temperature during device operation usually leads to undesirable changes in device properties such as reduced carrier mobility. It is therefore important that heat produced be conducted away hence semiconductor materials for device fabrication should preferably have a high thermal conductivity to carry away the heat. With a high thermal conductivity which is said to be higher than for metals at room temperature [12], SiC is most suitable for devices where various resistive processes may lead to the generation of heat within the device. High temperature capability is also advantageous in elimination of cooling processes such as fans, long wire runs, liquid cooling and thermal shielding which is associated with the silicon semiconductor technology [4]. Silicon has however a higher electron mobility than SiC but as the temperature starts to increase, the situation becomes inverted and hence SiC still gets preference.

2.4.4 Saturation drift velocity

Saturation drift velocity is a very important parameter when high frequency devices are considered [13]. Semiconductors with a high drift velocity have a high frequency operation limit. SiC has a high saturation velocity and can thus be used more effectively for such devices compared to most other devices as shown in Table 2.1.

2.5 Synthesis of SiC

Successful growth of a semiconductor is very important for the development of a material for use in the semiconducting industry in light of many high quality semiconductors available with competing physical, electronic and chemical properties. A material should be grown and be of very high quality, that is, high purity and a low micropipe density to achieve, for instance, semi insulating (SI) semiconductors. The absence of impurities is also important as this would enable conduction to be properly controlled through doping.

SiC is grown both epitaxially and in bulk [3]. The Physical Vapour Transport (PVT) process also known as the "modified Lely" and the High Temperature Chemical Vapour Deposition (HTCVD) are the bulk growth techniques while epitaxial growth is done using the Chemical Vapour Deposition (CVD) process. Epitaxial growth of SiC can also be achieved through Sublimation Epitaxy and the Liquid Phase Epitaxy (LPE) processes [14].

2.5.1 Acheson process

This section was developed following Byrappa *et al.*[14] unless cited otherwise. The Acheson process was first used in 1892 to produce the first SiC semiconductor [4]. In the Acheson process, a mixture of 50% silica, 40% carbon, 3% salt and 7% saw dust is heated in an electrical furnace. Heating is done by resistive heating of the core of graphite and coke placed at the centre of the furnace up to 2700°C and maintained there for some time before the temperature is gradually reduced. When the temperature reaches 1800°C, amorphous SiC forms but as the temperatures increases it decomposes into graphite and silicon. Graphite remains at the core but silicon evaporates and reacts with carbon at the adjacent cooler surfaces to give SiC. Meanwhile, the sawdust maintains porosity of the mixture for carbon monoxide and other gaseous wastes to escape easily while salt improves the purity of the SiC by reacting with metallic impurities to form metal chlorides.

Although the first LED was produced using Acheson SiC, the semiconductor produced through the process is of low quality and is used mainly for cutting and grinding purposes rather than device fabrication [15].

2.5.2 Lely growth method

Due to the low quality of crystals obtained from the Acheson process, there was need for better growth techniques and in 1955, Lely developed what become to be known as the Lely process [16]. In the Lely method, SiC lumps are filled between two concentric graphite tubes.

The inner tube is withdrawn after complete packing of the lumps leaving a porous SiC wall inside the outer tube (crucible). The crucible is then closed with SiC or graphite and vertically placed in a furnace which is heat up to 2500 °C in Argon at atmospheric pressure [16]. At these temperatures, SiC lumps decompose and sublime from the crucible nucleating at the cooler surface of the porous SiC cylinder in the middle of the furnace. With prolonged heating, SiC platelets grow. It is however difficult to impose supersaturation making it impossible to control the nucleation hence platelets of incomplete hexagonal habit results [14]. The platelets are of high quality, and in some cases can be dislocation free over a few square millimetres. However, because of the shape irregularities, crystals grown from this process are not commercially viable for large scale manufacture [14, 17].

2.5.3 Physical vapour transport

The Physical Vapour Transport growth method is a modification of the Lely method by Tairov and Tsvetkov in the late 1970's and has been widely used for bulk SiC growth since then [18]. It is for that reason also known as the Modified Lely Process or the Seeded Sublimation method. This process was supposed to address the issues of nucleation controllability which were incontrollable in the Lely method. In the PVT method, a seed is kept at a low temperature compared to the crucible with a thermal gradient of about $20 - 40\ ^{\circ}C$ being maintained. Pressure is kept below atmospheric and argon ambient of very high purity is used. This method initially produced ingots of 8 mm in both diameter and length though larger dimension ingots were later realised [19, 20].

2.5.4 High temperature chemical vapour deposition (HTCVD)

Introduced in 1995, the HTCVD method uses gases instead of a powder as a source material for boule growth. Three gases; silane, ethylene and a helium carrier are used and slowly introduced into a three stage reactor [21].

At high temperatures, silane decomposes into silicon liquid droplets and reacts with ethylene to form microparticles of Si_xC_y. Hydrocarbons may be added to form stable Si_xC_y, the stability being achieved because of the non-solubility of carbon in silicon hence when carbon is added to liquid silicon, the phase will be solid rather than liquid. In the sublimation zone, the Si_xC_y decompose into Si, Si_2C and SiC_2, and these sublimed species later condense on the seed due to a thermal gradient. A growth rate of 1 µm/h can be reached with this technique with proper optimization of growth conditions [22].

2.5.5 Chemical vapour deposition (CVD)

CVD of SiC normally uses hydrogen as the carrier gas with silane and a hydrocarbon as the precursor gases and the flow is laminar. As the gases reach the susceptor, the velocity of flow is reduced to zero and the precursor gases are heated and decompose. The resulting species diffuse through a boundary layer and grow on the reactor wall and on the substrate. Due to the consumption of species, concentration of precursor gases falls in the direction of flow resulting in a tapered layer thickness-depletion. It is usual to taper the susceptor resulting in a decreased diffusion of active species thus compensating for depletion [23].

2.6 Doping of SiC

Doping of any semiconductor is very crucial in the semiconductor industry as it controls the electrical characteristics of the material. An intrinsic semiconductor is made *n*-type or *p*-type through doping so it can be used for current conduction. Nitrogen and aluminium are the common dopants of SiC used to achieve *n*-type or *p*-type SiC, respectively. SiC is doped through epitaxially controlled doping and hot implantation [24]. Ion implantation followed by annealing is mostly, but not limited to cases where a pattern may be required and only parts of the semiconductor are to be doped. Epitaxial doping for both aluminium and nitrogen in SiC is affected by temperature, pressure, growth rate and C/Si ratio [25-28].

Nitrogen replaces carbon in the C–Si bond to achieve *n*–type doping since nitrogen has one more valence electrons compared to carbon. A lower C/Si ratio would encourage more site competition between nitrogen and carbon atoms for the carbon site thereby enhancing nitrogen doping. Nitrogen doping is suppressed by increasing the C/Si ratio since the site competition would be reduced. The same logic of C/Si ratio holds for aluminium doping where aluminium atoms replace Si to achieve *p*–type doping.

Forsberg et al [25, 26] discusses the effects of the other doping controlling factors. These may however differ with different growing techniques in the case of epitaxial doping.

References

[1] S.H. Ryu, A.K. Agarwal, R. Singh, J.W. Palmour, 1800 V NPN Bipolar Junction Transistors in 4H–SiC, IEEE Electron Device Letters, **22** (2001) 124.

[2] D. Perrone, 'Process and Characterisation Techniques on 4H-Silicon Carbide', Ph.D. Thesis, Politecnico di Torino, Torino, 2007.

[3] M.J. Marinella, *Silicon Carbide (SiC) An Overview*, Arizona State University.

[4] P.G. Neudeck, *Silicon Carbide Technology*, CRC Press LLC, 2006.

[5] M. Florian, L.E. Carvalho, C.A.A. Cairo, SiC_f/SiC Composite: Attainment Methods, Properties and Characterization, Advances in Ceramics - Synthesis and Characterization, Processing and Specific Applications, 2011.

[6] P.G. Neudeck, Progress in Silicon Carbide Semiconductor Electronics Technology, Journal of Electronic Materials, **24** (1995) 283.

[7] J.B. Casady, R.W. Johnson, Status of Silicon Carbide (SIC) as a widebandgap semiconductor for high temperature applications: A Review. Solid-State Electronics, **39** (1996) 1409.

[8] G.L. Harris, *Properties of Silicon Carbide*, IET, 1995.

[9] B.J. Baliga, *Fundamentals of Power Semiconductor Devices*, Springer Science & Business Media, USA, 2008.

[10] B. Kumar, S.B. Jain, *Electronic Devices and Circuits*, PHI Learning Pvt. Ltd, 2007.

[11] P. Bhattacharya, S. Mahajan, H. Kamimura, *Comprehensive Semiconductor Science and Technology*, Elsevier Science, Newnes, 2011.

[12] S.E. Saddow, A.K. Agarwa, *Advances in Silicon Carbide Processing and Applications*, Artech House, 2004.

[13] V.I. Sankin, A.A. Lepneva, Saturated vertical drift velocity of electrons in silicon carbide polytypes, Semiconductors, **33** (1999) 547.

[14] K. Byrappa, T. Ohachi, *Crystal Growth Technology*, First ed., William Andrew Inc, New York, 2003.

[15] A.W. Weimer, Carbide, *Nitride and Boride Materials Synthesis and Processing*, First ed., Chapman & Hall, 1997.

[16] R.K. Willardson, E.R. Weber, *SiC Materials and Devices*, Vol. 52., Academic Press, 1998.

[17] J. Takashi, N. Ohtani, Modified-Lely SiC Crystals Grown in [11-00] and [112-0] Directions, Physica Status Solidi (b) **202** (1997) 163.

[18] Q.S. Chen, J. Lu, Z.B. Zhang, G.D. Wei, V. Prasad, Growth of silicon carbide bulk crystals by physical vapor transport method and modeling efforts in the process optimization, Journal of Crystal Growth, **292** (2006) 197.

[19] Y.M. Tairov, V.F. Tsvetkov, Investigation of growth processes of ingots of silicon carbide single crystals, Journal of Crystal Growth, **43** (1978) 209.

[20] V.D. Heydemann, N. Schulze, D.L. Barrett, G. Pensl, Growth of 6H and 4H silicon carbide single crystals by the modified Lely process utilizing a dual-seed crystal method, Applied Physics Letters, **69** (1996) 3728.

[21] G. Dhanaraj, P.K. Byrappa, V. Prasad, P.M. Dudley, *Springer Handbook of Crystal Growth*, First ed., Springer, Berlin, 2010.

[22] C.M. Zetterling, *Process Technology for Silicon Carbide Devices*, Second ed., IET, United Kingdom, 2002.

[23] B. Choi, D. Kim, Growth of silicon carbide by chemical vapour deposition, Journal of Materials Science Letters, **10** (1991) 860.

[24] J.B. Casady, R.W. Johnson, Status of Silicon Carbide (SIC) as a widebandgap semiconductor for high temperature applications: A Review, Solid-State Electronics **39** (1996) 1409.

[25] U. Forsberg, A. Danielsson, A. Henry, M.K. Linnarsson, E. Janzen, Nitrogen doping of epitaxial silicon carbide, Journal of Crystal Growth, **236** (2002) 101.

[26] U. Forsberg, O. Danielsson, A. Henry, M.K. Linnarsson, E. Janzen, Aluminum doping of epitaxial silicon carbide, Journal of Crystal Growth, **253** (2003) 340.

[27] D J Larkin, P G Neudeck, J A Powell, L.G. Matus, *Site-Competition Epitaxy for Controlled Doping of CVD Silicon Carbide*, SiC and Related Materials Conference, Washington, DC, 1993.

[28] D.J. Larkin, P.G. Neudeck, J.A. Powell, L.G. Matus, Site-competition epitaxy for superior silicon carbide electronics, Applied Physics Letters, **65** (1994) 1659.

CHAPTER 3

Metal-Semiconductor Junctions

3.1 Introduction

Metal-semiconductor junctions are very important for the semiconductor device industry as they allow for the determination of most electronic semiconductor properties. In this work, metal-semiconductor junctions are used mainly for defect characterization through probing of a depletion layer which is synonymous with these junctions. This chapter explains the formation of Schottky diodes under both ideal and non-ideal conditions in the first sections of the chapter. The depletion layer, also commonly known as the space charge region, is then discussed. Properties of this region such as capacitance and depletion width under different biasing conditions are given in sections 3.3.1 and 3.3.2. Apart from Schottky diodes, metal-semiconductor contacts can be ohmic contacts depending on a number of factors but mostly the doping density of the semiconductor. Ohmic contacts are discussed in section 3.4. Different processes are responsible for the transport of charge carriers across the Schottky barrier. The thermionic emission theory and the tunnelling current mechanisms are discussed in sections 3.5.1 and 3.5.2. Thermionic emission is responsible for current transport across the barrier at higher temperatures while tunnelling current is important for ohmic contacts where the barrier is sufficiently thin.

3.2 Schottky barrier diodes

Evaporation of a metal onto a semiconductor produces either an ohmic contact (contact of low contact resistance) or a rectifying contact (Schottky diode). The formation of a Schottky diode will in this thesis be explained by considering two cases: (1) the ideal metal-semiconductor contact without any surface states (Schottky–Mott theory) and (2) the *MS* contact where the density of surface interface states is high (Bardeen theory) [1].

3.2.1 Ideal Schottky barrier

When isolated from each other, the metal and the semiconductor generally have different work functions (energy difference between the Fermi level, E_F and the vacuum level, E_{vac}) [2] as shown in Figure 3.1 (a). The vacuum level is used to define an infinite distance from a

solid where an electron has zero kinetic energy [2]. The metal work function ($e\Phi_m$) is the energy difference between the Fermi level and the vacuum level, e is the electronic charge. In a semiconductor, the equivalent of a metal work function is given by ($e\Phi_n + e\chi_{sc}$) where $e\Phi_n$ is the energy difference between the Fermi level and the bottom of the conduction band, i.e. $e\Phi_n = E_C - E_F$. $e\chi_{sc}$ is the electron affinity, which is defined as the energy difference between the bottom of the conduction band, E_C and the vacuum level, E_V [3].

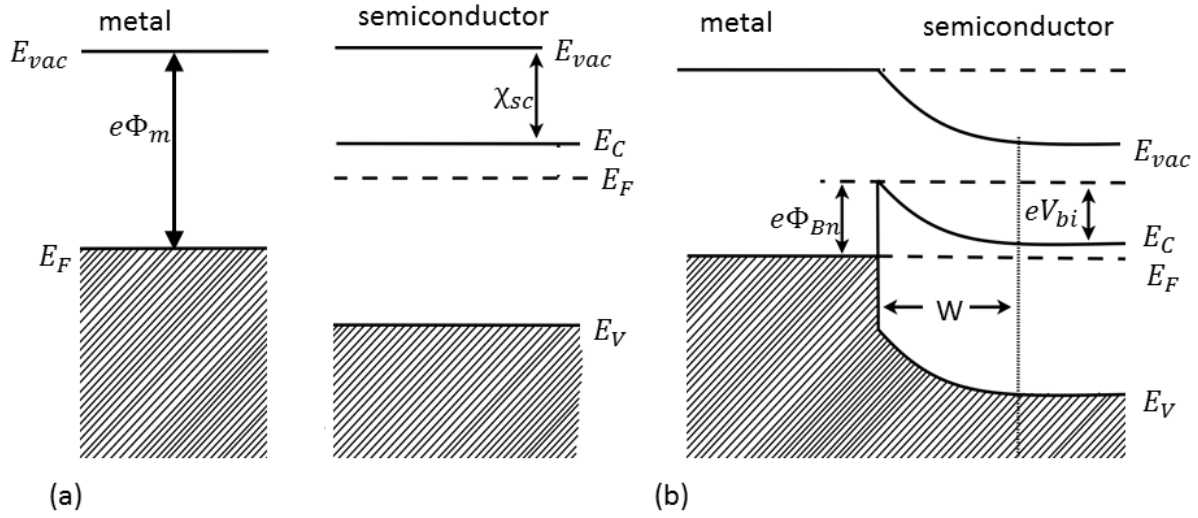

Figure 3.1 Schematic representation of a Schottky diode formation. (a) No contact yet between metal and semiconductor, (b) after contact and Schottky barrier formation. Diagram redrawn from *ref*. [2]

Consider now a case where the metal and the semiconductor are brought into thermodynamic contact, Figure 3.1(b). Since the semiconductor Fermi level, $E_{F,S}$ is greater than the metal Fermi level, $E_{F,m}$ electrons will flow from the semiconductor to the metal until the Fermi levels equilibrate [2, 3]. The equilibration of the Fermi levels causes the formation of a potential barrier (Schottky barrier, $e\Phi_{Bn}$) which the electrons flowing from the metal to the semiconductor would have to surmount with a limiting value of the barrier being [3-7]

$$e\Phi_{Bn} = e(\Phi_m - \chi_{sc}) \qquad 3.1$$

From Equation 3.1, an ideal Schottky barrier height is defined as the difference between the metal work function and the semiconductor electron affinity. The subscript *n* is used to denote an *n*-type semiconductor. Likewise a *p*-type semiconductor Schottky barrier height is denoted by a subscript *p* and its Schottky barrier height has the form [3]

$$e\Phi_{Bp} = E_g - e(\Phi_m - \chi_{sc}) \qquad 3.2$$

where E_g is the semiconductor bandgap. It should be noted that as the metal and the semiconductor are brought into contact, there is an accumulation of negative charges that takes place at the metal side in the vicinity of the interface. This negative charge is compensated by a positive charge in the semiconductor side that results from the flow of electrons into the metal. It therefore follows from this that a potential drop (V_{bi}), termed the built in potential, will be established at the *M-S* junction and this has the form [2]

$$V_{bi} = \frac{\Phi_{Bn}}{e} + \Phi_n = \frac{\Phi_m - \chi_{SC}}{e} + \Phi_n \qquad 3.3$$

A region in the semiconductor close to the interface is left depleted of charge carries and is known as the depletion region (width w) which will be discussed in section 3.3.

Equations 3.1 and 3.2 give a picture that the Schottky barrier height only depends on the values of the electron affinity and the metal work function. This is however only ideal and does not hold for practical diodes [8]. Some of the reasons why the Schottky barrier height does not only depend on the metal work function and the semiconductor electron affinity are the existence of surface states/interface states on the semiconductor surface and also the presence of a small distance (δ) between the metal and the semiconductor even after the contact is established [9].

3.2.2 Interface states

The barrier height was experimentally found not to vary with metal type [1, 10], meaning that the Fermi level is pinned at a certain position in the energy gap. Bardeen [11] proposed that surface states of the semiconductor are responsible for pinning the Fermi level and thus the barrier height is a function of these surface states, not the metal type. The calculation of the barrier height considering interface states (and the metal work function as this is not completely disregarded) as presented in this dissertation will be developed following Sze [3] unless cited otherwise. Assumptions are made in this development that, (1) the interface layer is of atomic dimension and is therefore transparent to electrons but can withstand the potential across it and (2) interface states are a property of the semiconductor only and are independent of the metal type.

Figure 3.2 shows a simplified diagram for the barrier height formation in the presence of interface states. A more elaborate diagram for the formulation of the Schottky barrier diode in the presence of surface states is given by Figure 3.3. A neutral energy level ($e\Phi_0$ above

E_V) exists on the semiconductor surface above which states are of acceptor type and below are donor type. Acceptor states are neutral when empty and negatively charged when filled while donor states are neutral when filled and positively charged when empty. When the neutral level coincides with the Fermi level at the surface, the net interface trap charge is zero. This is the energy level that pins the Fermi level before contact with the metal is established.

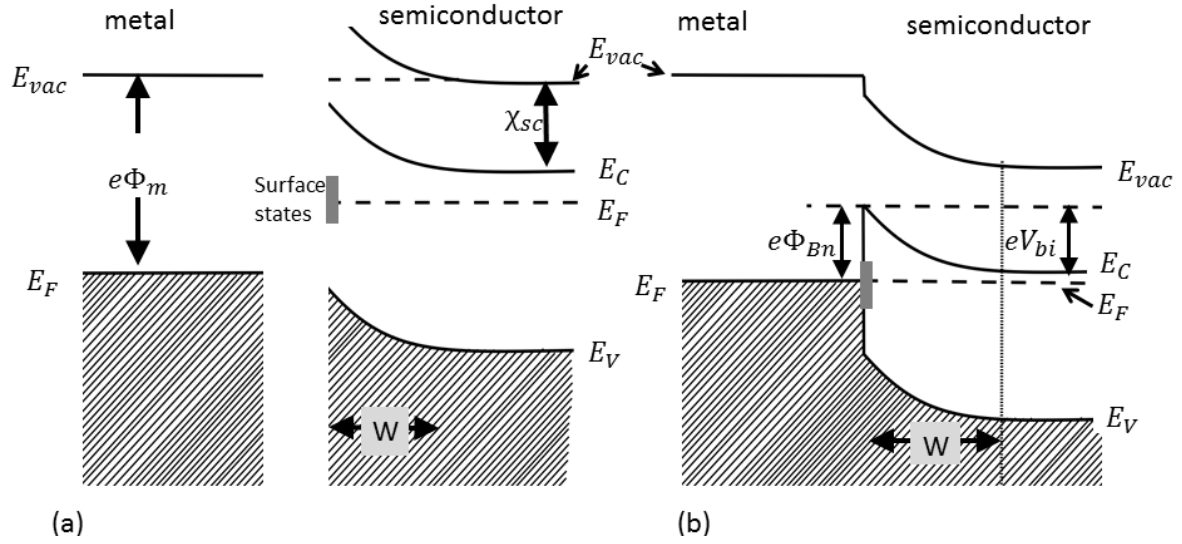

Figure 3.2 Formation of a Schottky diode in the presence of surface states. (a) a depletion width already exist before contact due to Fermi level pinning, and (b) Schottky barrier formed. Diagram redrawn from *ref*. [2]

Taking a semiconductor with an acceptor interface trap density (D_{it} states/cm^{-2}eV) extending from $e\Phi_0 + E_V$ to E_F, the interface-trap charge density Q_{SS} on the semiconductor will be negative and is given by

$$Q_{SS} = -eD_{it}(E_g - e\Phi_0 - e\Phi_{Bn}) \quad {}^{C}/_{cm^2} \tag{3.4}$$

At thermal equilibrium, the space charge that forms in the semiconductor depletion layer is given by

$$Q_{SC} = eN_D w = \sqrt{2e\epsilon_S N_D \left(\Phi_{Bn} - \Phi_n - \frac{k_B T}{e}\right)} \tag{3.5}$$

The sum of Equations 3.4 and 3.5 gives the total equivalent charge density on the semiconductor surface. An equal and opposite charge Q_M ($C\ cm^{-2}$) develops on the metal surface if there are no space charge effects on the interfacial layer. Q_M is given by

$$Q_M = -(Q_{ss} + Q_{SC}) \tag{3.6}$$

To obtain the potential Δ across the interfacial layer, Gauss' law is applied to the surface charge on the metal and semiconductor surfaces, i.e.

$$\Delta = -\frac{\delta Q_M}{\epsilon_i} \tag{3.7}$$

It can also be seen from Figure 3.2 that

$$\Delta = \Phi_m - (\chi_{sc} + \Phi_{Bn}) \tag{3.8}$$

Combining Equations 3.7 to 3.8, the following result is obtained

$$\Phi_m - \chi_{sc} - \Phi_{Bn} = \sqrt{\frac{2e\epsilon_S N_D \delta^2}{\epsilon_i^2}\left(\Phi_{Bn} - \Phi_n - \frac{k_B T}{e}\right)} - \frac{eD_{it}\delta}{\epsilon_i}\left(E_g - e\Phi_0 - e\Phi_{Bn}\right) \tag{3.9}$$

Equation 3.9 can be solved by introducing constants c_1 and c_2 such that

$$c_1 \equiv \frac{2e\epsilon_S N_D \delta^2}{\epsilon_i^2} \tag{3.10}$$

and

$$c_2 \equiv \frac{\epsilon_i}{\epsilon_i + e^2 \delta D_{it}} \tag{3.11}$$

The result that is obtained is treated considering two limiting cases:

(1)$D_{it} \to \infty$, then $c_2 \to 0$, giving

$$e\Phi_{Bn} = E_g - e\Phi_0 \tag{3.12}$$

Equation 3.12 represents a case where the barrier height is independent of the metal work function. This is the case where the Fermi level is pinned and the barrier height is determined sufficiently from the properties of the semiconductor.

(2) $D_{it} \to 0$, then $c_2 \to 1$, giving

$$e\Phi_{Bn} = e(\Phi_m - \chi_{sc}) \tag{3.13}$$

This is a case where the surface states are negligible and Equation 3.1 is once again valid, i.e. the ideal Schottky barrier height can then be realised.

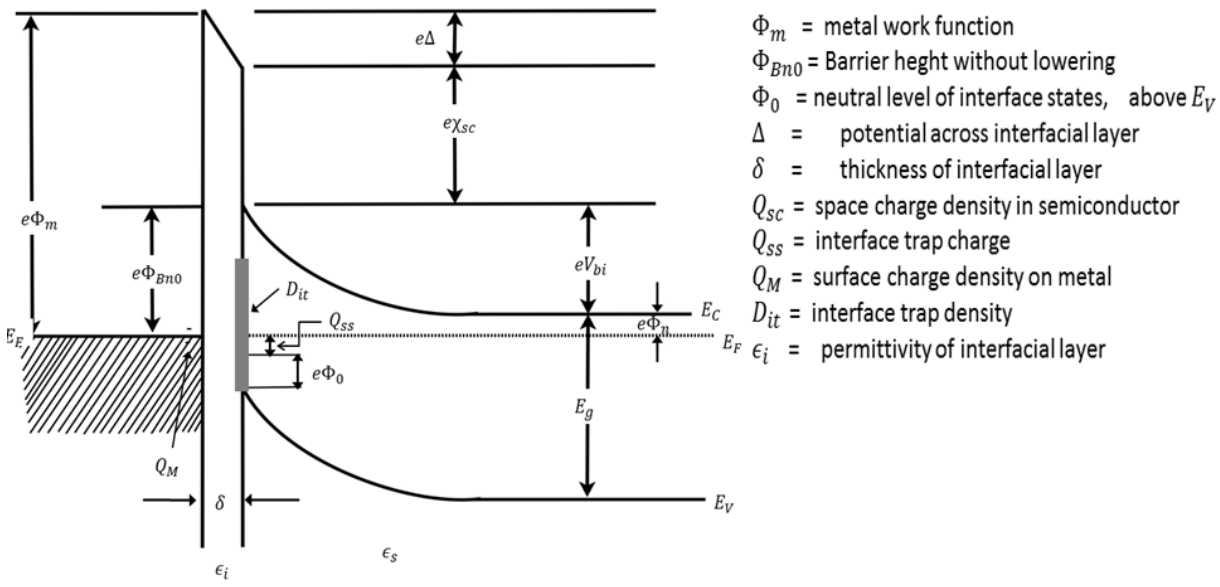

Figure 3.3 Schematic showing the formation of a Schottky barrier height in the presence of surface states and a distance δ between metal and semiconductor. Diagram redrawn from ref.[3]

3.2.3 Image force lowering

Other than the presence of interface states, the Schottky barrier height can also be modified by what is referred to as the image force. The image force has an effect of lowering the barrier height due to the presence of external electric fields.

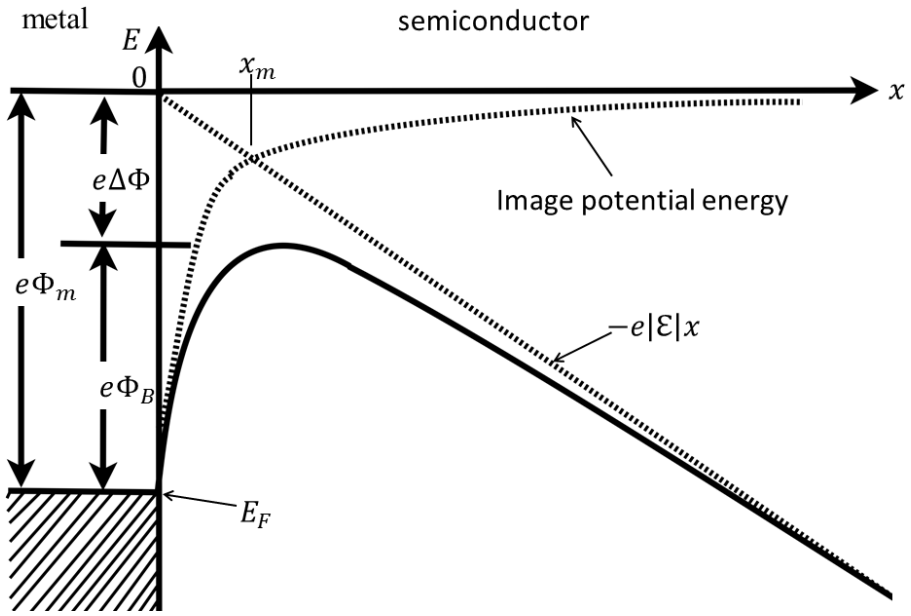

Figure 3.4 Energy band diagram showing the image force barrier lowering due to the presence of an electric field. Diagram has been drawing from ref. [3]

Consider an electron located in the semiconductor at a distance x from the metal. An induced positive charge exists on the metal surface due to the electron. The force of attraction that

exists between the electron and the induced positive charge is equal to the force that would exist as a result of an equal positive charge a distance $-x$ outside the metal [2, 3]. This image force, F_{if} is given by [2]

$$F_{if} = -\frac{e^2}{16\pi\epsilon_s x^2} \tag{3.14}$$

where ϵ_s is the dielectric constant of the semiconductor. The energy, E_{if} required to bring an electron from infinity to a distance x is obtained by integrating F_{if}, that is

$$E_{if} = \int_{\infty}^{x} F_{if}\,dx = -\frac{e^2}{16\pi\epsilon_s x} \tag{3.15}$$

In the presence of an external field $\mathcal{E}$, Equation 3.15 becomes [3]

$$E_{tot} = -e\mathcal{E}x - \frac{e^2}{16\pi\epsilon_s x} \tag{3.16}$$

The position, x_m of the image force lowering is obtained as the maximum of the function, from the condition $(dE_{tot}/dx) = 0$ occurring at [6]

$$x_m = \sqrt{\frac{e}{16\pi\epsilon_s \mathcal{E}}} \tag{3.17}$$

and the magnitude of the image force lowering ($\Delta\varphi$) is given by [12]

$$\Delta\varphi = \sqrt{\frac{e\mathcal{E}}{4\pi\epsilon_s}} = 2\mathcal{E}x_m \tag{3.18}$$

Equations 3.17 and 3.18 shows that the position of the lowering decreases as the electric field is increased while the image force lowering increases with increasing electric field. The magnitude of the barrier lowering is greater for higher electric fields.

3.3 Space charge region

As the metal and the semiconductor are brought into contact during Schottky diode formation, electrons accumulate in the metal leaving an accumulation of a positive charge in the semiconductor close to the interface. This induces an electric field pointing towards the

metal from the semiconductor. The region between these two "charged regions" is depleted of charge carriers and is known as the depletion region or space charge region [13].

3.3.1 Depletion width

This work assumes an *n*-type semiconductor as SiC used in this thesis is *n*-type. The charge density, $\rho(x)$ in the depletion region assuming the abrupt approximation (Schottky–Mott model) is given by [13]

$$\rho(x) = \begin{cases} e[\sum N_D^+(x) - \sum N_A^-(x)] & 0 < x < w_D \\ 0 & x > w_D \end{cases} \quad 3.19$$

$\sum N_D^+(x)$ and $\sum N_A^-(x)$ are the total ionised donor and acceptor concentration at a depth (x) from the interface respectively. The potential at the *MS* interface is considered to be $-\varphi_{bi} < 0$ as a further barrier condition. Poisson's one dimensional equation can be applied to find the potential drop in the space charge region [2]

$$\frac{d^2\varphi}{dx^2} = \frac{\rho(x)}{\epsilon_0\epsilon_r} \quad 3.20$$

where ϵ_r is the relative dielectric constant and ϵ_0 is the permittivity of vacuum. $\epsilon_0\epsilon_r = \epsilon_s$ is the dielectric constant of the semiconductor. Using knowledge of solving differential equations, Equation 3.20 is solved to give

$$\varphi(x) = -V_{bi} + \frac{eN_D}{\epsilon_s}\left(w_0 x - \frac{x^2}{2}\right) \quad 3.21$$

w_0 is the depletion width at zero bias. The electric field strength in the space charge region is given by [2]

$$\varepsilon(x) = -\frac{eN_D}{\epsilon_s}(w_0 - x) = \varepsilon_m + \frac{eN_D}{\epsilon_s}x \quad 3.22$$

where ε_m is the maximum electric field equal to $-eN_D w_0/\epsilon_s$ at $x = 0$. It follows from the boundary conditions $(d\varphi/dx = 0)$ that

$$w_0 = \sqrt{\frac{2\epsilon_s}{eN_D}V_{bi}} \quad 3.23$$

A more accurate determination of the depletion width is obtained by considering the majority carrier concentration in addition to the impurity concentration in the Poisson's equation [3]. Defining $\beta = e \,/\, k_B T$ as the dependence of the charge density on the potential, Equation 3.23 is corrected to

$$w_0 = \sqrt{\frac{2\epsilon_s}{eN_D}(V_{bi} - \beta^{-1})} \tag{3.24}$$

If an external voltage (V_{ext}) is applied to the diode, the interface boundary condition becomes $\varphi(0) = -V_{bi} + V_{ext}$. The depletion width as given by Equation 3.24 then becomes

$$w_0 = \sqrt{\frac{2\epsilon_s}{eN_D}(V_{bi} - V_{ext} - \beta^{-1})} \tag{3.25}$$

Figure 3.5 illustrate the change of the depletion width under different biasing conditions.

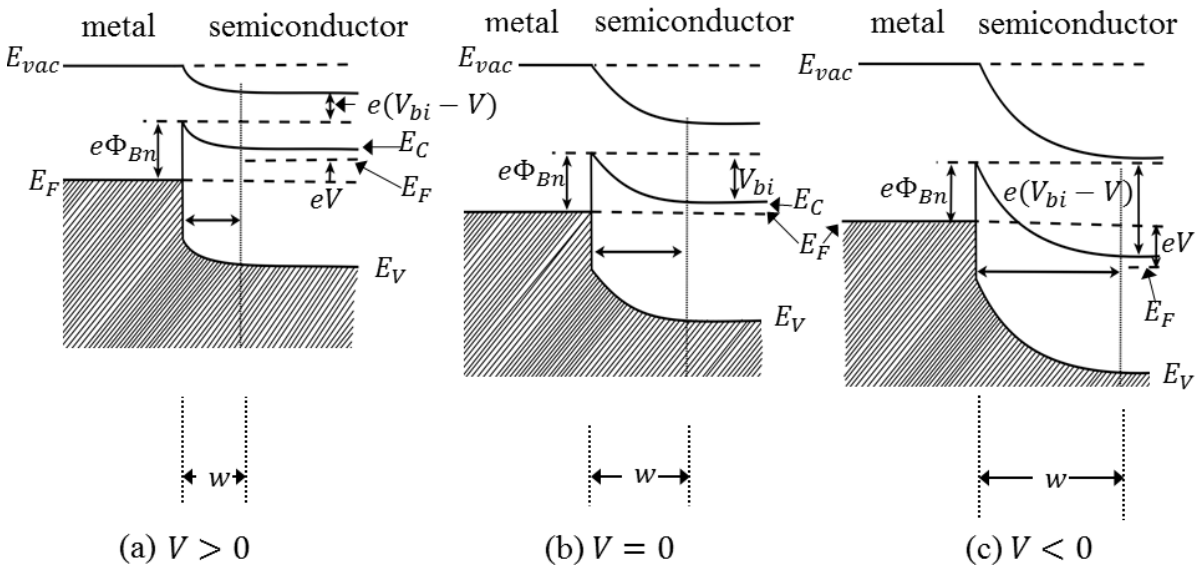

Figure 3.5 Band structures of metal-semiconductor junctions under (a) forward, (b) zero and (c) reverse biasing conditions as indicated. Diagram redrawn from *ref.* [2]

3.3.2 Space charge region capacitance

The total space charge per unit area, Q of the semiconductor is given by [2, 3]

$$Q = eN_D w_D = \sqrt{2\epsilon_s eN_D(V_{bi} - V_{ext} - \beta^{-1})} \tag{3.26}$$

In the determination of the space charge capacitance, the depletion region is kept at a reverse dc voltage which determines the depletion width. A periodical small ac voltage, δV is then superimposed onto the quiescent dc voltage to probe the capacitance.

The total depletion region capacitance, C per unit area is obtained from the relation $C = dQ/dV$. Thus when the Schottky diode is maintained at V_{ext}, then the depletion region capacitance is given, following Equation 3.26, by [10, 14]

$$C = \sqrt{\frac{eN_D\epsilon_s}{2(V_{bi} - V_{ext} - \beta^{-1})}} = \frac{\epsilon_s}{w} \qquad 3.27$$

Equation 3.27 can be simplified to

$$\frac{1}{C^2} = \frac{2(V_{bi} - V_{ext} - \beta^{-1})}{eN_D\epsilon_s} \qquad 3.28$$

If the diode capacitance is measured as a function of external voltage, a straight line graph of $1\ /\ C^2$ against V_{ext} should be obtained, Figure 3.6. Also shown on the Figure is the capacitance voltage plot.

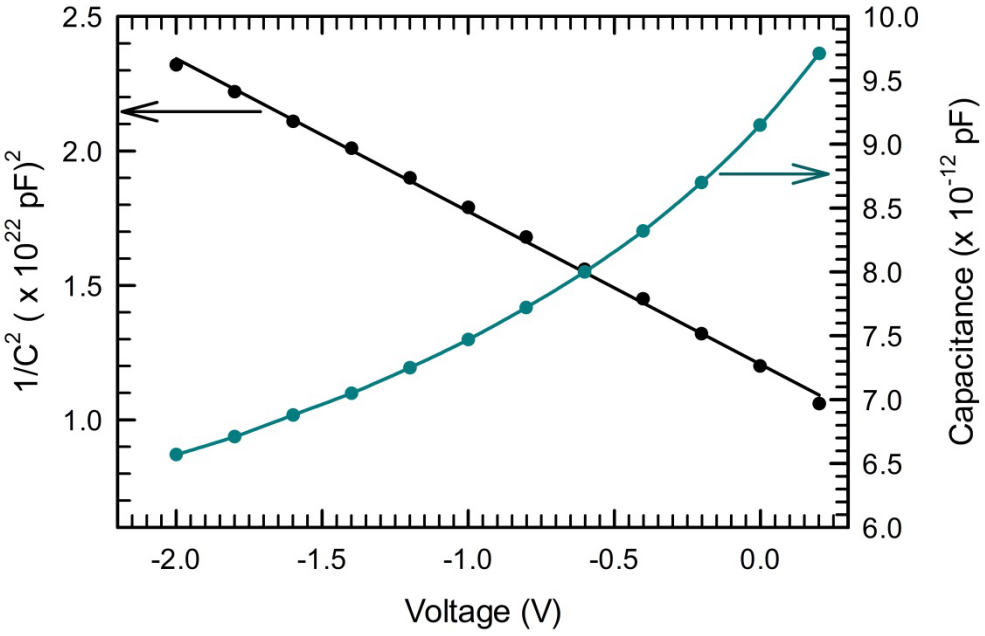

Figure 3.6 A graph of $1/C^2$ (pF^{-2}) and Capacitance (pF) versus Voltage (V) obtained from measurements of low doped Ni/4*H*-SiC.

Analysing Equation 3.28, one obtains

$$\frac{d(1/C^2)}{dV} = \frac{2}{eN_D\epsilon_s} \tag{3.29}$$

Thus a gradient of the $1/C^2$ against V_{ext} graph gives the net carrier concentration while the Schottky barrier height is determined from the voltage intercept using equation [15]

$$\Phi_{Bn} = V_{bi} - V_{ext} - \beta^{-1} \tag{3.30}$$

The Schottky barrier height is obtained with minimum error if the $1\ /\ C^2$ against V_{ext} graph is a straight line.

3.4 Ohmic contacts

Schottky contacts are rectifying, hence very important metal semiconductor contacts. Ohmic contacts are also very important in semiconductor device fabrication. A good ohmic contact should allow current flow with a very small voltage drop relative to the voltage drop that takes place across the device active region. Sze [3] defines ohmic contacts as metal semiconductor contacts with negligible contact resistance compared to the total device resistance. The specific contact resistance, R_C is defined as the resistance of the contact at zero applied voltage [16], and can be expressed as [17]

$$R_C = \left(\frac{\partial I}{\partial V}\right)^{-1}_{V=0} \tag{3.31}$$

The total contact resistance (R) for an ohmic contact with area A is given by [3]

$$R = \frac{R_C}{A} \tag{3.32}$$

For a metal-semiconductor contact to have very low contact resistance, it must have either a small barrier height or very high doping density or both [15]. It is difficult to produce a small barrier height as metals with sufficiently small work function may not be generally available [3]. Engineering of a small barrier height is also difficult as the barrier height is not always determined by the metal work function alone as discussed in sections 3.2.2 and 3.2.3. The difficulty in barrier height engineering leaves the net doping density as the main basis for successful ohmic contact fabrication.

The doping density does not have an effect on the barrier height but does affect the barrier width [15]. Heavily doped semiconductors have a narrow barrier and charge transport across the barrier can easily take place in form of tunnelling.

A parameter that can be used to determine the dominant current transport mechanisms for differently doped semiconductors is the characteristic energy, E_{00} defined by [18]

$$E_{00} = \frac{eh}{4\pi}\sqrt{\frac{N_D}{m^*\epsilon_s}} \tag{3.33}$$

where h is Planck's constant and m^* is the effective tunnelling mass. Figure 3.7 graphically represents the variation of E_{00} with net doping density.

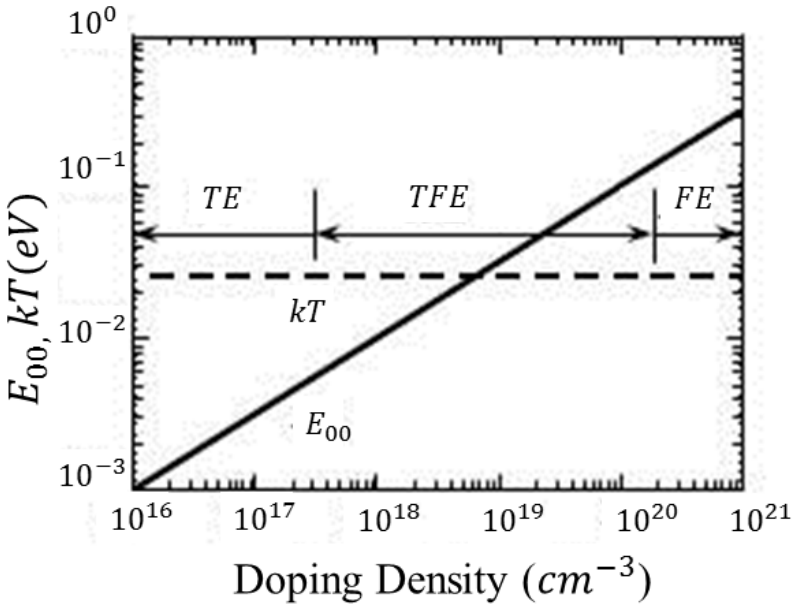

Figure 3.7 Thermionic emission, thermionic field emission and Field emission dominant dependency on doping density for silicon. Diagram adapted from ref. [15].

Where the doping density is small, thermionic emission (TE) is dominant and $E_{00} \ll k_B T$. In such a case, the contact resistance is given by [2, 3]

$$R_C = \frac{k_B}{eA^*T} exp\left(\frac{\Phi_{Bn}}{k_B T}\right) \tag{3.34}$$

where A^* is the Richardson constant. The equation shows that in the case of lightly doped semiconductors, a small barrier height is necessary to produce a small contact resistance.

For moderately doped semiconductors ($E_{00} \approx k_B T$), thermionic field emission (TFE) is dominant and electrons are thermally excited to energies where the barrier is sufficiently narrow for tunnelling to occur. With TFE being the dominant current transport mechanism, the contact resistance is given by [3]

$$R_C \propto exp\left[\frac{e\Phi_{Bn}}{E_{00} coth\left({}^{E_{00}}/_{k_B T}\right)}\right] \quad 3.35$$

Tunnelling current is the dominant current transport mechanism for highly doped semiconductors where ($E_{00} \gg k_B T$). The contact resistance in this regime is given by [2]

$$R_C \propto exp\left(\frac{e\Phi_{Bn}}{E_{00}}\right) \quad 3.36$$

As the doping increases, the contact resistance exponentially decreases. Ohmic contacts should be fabricated using highly doped semiconductors in order to achieve this low contact resistance as it is difficult to modify barrier heights. Mostly epitaxial semiconductors grown on heavily doped semiconductors are used in the fabrication devices that require ohmic contacts. Ohmic contacts are made on the heavily doped side while Schottky diodes are made on the lightly doped semiconductor side.

3.5 Current transport mechanisms

Majority carriers, i.e. electrons in *n*-type semiconductors and holes in *p*-type semiconductors are responsible for conduction across metal-semiconductor junctions. Current transport occurs through different mechanisms, illustrated in Figure 3.8. Thermionic emission (TE) which is dominant for lightly doped semiconductors is the emission of electrons over the Schottky barrier from the semiconductor into the metal. Quantum mechanical tunnelling is dominant for highly doped semiconductors such that the barrier is sufficiently thin. Tunnelling can be ‘pure’ tunnelling [2] or field emission (FE) where electrons energies are close to the (quasi) Fermi level. Other mechanisms responsible for current transport are recombination in the space charge region and hole injection from the metal [2, 3, 17]. Experiments done in this thesis were based on low doped SiC. As such, thermionic emission is supposed to be the dominant current transport process for Schottky diodes fabricated thereon. The different mechanisms will be discussed in Sections 3.5.1 and 3.5.2.

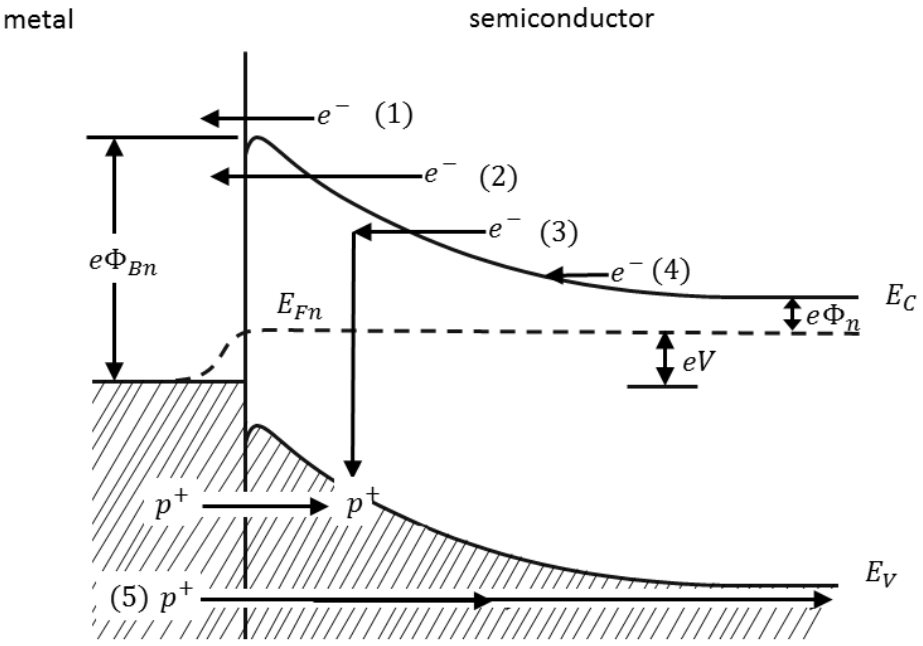

Figure 3.8 Basic current transport mechanisms across a forward biased Schottky barrier. (1) Thermionic emission. (2) Tunnelling. (3) Recombination. (4) Diffusion of electrons. (5) Diffusion of holes. Diagram has been redrawn from refs. [2, 3].

3.5.1 Thermionic emission

The TE theory has its basis in several assumptions which are: (1) the Schottky barrier height is large compared to the product k_BT, (2) there is thermal equilibrium at the plane that determines emission and (3) this equilibrium is not affected by the net current flow hence one can superimpose the two current fluxes, from semiconductor to metal and from metal to semiconductor, each with a different quasi Fermi level [3].

Current density from the semiconductor to the metal ($J_{S\rightarrow M}$) is determined by the number of electrons that have enough energy to cross over the barrier and are moving from the semiconductor into metal, i.e.

$$J_{S\rightarrow M} = \int_{E_{Fn}+e\Phi_{Bn}}^{\infty} ev_x dn \qquad 3.37$$

$E_{Fn} + e\Phi_{Bn}$ is the minimum energy necessary for thermionic emission to take place, v_x is the carrier velocity in the direction of current flow and is obtained from [2]

$$E = E_C + \frac{1}{2}m^*v^2 \qquad 3.38$$

where m^* is the effective mass. dn is the electron density in a small energy interval (dE) and is given by [2]

$$dn = N(E)F(E)dE \tag{3.39}$$

where $N(E)$ is the effective density of states and $F(E)$ is the distribution function. Using Equations 3.38 and $dE = m^*vdv$, Equation 3.39 can be written as [2, 3]

$$dn \approx 2\left(\frac{m^*}{h}\right)^3 exp\left(-\frac{e\Phi_n}{k_BT}\right) exp\left(-\frac{m^*v^2}{2k_BT}\right)(4\pi v^2 dv) \tag{3.40}$$

Equation 3.40 gives the number of electrons per unit volume with velocities between v and $v + dv$ distributed in all directions. h is Planck's constant. Using the transformation $4\pi v^2 dv = dv_x dv_y dv_z$ and integrating over all velocities in y and z directions and v_x from minimum velocity required to overcome the barrier to ∞, the current density is given by [2, 3]

$$J_{S\to M} = \frac{4\pi e m^* k_B^2}{h^3} T^2 exp\left(-\frac{\Phi_{Bn}}{k_BT}\right) exp(\beta V) \tag{3.41}$$

A constant $A^*(= 120 Acm^{-2}K^{-2}$ for vacuum) which is the Richardson constant, is introduced and Equation 3.41 is rewritten as

$$J_{S\to M} = A^*T^2 exp\left(-\frac{\Phi_{Bn}}{k_BT}\right) exp(\beta V) \tag{3.42}$$

Equations 3.41 and 3.42 give the current density as determined by thermionic emission when moving from the semiconductor into the metal. When a forward voltage is applied across the diode, the energy difference between the quasi Fermi level and the top of the barrier is reduced hence the thermionic emission current is increased as more electrons will have enough energy to surmount the barrier.

However, if the junction is reverse biased, the energy difference is increased and the thermionic emission current is then decreased. The barrier 'seen' by electrons moving from the metal into the semiconductor is not changed by biasing conditions hence the current remains unchanged in this direction. Figure 3.5 shows the effect of different biasing conditions on the barrier height as 'seen' by electrons moving from the semiconductor into the metal.

The current-voltage relationship in the thermionic emission theory is given by the equation

$$J_{S\to M} = A^*T^2 exp\left(-\frac{\Phi_{Bn}}{k_BT}\right)[exp(\beta V) - 1] \quad 3.43$$

$$= J_s[exp(\beta V) - 1] \quad 3.44$$

where $J_s = A^*T^2 exp\left(-\frac{\Phi_{Bn}}{k_BT}\right)$ is the saturation current density [6]. The saturation current is strongly dependent on temperature and barrier height. The equation for the saturation current density can be rewritten in the form

$$ln\left(\frac{J_s}{T^2}\right) = ln(A^*) - \frac{\Phi_{Bn}}{k_BT} \quad 3.45$$

A plot of $\ln(J_s/T^2)$ against $1/T$ can thus be used to determine the barrier height from the gradient while the Richardson constant is obtained from the $\ln(J_s/T^2)$ intercept. Such a plot is commonly refered to as the Richardson plot.

Two methods for Schottky barrier height determination have been discussed, i.e. from capacitance-voltage and current-voltage measurements. These are the two methods used in this thesis although there are other determination methods such as capture barrier measurements and photoelectric measurements [3].

If the image force lowering of the barrier height is considered, Equation 3.44 is modified by the introduction of a dimensionless quantity, n, the ideality factor to

$$J = J_s\left[exp\left(\frac{eV}{nk_BT}\right) - 1\right] \quad 3.46$$

The ideality factor is given by the formula [3]

$$n = \frac{e}{k_BT}\frac{dV}{d(lnJ)} \quad 3.47$$

The ideality factor can therefore be obtained from the slope of semi-logarithmic *I-V* curves obtained from the diode characteristics. If the current transport is perfectly described by the thermionic emission model, the quantity n is equal to unity. The ideality factor is therefore used to quantify the deviation of the transport mechanisms from the TE model when used as in Equation 3.46. Other anomalies such as barrier unevenness are also included in the ideality factor [15].

3.5.2 Tunnelling current

Tunnelling processes are responsible for current transport when the Schottky barrier is sufficiently thin, a case for highly doped semiconductors as well as at low temperatures where electrons do not have sufficient energy for thermionic emission to take place [2, 19, 20]. Tunnelling processes can be analysed for different temperature regimes: very low temperature, and high temperatures but not high enough for thermionic emission to take place.

3.5.2.1 Field Emission

When the temperature is very low, electron tunnelling occurs close to the semiconductor Fermi level. This process is known as field emission (*FE*) and is important in degenerate semiconductors [2]. Where the *FE* process is dominant, the forward current process is given by

$$J = J_s exp\left(\frac{eV}{E_{00}}\right) \tag{3.48}$$

E_{00} has been defined by Equation 3.33. The saturation current, J_s in this regime is given by the equation [19]

$$J_s \propto exp\left(-\frac{\Phi_{Bn}}{E_{00}}\right) \tag{3.49}$$

Under reverse biasing conditions, the current-voltage characteristics for the *FE* regime are given by [2]

$$J = \frac{4e\pi m^*}{h^3} E_{00}^2 \frac{e(V_{bi} - V)}{\Phi_{Bn}} exp\left(-\frac{2\Phi_{Bn}^{3/2}}{3E_{00}\sqrt{e(V_{bi} - V)}}\right) \tag{3.50}$$

3.5.2.2 Thermionic Field Emission

Thermionic field Emission (*TFE*) occurs when the temperature increases such that electrons are excited to levels where the barrier is sufficiently thin for tunnelling to occur [2]. Here the current characteristics are given by

$$J = J_s exp\left(\frac{eV}{E_0}\right) \quad 3.51$$

where E_0 is obtained from E_{00} using

$$E_0 = E_{00} coth\left(\frac{E_{00}}{kT}\right) \quad 3.52$$

Detailed discussions of the *FE* and the *TFE* mechanisms can be obtained from [19, 20].

References

[1] W. Monch, *Electronic Structure of Metal-Semiconductor Contacts*, Kluwer Academic, Dordrecht, 1990.

[2] M. Grundmann, *The Physics of Semiconductors An Introduction Including Nanophysics and Applications*, Second ed., Springer, Berlin Heidelberg, 2010.

[3] S. M. Sze, *Physics of Semiconductor Devices*, Third ed., John Wiley & Sons, New Jersey, 2007.

[4] M. Schluter, Theoretical models of Schottky barriers, Thin Solid Films, **93** (1982) 3.

[5] I.P. Batra, E. Tekman, S. Ciraci, Theory of Schottky Barrier and Metallization, Progress in Surface Science, **36** (1991) 289.

[6] B.J. Baliga, *Advanced Power Rectifier Concepts*, First ed., Springer Scientific, New York, 2009.

[7] L.M. Porter, R.F. Davis, A critical review of ohmic and rectifying contacts for silicon carbide, Materials Science and Engineering: B, **34** (1995) 83.

[8] R.T. Tung, Recent advances in Schottky barrier concepts, Materials Science and Engineering: R: Reports, **35** (2001) 1.

[9] C.R. Crowell, S.M. Sze, Current transport in metal-semiconductor barriers, Solid-State Electronics, **9** (1966) 1035.

[10] C.A. Mead, Metal-semiconductor surface barriers, Solid-State Electronics, **9** (1966) 1023.

[11] J. Bardeen, Surface States and Rectification at a Metal Semi-Conductor Contact, Physical Review, **71** (1947) 717.

[12] C.Y. Chang, S.M. Sze, Carrier transport across metal-semiconductor barriers, Solid-State Electronics, **13** (1970) 727.

[13] M. Schmidt, 'Space Charge Spectroscopy applied to Defect Studies in Ion-Implanted Zinc Oxide Thin Films', Ph.D. Thesis, Universitat Leipzig, Leipzig, 2010.

[14] H. Czichos, T. Saito, L. Smith, *Springer Handbook of Metrology and Testing*, Second ed., Springer, Berlin Heidelberg, 2011.

[15] D.K. Schroder, *Semiconductor Material & Device Characterization*, Third ed., John Wiley and Sons, New Jersey, 2006.

[16] J.W. Mayer, S.S. Lau, *Electronic Material Science For Integrated Circuits in Si and GaAs*, Macmillan Publishing, New York, 1990.

[17] M. Jang, J. Lee, Analysis of Schottky Barrier Height in Small Contacts Using a Thermionic-Field Emission Model, ETRI Journal, **24** (2002) 455.

[18] S. Chand, J. Kumar, Current transport in Pd2 Si/n-Si(100) Schottky barrier diodes at low temperatures, Applied Physics A, **63** (1996) 171.

[19] F.A. Padovani, R. Stratton, Field and thermionic-field emission in Schottky barriers, Solid-State Electronics, **9** (1966) 695.

[20] C.R. Crowell, V.L. Rideout, Normalized thermionic-field (T-F) emission in metal-semiconductor (Schottky) barriers, Solid-State Electronics, **12** (1969) 89.

CHAPTER 4

Ion Implantation and radiation damage

4.1 Introduction

Ion implantation is an essential part of this work as alpha particle, electron and proton irradiations were carried out on the studied SiC samples. It is therefore important to have a background understanding of the interactions that take place between ions and semiconductors. This chapter discusses the energy loss processes (nuclear and electronic) as an ion interacts with the lattice, section 4.2. Section 4.3 gives the ion range distributions and section 4.4 discusses the ion induced damage and recovery due to annealing treatments.

4.2 Energy - loss processes

Two major types of interactions are responsible for stopping an ion beam interacting with matter and these are electronic interactions/collisions and nuclear interactions [1-3]. These two processes are both responsible for the stopping although each is dominant under different ion beam conditions such as ion mass, ion velocity and ion energy [4]. Taking $(dE/dx)_n$ as the rate of energy loss due to nuclear interactions and $(dE/dx)_e$ as the rate of energy loss due to electronic interactions, then the total energy loss rate is given as [2]

$$\frac{dE}{dx} = \left(\frac{dE}{dx}\right)_n + \left(\frac{dE}{dx}\right)_e \qquad 4.1$$

where x is the beam penetration depth. It will be mentioned at this point that energy loss due to nuclear collisions is dominant at low ion velocities or low ion energies while at high ion energies, it is electronic energy loss that dominates as illustrated graphically in Figure 4.1. The rate of energy loss dE/dx can be converted into a stopping cross section S by use of the equation: $S = N^{-1}(dE/dx)$ where N is the target electron density. The total stopping cross section is then given as:

$$S = \frac{1}{N}\left[\left(\frac{dE}{dx}\right)_n + \left(\frac{dE}{dx}\right)_e\right] = \frac{1}{N}(S_n + S_e) \qquad 4.2$$

where S_n and S_e are the nuclear and electronic cross sections respectively.

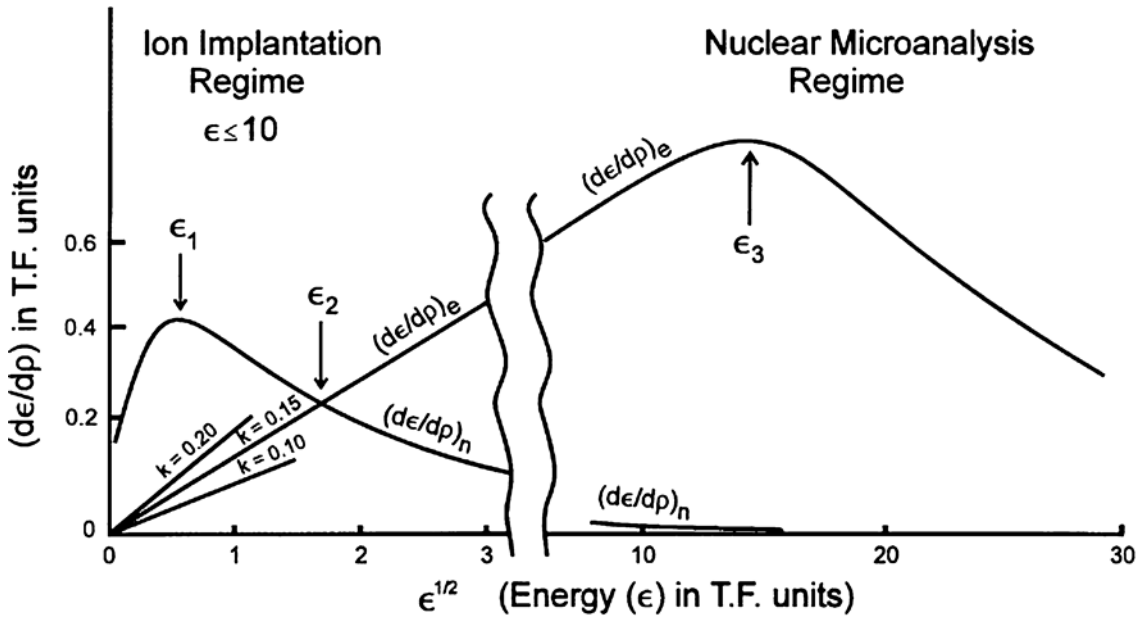

Figure 4.1 Nuclear stopping and Electronic stopping energies as a function of reduced energy. Diagram from *ref*. [5].

4.2.1 Nuclear stopping

Also known as elastic (from energy conservation) stopping, nuclear stopping results from the interaction of ions with the nuclei of target atoms [6]. The nuclear stopping component is dominant when ion particles are of high mass and low energy [1]. Since nuclear stopping is dominant at low energies, it therefore takes place at the end of the ion trajectories (deeper in the material), hence this is the region where ion induced damage occur [4].

In nuclear stopping, an ion may lose a lot of energy from a single collision and change its direction considerably. The energy transferred, T to a stationary target atom due to a collision is given by [7]

$$T = \frac{4M_1M_2E}{(M_1+M_2)^2} sin^2\frac{\theta_c}{2} \qquad 4.3$$

where M_1 and M_2 are the ion and target masses respectively, and θ_c is the scattering angle in the centre of mass frame of reference. This expression for transferred energy is integrated over a differential cross section, $d\sigma$ to give the stopping power $S_n(E)$ as

$$S_n(E) = \int_0^{T_{max}} T d\sigma \qquad 4.4$$

Equation 4.4 is simplified to give for practical calculations, the universal stopping power as [8]

$$S_n(E) = \frac{8.462 \times 10^{-15} Z_1 Z_2 M_1 S_n(\varepsilon)}{(M_1 + M_2)(Z_1^{.23} + Z_2^{.23})} eV/(atom/cm^2) \quad 4.5$$

where ε is the reduced energy. More detailed derivations and explanations of the nuclear stopping power can be found in Ziegler *et al*. [8] or from Rimini *et al*. [7].

4.2.2 Electronic stopping

Electronic/inelastic stopping result from the coulomb interaction of the ion with the electron cloud of the target atoms [7]. The stopping is referred to as inelastic since energy may be lost due to excitation of bound electrons from the target material atoms or excitation of electron cloud of the ion [4, 7-9]. The inelastic energy loss for moderately relativistic particles can be represented by the Bethe-Bloch equation [10]

$$S_e(E) = K{Z_1}^2 \frac{Z_2}{A} \frac{1}{\beta^2} \left[\frac{1}{2} \frac{2 m_e c^2 \beta^2 \gamma^2 T_{max}}{I^2} - \beta^2 - \frac{\delta(\beta\gamma)}{2} \right] \quad 4.6$$

where T_{max} is the maximum amount of energy that can be transferred to an electron after a single collision, m_e is mass of an electron, c is the speed of light, Z_1 is the atomic number of incident particle, Z_2 is the atomic number of target material, I is the mean excitation energy and $\delta(\beta\gamma)$ is defined as the density effect correction to ionization energy loss. $K/A = 4\pi N_A r_e^2 m_e c^2/A$ with N_A being Avogadro's number, A is the atomic mass of target atom and r_e being a classical electron radius. It is important to note the direct dependency of the electronic stopping power on Z_1 and Z_2.

For amorphous solids, deceleration of an ion beam is purely statistical.

4.3 Ion range distributions

The range R is a beam's total track length before coming to rest [5, 11]. An ion propagating in the incident lattice will be involved in a series of collisions with host atoms leading to a non-linear propagation. The total distance, R travelled by ions of the same energy and angle of incidence is therefore not always the same due to different interactions with the host material. The range is therefore of less practical significance and a parameter of more practical significance is the projected range, R_p which gives beam's mean penetration depth

with respect to the surface [5, 11]. The difference between these two parameters is shown in Figure 4.2.

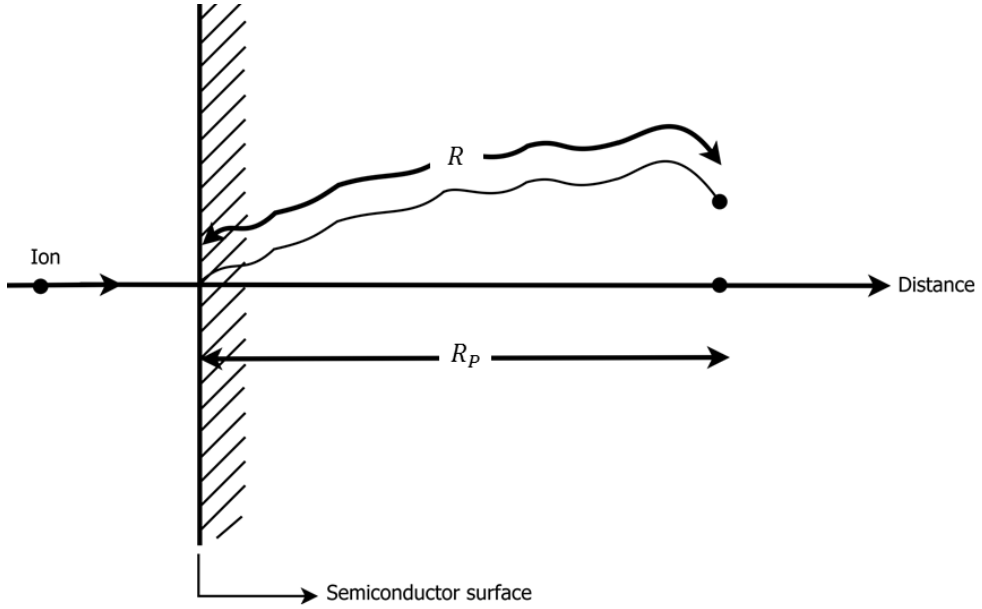

Figure 4.2 Total path length (R) and projected range (R_P) of an incident ion in a semiconductor material. Diagram redrawn following *ref.* [3].

Knowing the nuclear and electronic stopping cross sections, the range is obtained from the expression [5, 12, 13]

$$R = \int_{E_0}^{0} \frac{1}{dE/dx} dE \tag{4.7}$$

For heavier ions where $M_1 \geq M_2$, R_p is obtained by scaling R with the projection factor, approximately equal to $(1 + M_2/3M_1)^{-1}$ [5]. A more complex treatment is needed for crystalline semiconductors as channelling effects may occur. The angle of incidence has an influence on the projected range. For near normal incidence, $R_p \approx R$ and the depth distribution, $N(x)$ can be modelled by Gaussian distribution as [2, 3]

$$N(x) = \frac{\phi}{(2\pi)^{1/2}\Delta R_p} exp\left[-\frac{1}{2}\left(\frac{x - R_p}{\Delta R_p}\right)^2\right] \tag{4.8}$$

where ϕ is the total implantation ion fluence and ΔR_p is the projected range straggling (standard deviation of the distribution). With all implanted ions being retained, the relation between the ion depth distributions and the total fluence is given by [3]

$$\phi = \int_{-\infty}^{\infty} N(x)\, dx \tag{4.9}$$

The projected range and other implantation profiles can be simulated using Monte-Carlo based techniques. Figure 4.3 shows alpha particle depth projections obtained from Monte-Carlo simulations. The simulation shows the effect of alpha particle particle collisions with SiC lattice atoms as well as wide range of projected ranges that may result from the implantation.

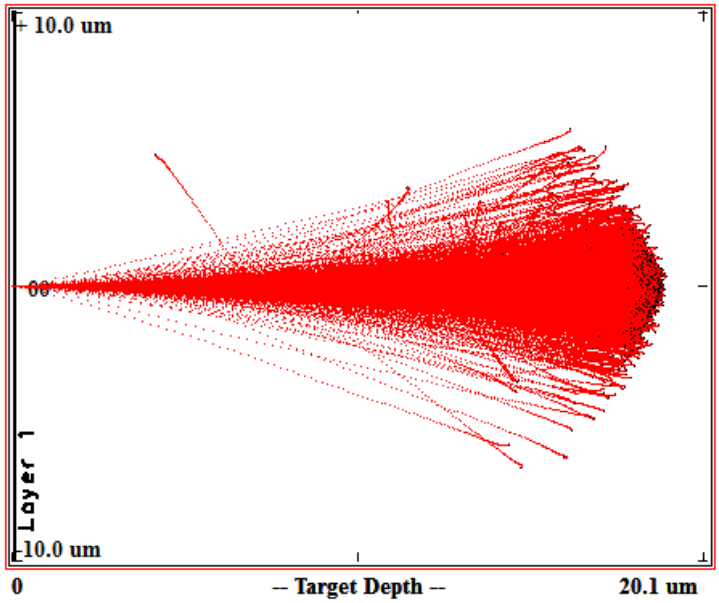

Figure 4.3 Monte-Carlo simulation of 5.4 MeV alpha particles onto a Ni/4H-SiC Schottky diode.

4.4 Radiation damage

Due to nuclear interactions, the ion gives off some of its energy, E to a target atom. If the ion energy is high enough ($E_d < E < 2E_d$), atomic displacements and interstitials can occur. Vacancies and interstitials are formed for higher ion energies where the condition $E > 2E_d$ is fulfilled [5]. E_d is the displacement energy, which is the minimum energy required to displace an atom from its lattice position. If E is however less than E_d, then the transferred energy can only cause the target atom to oscillate with a large amplitude about its lattice position without the creation of a vacancy [3].

A cascade of collisions can be created if the displaced atom has enough energy to displace other atoms and there is a continuation of the process. This process creates vacancies, interstitials, amorphous regions and a possibility of extended defects [3, 11]. A cascade of collisions that can result from such collisions is illustrated in Figure 4.4.

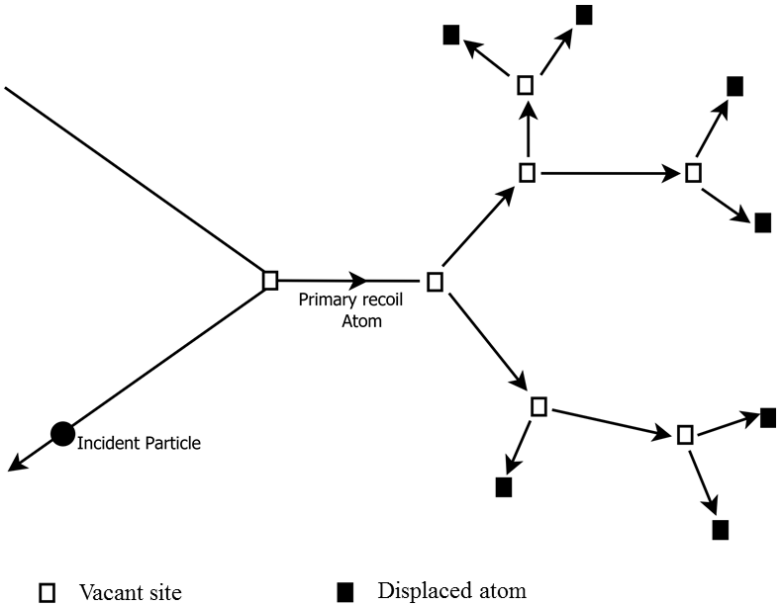

Figure 4.4 Schematic of a cascade of collisions. Diagram redrawn from *ref*. [3].

References

[1] S. Cabrini, S. Kawata, *Nanofabrication Handbook*, First ed., CRC Press, Danvers, 2012.

[2] L. Pavesi, R. Turan, *Silicon Nanocrystals*, First ed., John Wiley & Sons, Weinheim, 2010.

[3] M. Nastasi, J.W. Mayer, First ed., *Ion Implantation and Synthesis of Materials*, Springer, Berlin Heidelberg, 2006.

[4] B. Schmidt, K. Wetzig, *Ion Beams in Materials Processing and Analysis*, Springer Science & Business Media, Wien, 2012.

[5] F. D. Auret, Deenapanray, N.K. Prakash, Deep Level Transient Spectroscopy of Defects in High-Energy Light-Particle Irradiated Si, Critical Reviews in Solid State and Materials Sciences, **29** (2004) 1.

[6] Dietmar Fink, L.T. Chadderton, Ion-Solid Interaction: Status and Perspectives, Brazilian Journal of Physics, **35** (2005) 735.

[7] E. Rimini, *Ion Implantation: Basics to Device Fabrication*, First ed., Springer Science & Business Media, Massachusetts, 1995.

[8] J. F. Ziegler, J. P. Biersack, M.D. Ziegler, *SRIM, the Stopping and Range of Ions in Matter*, First ed., Lulu.com, Maryland, 2008.

[9] P. D. Townsend, P. J. Chandler, L. Zhang, *Optical Effects of Ion Implantation*, First ed., Cambridge University Press, USA, 2006.

[10] H. Bichsel, D.E. Groom, S.R. Klein, *Passage of particles through matter 1*, University of Washington, 2007.

[11] J.W. Mayer, S.S. Lau, *Electronic material science For Integrated Circuits in Si and GaAs*, Macmillan Publishing company, New York, 1990.

[12] A. Galdikas, L. Praniavichius, *Interaction of Ions with Condensed Matter*, First ed., Nova Publishers, New York, 2000.

[13] J.F. Gibbons, Ion Implantation in Semiconductors-Part I, Range Distribution Theory and Experiments, IEE, **56** (1968) 295.

CHAPTER 5

Defects in semiconductors

5.1 Introduction

All semiconductors contain defects [1]. Defects can be defined as any form of deviation from a perfect crystal lattice. One type of imperfection that semiconductors have in common is thermal atomic vibrations at any temperature above 0 K [2]. Another common type of defects contained in semiconductors is impurities. These are introduced intentionally to modify the conductivity of the semiconductors.

Defects can be broadly classified into either intrinsic defects or extrinsic defects. Intrinsic defects refer to irregularities in the crystal arrangements of atoms in the lattice and these can be further classified according to dimensionality. On the other hand, extrinsic defects involve the incorporation of impurities which are then the defects, and the incorporation can be intentional or unintentional. Impurity defects lead to another dimensionality in defect classification where an impurity can introduce either a shallow defect or a deep level defect.

This chapter looks at the different types of defects that are found in semiconductors, classifying them according to intrinsic and extrinsic defects, sections 5.2 through to 5.4. Section 5.5 discusses donor and acceptor levels that are found specifically in SiC. Deep levels are discussed in section 5.7 with a mathematical description being presented. The main measurement technique used in this study is DLTS. The theoretical basis of this technique is provided in section 5.8.

5.2 Intrinsic defects

As mentioned earlier, intrinsic defects result from a “mistake” in the atomic arrangements of atoms within the lattice. Classifying them according to dimension, intrinsic defects are point defects (zero dimension), line defects / dislocations (one dimensional), plane defects (two dimensional) and volume defects (three dimensional). A brief simple discussion of these types of defects follows according to the dimensional hierarchy.

5.2.1 Point defects

Point defects, being zero dimensional are the simplest types of defects to visualise. Point defects are predominantly vacancies, interstitials and antisites.

Vacancies refer to a missing atom from a lattice position. In silicon carbide, there can be a silicon vacancy, V_{si}, where a silicon atom is missing from a lattice position or a carbon vacancy V_c, where a carbon atom is missing from a lattice position. In the formation of a vacancy, four bonds are broken. In addition to simple vacancies, there can be a divacancy where two adjacent atoms are missing from the lattice positions and here only six bonds are broken [3]. It is important to note that the mobility of monovacancies is very low in silicon carbide due to its stronger chemical bonding thus these defects are very stable at room temperature to temperatures below 1400 °C [2, 4]. During the formation of a vacancy, the atom may leave its lattice position and migrate to the surface. If the atom does not migrate to the surface, it may occupy an interstitial position to become an interstitial defect. In SiC there can be either a silicon interstitial I_{si} or a carbon interstitial I_c. If the interstitial defect is close to the vacancy defect, the vacancy-interstitial arrangement is known as a Frenkel pair.

In compound semiconductors, it is also common to find a point defect in the form of an antisite. This is a defect where a lattice position is occupied by a different atom thereby disrupting the pattern of the semiconductor atomic arrangement. In SiC for example, a lattice position that should be occupied by a silicon atom may be occupied by a carbon atom and this would be a carbon antisites denoted as C_{Si}, while a silicon antisite is denoted Si_C. Because of the nature of antisites, these are not possible in elemental semiconductors. In SiC, antisite defects may be the most common point defects since silicon and carbon belong to the same lattice column of the periodic table [5]. Figure 5.1 schematically illustrates some of the point defects in a SiC lattice.

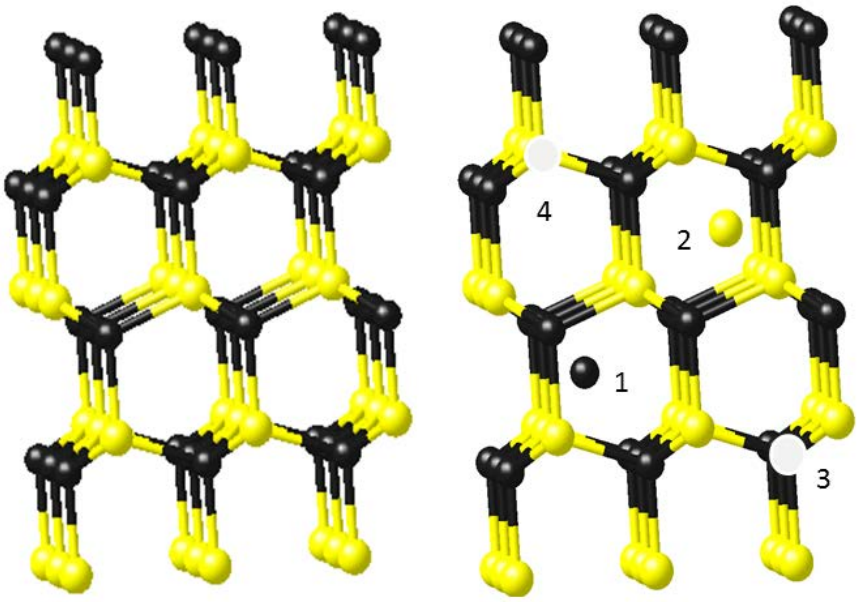

Figure 5.1 (a) A perfect SiC lattice and (b) A lattice containing intrinsic point defects: (1) carbon interstitial, (2) silicon interstitial, (3) V_c and (4) V_{si}.

5.2.2 Line defects

A line defect is also known as a dislocation and can be in two forms: an edge dislocation or a screw dislocation. Dislocations can be explained as discontinuities in the lattice [6]. Dislocations are best defined in terms of a Burgers circuit. A burgers circuit in a dislocation containing crystal is an atom to atom path which contains a closed loop [7]. A Burgers vector is required to complete the one to one Burgers circuit. The direction of a Burgers vector depends on whether the dislocation is line or screw in nature.

5.2.2.1 Edge dislocation

The distortion of a crystal due to an edge dislocation can be considered to be due to an insertion of an extra plane of atoms part way into a crystal [8]. Figure 5.2 illustrates an edge dislocation. The distortion due to an edge dislocation is concentrated close to the dislocation line (*core* of the dislocation) while the lattice is nearly perfect a few atoms distance away from the dislocation centre. A region far from the core of the dislocation is only slightly strained and is referred to as the elastic region [8]. In a line dislocation, the Burgers vector is normal to the line of the dislocation.

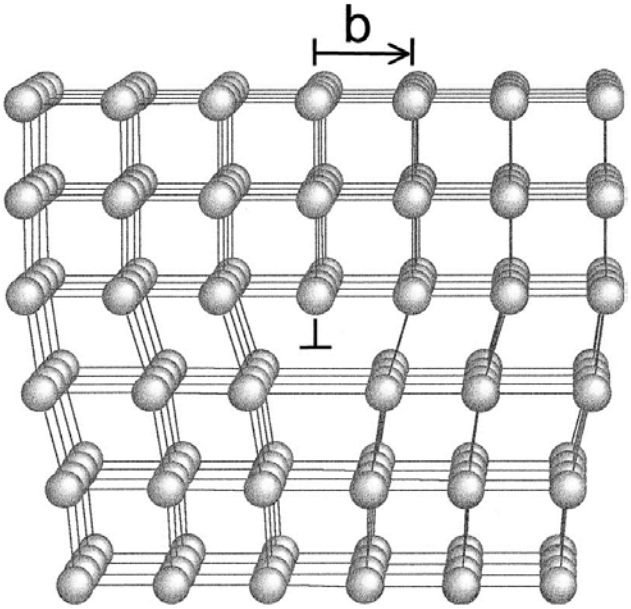

Figure 5.2 Edge dislocation schematic from *ref*. [9].

5.2.2.2 Screw dislocation

A screw dislocation is one where the direction of the Burgers vector is parallel to the line of dislocation [7]. A screw dislocation can be explained by imagining a sharp cut being made part way through a crystal and lifting the material on one side of the cut by one atomic spacing. If the rows of atoms are then placed back into contact, then the resulting crystal is said to have a screw dislocation and is schematically represented in Figure 5.3.

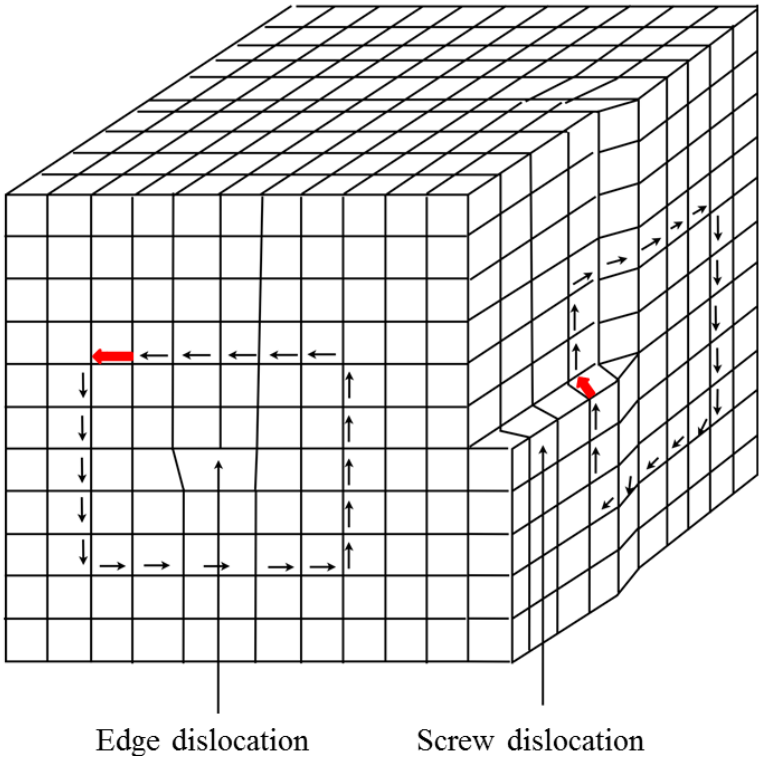

Figure 5.3 Screw and Edge dislocations illustration redrawn from *ref*. [10]. Arrows indicate the Burgers vectors associated with the Screw and Edge dislocations.

5.3 Planar defects

A change/disruption in the stacking sequence of a material is a plane defect. If the sequence disruption extends over a few atomic distances then the defect is a stacking fault and if the disruption is over several atomic distances, then the defect becomes a twin boundary. A plane defect can also be in the form of a grain boundary which exists where a crystal is not a single crystal but mostly in polycrystalline materials.

A stacking sequence such as ABCABC…. can be disrupted such that an A layer occupies either a B or a C position as this is geometrically allowed. The sequence disruption can either be due to a removal of one layer or due to an addition of an extra layer, Figure 5.4. The removal of a layer or part thereof can be explained as leading to an intrinsic stacking fault while a stacking fault that results from the addition of an extra layer is generally referred to as an extrinsic stacking fault as the added layer does not belong to the continuing patterns of layers [7]. Stacking faults in SiC devices are said to cause degradation of electrical characteristics and a reduction in the carrier lifetime [11, 12].

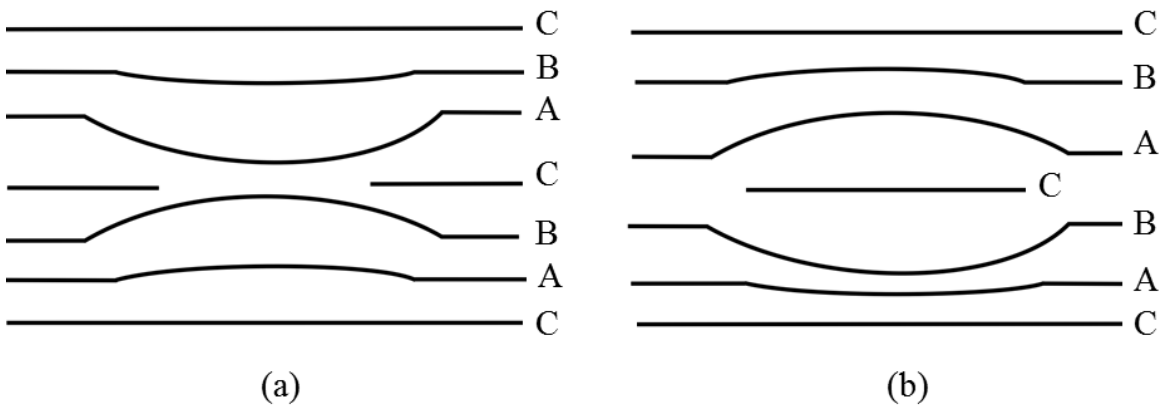

Figure 5.4 Schematic of different stacking fault. Diagram redrawn from ref. [6].

5.4 Volume defects

Volume defects, also known as bulk defects are types of defects that extend in three dimensions. Voids which are a cluster of vacancies are one example of volume defects. Impurities can also accumulate in a region to form precipitates which are another form of volume defects.

5.5 Extrinsic point defects

So far, only intrinsic point defects have been discussed, section 5.2.1. In addition, there are also extrinsic point defects which are impurities found within the semiconductor. These may be intentionally introduced in controlled concentrations during growth by diffusion or after growth by means of ion implantation to modify the conductivity of the material. Impurities can also be incorporated into a semiconductor unintentionally during growth, and this can be regarded as contamination. After being introduced into the semiconductor, impurities can either occupy an interstitial position or they can displace a native atom from a lattice position to become either a donor or an acceptor depending on whether it has more or less valence electrons compared to the displaced atom.

Nitrogen is the standard dopant for *n*-type SiC, although oxygen and phosphorous can also be used to enhance *n*-type conductivity [13]. Other common *n*-type dopants for SiC are indium and arsenic[14]. In general, substitutional impurities that have more than four valence electrons can be used for *n*-type conductivity in SiC. After substituting native atoms from the lattice positions, group V and group VI atoms donate extra valence electrons to the conduction band which then participate in *n*-type conductivity, hence they are called donors.

SiC can also be doped with group III atoms if *p*-type conductivity is desired. Aluminium and boron are the most commonly used dopants for *p*-type SiC. Since group III elements have one-less valence electron as compared to either silicon or carbon, after occupying a lattice position they need one more electron to complete the bonds and are thus called acceptors.

5.5.1 Donors in SiC

Nitrogen atoms are assumed to substitute carbon atoms in the SiC lattice [15] and are therefore the main forms of impurity point defects in *n*-type SiC. Nitrogen donors in SiC will be discussed in section 5.6.1. Other than nitrogen, other group V elements such as phosphorus and arsenic can be used in the doping of SiC. It therefore follows that these elements can be found in SiC as donors if they are used for doping and can then be regarded as point defects.

Phosphorous for instance has been found to introduce a shallow donor with an ionisation energy of $53.93\,meV$ [14]. Other researchers reported two phosphorous related levels in 4*H*-SiC after phosphorous implantation. These were observed at $53\,meV$ and at $93\,meV$ below the conduction band and were assigned to hexagonal and cubic positions respectively [16].

Because oxygen has two more electrons in the outer-most shell compared to either silicon or carbon, oxygen is a double donor if it displaces carbon from the lattice position, which would also be the case was it to displacing silicon. After oxygen implantation, Dalibor et al found two shallow donor-like centres in 4*H*-SiC with ionisation energies of $(2.99-3.03)\,eV$ and at $(2.84-2.88)\,eV$ above the valence band [17, 18]. These authors also show that oxygen introduces shallow donor-like centres in 6*H*-SiC with ionization energies of $(2.85-2.87)\,eV$ and $(2.80-2.82)\,eV$ above the valence band [13].

5.5.2 Acceptors in SiC

Aluminium is the preferred *p*-type dopant for SiC and it substitutes silicon in the lattice [19]. The ionisation energy of aluminium impurities in 4*H*-SiC were found to be $168\,meV + E_x$, where E_x is the exciton binding energy [5]. Other group III elements such as boron and gallium have also been observed to introduce shallow acceptor levels in 4*H*-SiC with ionisation energies of $628\,meV + E_x$ [20] and $290\,meV$ respectively [21].

In addition to group III elements, oxygen also introduces deep acceptor-like levels in SiC. In 4*H*-SiC, if oxygen substitutes a silicon atom from the lattice position, the resultant point defect is a double donor hole trap with energies of 1.0 eV and 1.1 eV above the valence band [18].

5.5.3 Transition metals in SiC

SiC unavoidably contains transition metal impurities, mostly titanium, vanadium and chromium especially if it is Lely-process grown [22]. These transition metals introduce both deep acceptor states and deep donor states in SiC. Several authors have done implantation studies to study transition metal defects in SiC, mostly the 6*H*- polytype. Dalibor et al [23] did extensive transition metal implantation studies on the introduced deep level states in SiC.

In 4*H*-SiC, vanadium was shown to introduce an acceptor-like defect at $E_C - (880\ to\ 970)\ meV$ from DLTS [24]. Achtziger *et al.*[25] performed DLTS on 4*H*-SiC after recoil implantation with radioactive metals and obtained a vanadium related level at $E_C - 970\ meV$ which is in agreement with the results presented by Dalibor et al.

Titanium introduces deep acceptor states in 4*H*-SiC at $E_C - 130\ meV$ and at $E_C - 170\ meV$ [25]. Dalibor *et al* [24] also produced the same results to within experimental error and from DDLTS proved these to be acceptor-like. The levels are further assumed to be a single defect occupying the “k” site and the ‘h” site respectively [23].

Chromium is one other transition metal that has been shown to introduce deep level defects in SiC. Band gap states in 4*H*-SiC of chromium have been reported at $150\ meV$, $180\ meV$ and at $740\ meV$ [25].

5.6 Shallow and deep levels

Defects can be broadly classified into two categories: shallow defect levels and deep centres. Shallow defects refers to impurities whose electronic energies can be calculated by means of the effective mass approximation while deep centres refers to defects whose electronic properties cannot be calculated be means of the effective mass approximation [26]. Though beyond the scope of this thesis, it will be mentioned that electronic properties of deep centres can be calculated by means of the Green function [26].

5.6.1 Shallow defects and nitrogen

Shallow defects can be loosely defined as those impurities that introduce energy levels (in semiconductors) that are very close, a few tens of milli-electron volts to either the conduction band or the valence band compared to the size of the semiconductor bandgap [27]. Usually the energy levels for shallow defects are within 100 meV of the conduction band or the valence band [28]. Those impurities that introduce energy levels in close proximity of the conduction band are shallow donors while shallow acceptors introduce electronic levels very close to the valence band.

In the discussion of shallow level defects in silicon carbide, nitrogen will be used as an example. Substituting a carbon atom in the 4*H*-SiC lattice, a nitrogen atom can either occupy a cubic position or a hexagonal position, otherwise referred to as the "k" sites and "h" sites respectively [11, 29, 30]. Compared to a carbon atom, a nitrogen atom has one too many valence electrons. After satisfying the tetrahedral bonds in the SiC lattice, the nitrogen atom will have one more loosely bound electron. The nitrogen-core and extra electron arrangement is analogous to the hydrogen atom save that the mass of the nitrogen can be regarded as infinite when compared to that of a proton. However, the mass of the electron is renormalized by the periodic potential to a value smaller than that of the free electron (effective mass (m_e^*)) and the coulomb attraction is screened by the semiconductor dielectric constant, ϵ_r [26, 31]. Bohr's theory for the hydrogen atom when applied to the shallow donor would thus be modified to give the electron binding energy, E_D^b as [31]

$$E_D^b = \frac{m_e^*}{m_0}\frac{1}{\epsilon_r^2}\frac{m_0 e^4}{2(4\pi\epsilon_0\hbar)^2} \tag{5.1}$$

where m_0 is a free electron mass, $\hbar = h/2\pi$, h being Planck's constant and ϵ_0 is the permittivity of free space. E_D^b is also known as the ionisation energy and is relative to the energy continuum given by the conduction band [31].

The wave function of the bound electron in real space can be obtained by considering the donor Bohr radius, a_D which is a modification of the Bohr's radius (a_B) in the hydrogen atom [26]. The semiconductor dielectric constant and the effective mass are used in the modification giving [31]

$$a_D = \frac{m_0}{m_e^*}\epsilon_r a_B \qquad 5.2$$

a_D is a measure of the average distance that a donor 1s electron moves in the lattice and thus shows how localized the electron is. Typically a_D is several lattice spacings for shallow donors giving a less localized wave function.

Due to different possible positions for a nitrogen donor in 4H-SiC (hexagonal position or cubic position), two different binding energies exist and are $59\ meV$ and $109\ meV$ for the hexagonal and cubic positions respectively [32]. According to the effective mass approximation, the binding energy for a nitrogen donor would be $6.07\ meV$; hence there is a discrepancy of about $53\ meV$ (considering the hexagonal position). This discrepancy is taken up by the core and is known as the central cell correction. Defects with large central cell corrections have localized wave functions and have a larger probability of interacting with the core [11].

5.6.2 Deep level defects

While impurities mainly introduce shallow levels in semiconductors, other impurities may lead to electronic levels deeper into the bandgap and these are known as deep levels [33, 34]. Some deep levels defects however have electronic levels closer to either the conduction band or the valence band. It is therefore not correct to classify all defects that have electronic levels closer to the bands as shallow level defects.

Defects that have localised wave functions (delocalized in "**k**" space) with binding energies that cannot be calculated by use of the effective mass approximation are deep levels / centres irrespective of their position in the bandgap [26, 31, 35, 36]. As such, deep centres were initially defined simply as those defects which are not shallow defects. The Green's function is widely used for approximation of deep centres electronic structures though there are other methods as well, which can be found from *refs*. [26, 31, 35].

Deep centres can significantly affect the electrical characteristics of semiconductors even when present in small concentrations [33]. In some cases however, deep centres can usefully act as recombination centres increasing switching frequencies of devices as gold would do in silicon [33].

5.7 Description of deep levels

A defect level can be described as an electron trap or a generation-recombination centre depending on the nature of electron and hole interactions that take place between the level and the bands. Figure 5.5 is an illustration of the possible interactions that can take place between the bands and the defect level through the emission and / or capture of electrons and holes. Process (a) shows that a defect can capture an electron from the conduction band with capture rate, c_n after which two possible interactions with the bands are possible. The defect can either emit the electron back to the conduction band, process (b), with emission rate, e_n or it can capture a hole from the valence band, process (c), with capture rate, c_p. These processes leave the defect occupied by a hole, (d) and again with two possible interactions: either emitting a hole to the valence band with rate e_p or capturing an electron, process (d). It should be mentioned at this point that a defect that captures an electron and keeps it for some time before re-emitting it back to the conduction band is known as an electron trap and the converse is true for a hole trap. For electron trapping to occur, the condition $c_n \gg c_p$ must be fulfilled [37]. If however $c_n \approx c_p$, then the defect level is a recombination centre [1]. Following Figure 5.5, a recombination event would be process (a) followed by process (c) while process (c) followed by process (d) would represent a generation event [1].

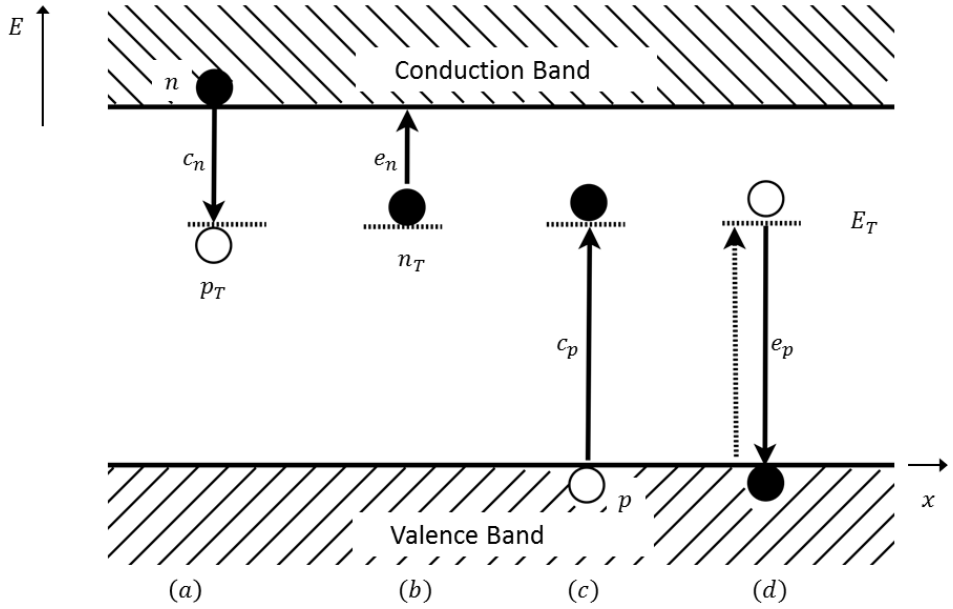

Figure 5.5 Different interactions that can take place between a defect level and the energy bands. Redrawn from ref. [1].

A more detailed mathematical description of the kinetics governing the interactions of defect levels and the bands can be obtained from refs [1, 38]. Here a simplified mathematical

representation of the capture cross section and the emissions rates leading to the defect activation enthalpy, ΔH and the defect capture cross section, σ_n shall be given. The parameters ΔH and σ_n are referred to as the defect 'signatures'.

The electron capture rate can be obtained from the relation [37]

$$c_n = \sigma_n \langle v_{th} \rangle n \tag{5.3}$$

where $\langle v_{th} \rangle$ is the average thermal velocity of electrons and n is the electron concentration in the conduction band. The expression for hole capture rate is analogous to that for electron capture and for a valence band with a hole concentration given by p, it is written as

$$c_p = \sigma_p \langle v_{th} \rangle p \tag{5.4}$$

The physical meaning of the capture cross section can be understood better by freezing the charge carries and allowing the defect level to move with velocity v_{th} sweeping / capturing with a high probability charge carriers that are within the volume $\sigma_n \langle v_{th} \rangle$. The capture cross section vary depending on whether the defect is neutral, repulsive or attractive to the charge carriers [1]. A donor level is considered neutral if it is occupied by an electron and positive if empty while an acceptor is neutral if empty and negative when occupied by an electron. The thermal velocity at a temperature T is given by the relation

$$v_{th} = \sqrt{\frac{3k_B T}{m_e^*}} \tag{5.5}$$

where k_B is the Boltzmann constant and m_e^* is the effective electron mass. n from Equation 5.3 is obtained from [31]

$$n = N_c exp\left(-\frac{E_C - E_T}{k_B T}\right) \tag{5.6}$$

where E_T is the defect energy level, N_C is the effective density of states in the conduction band, E_C and is given by

$$N_c = 2M_C \left(\frac{2\pi m_e^* k_B T}{h^2}\right)^{\frac{3}{2}} \tag{5.7}$$

M_C is the number of equivalent conduction band minima (= 3 for 4*H*–SiC).

The electron emission rate towards the conduction band is a function of temperature, $e_n(T)$ and is given by [37, 39, 40]

$$e_n(T) = \frac{g_0}{g_1}\sigma_n\langle v_{th}\rangle N_C exp\left(-\frac{E_C - E_T}{k_B T}\right) \quad 5.8$$

g_0/g_1 is the degeneracy between empty and filled energy levels. Both $\langle v_{th}\rangle$ and N_C are functions of temperature. Combining Equations 5.5, 5.7 and 5.8, and introducing a constant $X = 2\sqrt{3}(2\pi/h^2)^{\frac{3}{2}} m_e^* k_B^2 M_C$, $e_n(T)$ can be re–written as

$$e_n(T) = \frac{g_0}{g_1}\sigma_n T^2 X exp\left(-\frac{E_C - E_T}{k_B T}\right) \quad 5.9$$

If σ_n is considered to be temperature independent, then Arrhenius plots of $\log(e_n(T)/T^2)$ vs. $1/T$ can be plotted and $E_C - E_T$ is obtained from the gradient of the curve. The intercept of the $1/T$ axis is used to calculate σ_n.

The energy that is required to excite an electron from the trap level to the conduction band is the Gibbs free energy (ΔG) given by the formula [1]

$$\Delta E_n = \Delta G_n = \Delta H_n - T\Delta S_n \quad 5.10$$

where H is the enthalpy, S is the entropy and T is the temperature. The equation for the determination of the emission rate (Equation 5.7) then becomes

$$e_n(T) = \frac{g_0}{g_1}\sigma_n T^2 X exp\left(\frac{\Delta S}{k}\right) exp\left(-\frac{\Delta H_n}{k_B T}\right) \quad 5.11$$

The parameter obtained from thermally activated excitation of carriers from the trap level to the conduction band is therefore the activation enthalpy, while the free energy requires optical measurements to be determined [37].

The capture cross section for many deep level defects is however thermally activated as a result of multiphonon emission via lattice relaxation, and other reasons [41]. If the capture cross section varies with temperature, it usually increases with increasing temperature. In some cases, it may decrease with increasing temperature especially for shallow donors and acceptors at low temperatures [41]. Where the capture cross section has a dependence on temperature, it will be given by the expression [1, 37, 41]

$$\sigma_n = \sigma_\infty \left[-\frac{\Delta E_\sigma}{kT}\right] \quad 5.12$$

where ΔE_σ is the cross section activation energy and $\sigma_\infty$is the capture cross section as $T \to \infty$. Equation 5.11 is then modified to

$$e_n(T) = \frac{g_0}{g_1}\sigma_n T^2 X exp\left(-\frac{\Delta H_n + \Delta E_\sigma}{k_B T}\right) \quad 5.13$$

One technique that can be used to determine the "signatures" of a defect from thermal activation of charge carriers is Deep Level Transient Spectroscopy (DLTS).

5.8 Deep level transient spectroscopy (DLTS)

DLTS is a technique that was developed by Lang in 1974 to investigate deep level defects in semiconductor space charge structures, that is *p-n* junctions or Schottky diode [41]. DLTS has several advantages which include rapid scanning of a wide range of majority and minority traps, simple data interpretation and the technique has high sensitivity [40, 41]. The DLTS technique utilises a capacitance or current transient produced by a thermal emission of charge carriers from traps that are within the space charge region which is constantly reverse biased [39]. In this study, the capacitance based system was used. As such, it is important to recall first from section 3.3.1 how the capacitance of a space charge region varies and the effect of deep traps on the capacitance before the principle of DLTS, rate window concept, is discussed.

5.8.1 Width and capacitance of the depletion region

Following the discussion presented in section 3.3.1, if a diode is under a reverse voltage (V_{ext}), then the depletion width ($w(V_{ext})$) is given, by [31, 42]

$$w(V_{ext}) = \sqrt{\frac{2\varepsilon_0\varepsilon_r(V_{bi} - V_{ext})}{eN_D}} \quad 5.14$$

where ε_0 is the permittivity of a vacuum, ε_r the semiconductor permittivity, e is the elementary charge, N_D is the density of ionised impurities and other defects in the depletion region and $V_{bi}$is built in potential of the junction. The capacitance has an inverse relationship to the depletion width and is obtained from Equation 5.14 as

$$C = \frac{\varepsilon_0 \varepsilon_r A}{w(V_{ext})} = A\sqrt{\frac{e\varepsilon_0 \varepsilon_r N_D}{2(V_{bi} - V_{ext})}} \qquad 5.15$$

where A is the cross–sectional area of the junction. DLTS is based on the monitoring of a change in capacitance which results from a change (due to emission) of the concentration of charges.

5.8.2 The DLTS method

In the DLTS method, the Schottky diode is maintained at a reverse bias voltage and a less negative voltage pulse is periodically applied thereby modifying the band bending. The pulse brings about the capacitance transient that is used to produce a DLTS signal. Figure 5.6 (a) represents the space charge width for a diode that is under a reverse bias. Due to reverse biasing, the space charge width is extended (compared to that of an unbiased diode) and part of the trap will be above the Fermi level, hence empty. If a forward (or a less negative) pulse is applied for a short period of time compared to the pulse period, the band bending is reduced and part of the trap will be below the Fermi level, Figure 5.6 (b). This enables the trap to capture charge carriers consequently resulting in an increased capacitance.

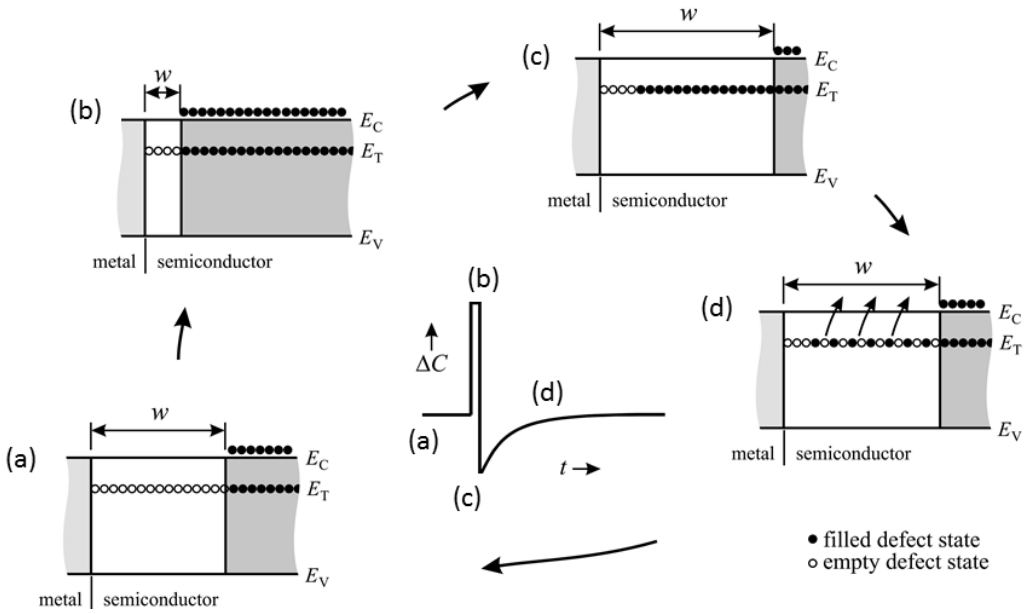

Figure 5.6 Variation of the depletion width and trap concentration in response to voltage biasing conditions for an electron trap in an *n*-type semiconductor. (a) diode reverse biased, (b) during a filling pulse, (c) directly after pulse removal and (d) a time t after pulse removal. The capacitance transient during the cycle is shown at the centre of the figure. Diagram from *ref.* [37].

Electron capture by an initially empty trap is given by [37]

$$N(t) = N_T[1 - exp(-c_n t)] \quad 5.16$$

where N_T is the trap density. Figure 5.6 (c) shows the state of the space charge layer soon after the pulse is removed and returning to the reverse bias. The removal of the voltage pulse causes the depletion width to be larger again and the capacitance falls sharply as a consequence. The part of the trap level that is once again above the Fermi level begins to emit the trapped electrons to the conduction band with emission rate e_n that can be obtained from [37]

$$N(t) = N_T exp(-e_n t) \quad 5.17$$

$N(t)$ is the density of occupied traps at a time *t* after removing the voltage pulse. Due to the high electric field present in the space charge layer, the emitted charges are swiftly swept out of the depletion width eliminating any chances of recapture by the trap [1]. Depending on the emission rates of the trap levels present in the depletion layer, a capacitance transient is observed that exponentially relaxes to the equilibrium capacitance, C_∞. The variation of capacitance, $C(t)$ with time after removing the voltage pulse, considering that $N_T \ll N_D$ is obtained from [37]

$$C(t) = C_0 - \Delta C_0 exp(-e_n t) \quad 5.18$$

where C_0 is the capacitance at quiescent reverse bias voltage and ΔC_0 is the capacitance immediately after removing the voltage pulse. Figure 5.7 is a typical capacitance transient that is observed when a filling pulse is removed. Such a transient would be difficult to obtain for very low trap concentrations [41]. To solve the problem, Lang [41] used the method of repetitively applying filling pulses to enable averaging, and this was done in conjunction with the use of the rate window concept, section 5.8.3, to successfully observe the DLTS spectrum [43].

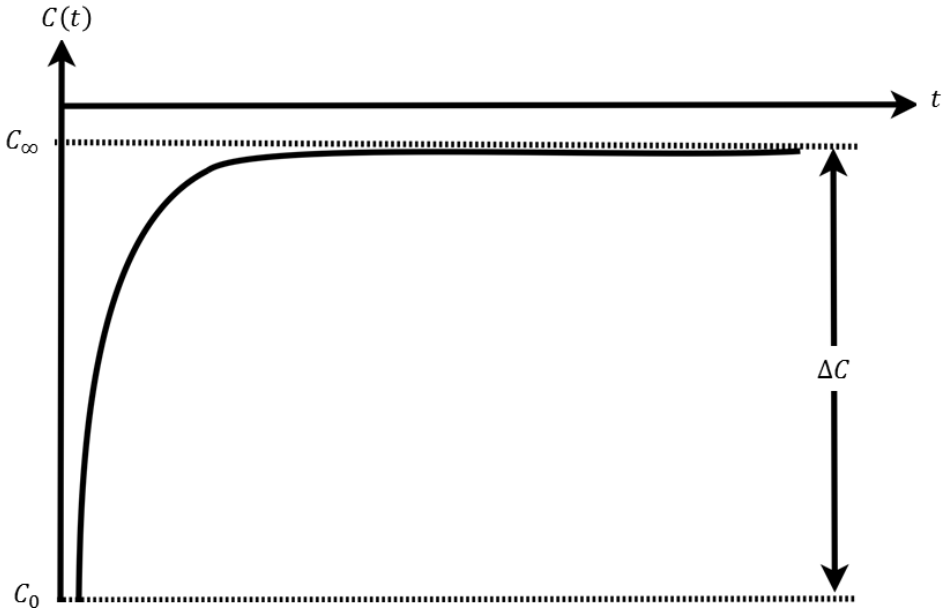

Figure 5.7 Schematic of a capacitance transient. Redrawn from *ref*. [44].

5.8.3 The rate window concept

If e_n can be extracted over a wide range of temperatures, then Equation 5.11 can be used to obtain the defect "signatures". Several techniques are used in the processing of a capacitance transient to obtain the emission rates [41], including the Boxcar avaragers.

In producing a DLTS spectrum by use of the Box car technique, the transient is observed by sampling within a given time window called the "rate window" [43]. The emission process from a particular defect level is very slow for lower temperatures. If the capacitance is monitored over an observation time window, $t_1 - t_2$, then the difference in capacitance at t_1, $C(t_1)$ and at t_2, $C(t_2)$ is a constant. For higher temperatures, the emission process is very fast and again the difference $C(t_1) - C(t_2)$ is a constant. For intermediate temperatures, the emission rate perfectly fits a certain rate window and the maximum capacitance transient is measured. These processes are schematically represented in Figure 5.8 (a) illustrating the change in the emission rates with increasing temperature. Amplitudes of the capacitance transients are determined at times t_1 and t_2, and the difference in capacitance at these two times is plotted, Figure 5.8 (b) to give the DLTS spectrum.

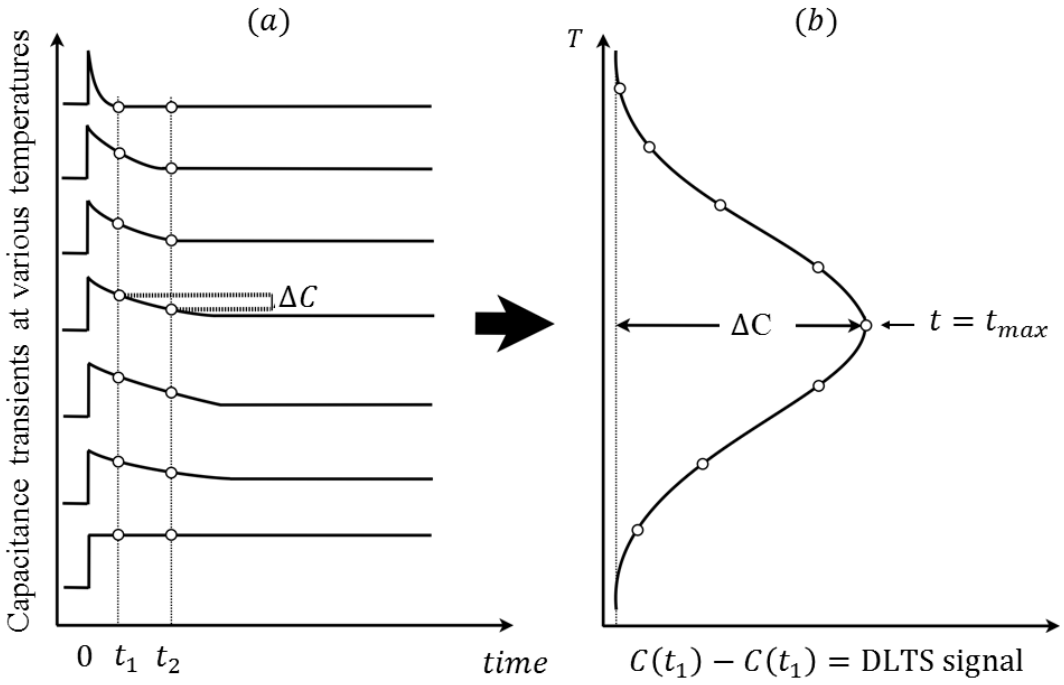

Figure 5.8 (a) Variation of capacitance transients measured at different increasing temperatures and (b) a DLTS spectra produced from plotting ΔC(t) values obtained from the transients. Diagram redrawn from *ref*. [41].

The DLTS spectrum has the units of capacitance, (usually pF) since it is just a difference in capacitance measured at two different times. By scanning over a temperature range, different rate windows would produce different DLTS peaks at different temperatures as shown in Figure 5.9. The graph shown in Figure 5.9 has however been normalized by the capacitance, but this does not change the peak temperature-positions. Also, an increasing $\Delta C/C$ amplitude shows that the voltage pulse width is not long enough for a defect to be completely filled at lower temperatures.

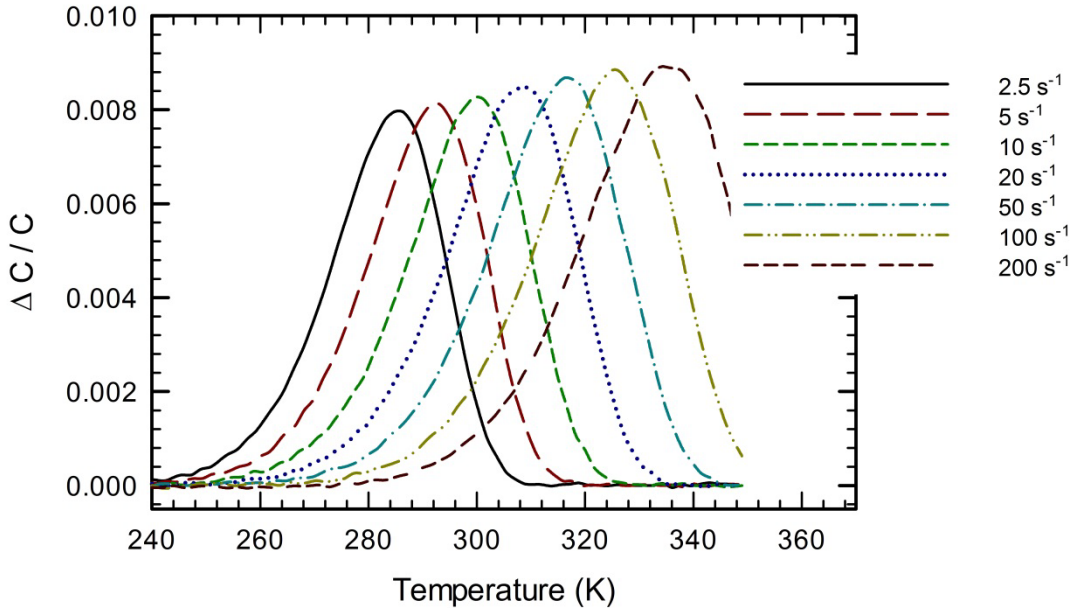

Figure 5.9 Normalized DLTS spectra obtained from a Ni/4*H*-SiC Schottky diode measured from 240K to 350K. the spectra was obtained using a constant reverse bias of -5 V, a voltage pulse of -1 V, and the different rate windows are shown for each spectrum.

5.8.4 Defect depth profiling

The peak height of a defect is directly proportional to the concentration of the defect if the peak is obtained from a saturation pulse width. Taking $\Delta C_0 = C(\infty) - C(0)$ to be the capacitance change just after removal of the voltage pulse, C as the junction capacitance measured under the quiescent reverse bias voltage and N_D being the shallow impurity concentration, then the concentration of deep levels, N_T is given by [41]

$$N_T = \frac{2\Delta C(0)}{C} N_D \qquad 5.19$$

The defect concentration obtained from Equation 5.19 is usually lower than the actual defect concentration. This is because the method assumes that the whole part of the defect in the depletion width is empty under the quiescent reverse bias and thus the whole part takes place in the capture and emission of defects during the periodical pulse application. Figure 5.10 shows that there is a region, λ called the free carrier tail in the depletion width where the trap does not participate in the capture and emission of charge carriers as it is always filled, this leading to an underestimation of the concentration [45]. The region λ is given by [45]

$$\lambda = \sqrt{\frac{2\varepsilon(E_F - E_T)}{eN_D}} \qquad 5.20$$

where ε is the semiconductor dielectric constant, e is the electronic charge, E_F is the Fermi level and $E_T$is the trap level. To take this region into consideration, a method is used where a quiescent reverse is maintained while the voltage filling pulses are varied. Concentrations values, $N_T(x)$ would then obtained at different depths, x in the depletion region. This produces an incremental change in capacitance, $\delta(\Delta C)$ for corresponding incremental voltage pulses, δV_P given by

$$\delta\left(\frac{\Delta C}{C}\right) = \left(\frac{\varepsilon}{ew^2 N_D}\right)\frac{N_T(x)}{N_D(x)}\delta V_P \qquad 5.21$$

where w is the depletion width due to the quiescent reverse voltage and N_D is the ionised shallow impurity concentration. $N_D(x)$ is a function of depth and is obtained from *C-V* depth profiling methods. After taking the λ-correction into account, the concentration can then be obtained from [45]

$$N_T = \frac{2\Delta C(0)N_D(x)}{C}\left[\left(\frac{x-\lambda}{x}\right)^2 - \left(\frac{x_P-\lambda_P}{x}\right)^2\right]^{-1} \qquad 5.22$$

where $x-\lambda$ is the depletion width before applying the voltage filling pulse, $x_P-\lambda_P$ is the depletion width after applying the filling pulse and λ_P is the distance from the depletion region edge to the point where the trap crosses the Fermi level during the pulse width application.

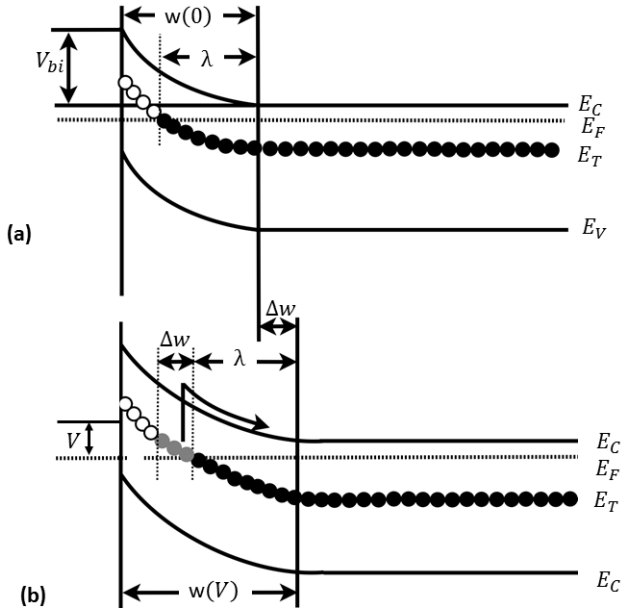

Figure 5.10. Filling (a) and emptying, (b) of a defect level in response to applying and removing a voltage pulse respectively. An increase in the depletion width (Δw) is observed after removing the pulse. Also shown is the fact that the defect is filled to a depth (λ) due to band bending. Diagram redrawn from *refs*. [46, 47].

It is worth mentioning that if the quiescent reverse bias is large enough, the distance λ becomes negligible as compared to the distance x. In such cases Equation 5.22 reduces to Equation 5.19.

4.9 Laplace-DLTS

Although the standard DLTS (which is an analogue signal processing technique) method has high sensitivity, it has a poor time constant resolution for the study of fine structure in emission processes partly due to the way the DLTS spectrum is obtained [48]. Variations in the time constants results in the broadening of the DLTS spectra and makes it difficult to separate different defects that have very close emission rates. The main challenge is therefore to separate the time constants. This can be done through digital signal processing techniques.

A common approach to quantitatively describe the non-exponential nature of the capacitance transients is to assume that they are characterized by a spectrum of emission rates that can be described by an integral [1, 48]

$$f(t) = \int_0^\infty F(s)e^{-st}ds \qquad 5.23$$

where $f(t)$ is the recorded transient and $F(s)$ is the spectral density function. Equation 5.23 gives a mathematical Laplace transform of the true spectra of the emission rates. To obtain

the real spectra of the emission rates, there is need therefore to use an algorithm that performs an inverse Laplace transform of the function $f(t)$. This should give rise to a spectrum of delta-like peaks with multi-, mono-exponential transients and broad spectrum with no fine structure over continuous distribution [1].

In the experimental manifestation of Laplace-DLTS, three different software procedures are used for numerical calculations. The three regularization procedures are the CONTIN [49], FITREG [50] and the FLOG. The three are based on the Tikhonov regularization procedure but differ in the procedure of finding the regularization parameters. The three software packages are used together to increase the level of confidence in the obtained spectra.

References

[1] D.K. Schroder, *Semiconductor Material & Device Characterization*, Third ed., John Wiley and Sons, New Jersey, 2006.

[2] D.A. Neamen, *An Introduction to Semiconductor Devices*, First ed., McGraw-Hill Higher Education, Columbus, 2006.

[3] J. Schneider, K. Maier, Point defects in silicon carbide, Physica B: Condensed Matter, **185** (1993) 199.

[4] T. Yano, T. Sawabe, K. Yoshida, Y. Yamamoto, High-temperature neutron irradiation effects on CVD-diamond, silicon and silicon carbide, Journal of Nuclear Materials, **386-388** (2009) 1018.

[5] G.L. Harris, *Properties of Silicon Carbide*, First ed., IET, United Kingdom,1995.

[6] P.F. Kane, *Characterisation of Semiconductor Materials*, in, McGraw-Hill, New York, 1970.

[7] D. Hull, D.J. Bacon, *Introduction to Dislocations*, Fifth ed., Elsevier Ltd, Great Britain, 2011.

[8] C.A. Wert, R.H. Thomson, *Physics of Solids*, Second ed., McGraw-Hill, New York, 1970.

[9] D. Blavette, E. Cadel, A. Fraczkiewicz, A. Menand, Three-Dimensional Atomic-Scale Imaging of Impurity Segregation to Line Defects, Science **286** (1999) 2317

[10] C.W. Passchier, R.A.J. Trouw, *Microtectonics*, Second ed., Springer, Berlin Heidelberg, 2005.

[11] S.E. Saddow, A.K. Agarwa, *Advances in Silicon Carbide Processing and Applications*, Artech House, MA, 2004.

[12] H. Jacobson, J. P. Bergman, C. Hallin, E. Janzén, T. Tuomi, H. Lendenmann, Properties and origins of different stacking faults that cause degradation in SiC PiN diodes, Journal of Applied Physics, **95** (2004) 1485.

[13] T. Dalibor, H. Trageser, G. Pensl, T. Kimoto, H. Matsunami, D. Nizhner, O. Shigiltchoff, W.J. Choyke, Oxygen in silicon carbide: shallow donors and deep acceptors Materials Science and Engineering: B, **61-62** (1999) 454.

[14] C.M. Zetterling, *Process Technology for Silicon Carbide Devices*, IET, London, 2002.

[15] J. Schneider, K. Maier, Point defects in silicon carbide, Physica B: Condensed Matter, **185** (1993) 199.

[16] M.A. Capano, J.A. Cooper, M.R. Melloch, A. Saxler, W.C. Mitchel, Ionization energies and electron mobilities in phosphorus- and nitrogen-implanted 4H-silicon carbide, Journal of Applied Physics, **87** (2000) 8773.

[17] T. Dalibor, G. Pensl, T. Yamamoto, T. Kimoto, H. M atsunami, S. G. Sridhara, D. G. Nizhner, R. P. Devaty, W.J. Choyke, Oxygen-related defect centers in 4H silicon carbide, Materials Science and Engineering: B, **264-268** (1998) 553.

[18] A. Gali, D. Heringer, P. Deák, Z. Hajnal, T. Frauenheim, R. Devaty, W. Choyke, Isolated oxygen defects in 3C- and 4H-SiC:A theoretical study, Physical Review B, **66** (2002) 125208.

[19] P. Achatz, J. Pernot, C. Marcenat, J. Kacmarcik, G. Ferro, E. Bustarret, Doping-induced metal-insulator transition in aluminum-doped 4H silicon carbide, Applied Physics Letters, **92** (2008) 072103.

[20] S.G. Sridhara, L.L. Clemen, R.P. Devaty, W.J. Choyke, D.J. Larkin, H.S. Kong, T. Troffer, G. Pensl, Photoluminescence and transport studies of boron in 4H SiC, Journal of Applied Physics **83** (1998) 7909.

[21] G. Pensl, H. Morkoç, B. Monemar, E. Janzén, Electrical Characterization of the Gallium Acceptor in 4H- and 6H-SiC, Materials Science Forum **264 - 268** (1998) 557.

[22] M.M. Rahman, C. Y.W. Yang, G.L. Harris, *Amorphous and Crystalline Silicon Carbide II*, First ed., Springer, Verlag, (1989).

[23] T. Dalibor, G. Pensl, Electrical properties of the titanium acceptor in silicon carbide, Physical Review B, **55** (1997) 13618

[24] T. Dalibor, G. Pensl, H. Matsunami, W.J. Choyke, A. Schöner, N. Nordell, Deep Defect Centers in Silicon Carbide Monitored with Deep Level Transient Spectroscopy, Physica Status Solidi, **162** (1997) 199.

[25] N. Achtziger, W. Witthuhn, Band gap states of Ti, V, and Cr in 4H–silicon carbide, Applied Physics Letters, **71** (1997) 110.

[26] P. Yu, Y. Cardona, *Fundamentals of Semiconductors : Physics and Materials*, Third ed., Springer, Berlin, 2009.

[27] H.J. Queisser, E.E. Haller, Defects in Semiconductors: Some Fatal, Some Vital, Science **281** (1998) 945.

[28] S.L. Sheng, *Semiconductor Physical Electronics*, Second ed., Springer, USA, 2007.

[29] T. Kimoto, A. Itoh, H. Matsunami, S. Sridhara, L. L. Clemen, R. P. Devaty, W.J. Choyke, T. Dalibor, C. Peppermuller, G. Pensl, Nitrogen donors and deep levels in high-

quality 4H–SiC epilayers grown by chemical vapor deposition, Applied Physics Letters, **67** (1995) 2833.

[30] A. O. Evwaraye, S. R. Smith, W.C. Mitchel, Shallow and deep levels in *n*-type 4H-SiC, Journal of Applied Physics, **79** (1996) 7726.

[31] M. Grundmann, *The Physics of Semiconductors: An Introduction Including Nanophysics and Applications*, Second ed., Springer, Berlin Heidelberg 2010.

[32] W.J. Choyke, G. Pensl, Physical properties of SiC, Materials Research Bulletin, **22** (1997) 25.

[33] K. Robert, E.R. Willardson, M.S. Weber, *Identification of Defects in Semiconductors*, First ed., Academic Press, USA, 1998.

[34] C.P. Poole, *Encyclopedic Dictionary of Condensed Matter Physics*, First ed., Academic Press, United Kingdom, 2004.

[35] K.A. Kikoin, V.N. Fleurov, *Transition Metal Impurities in Semiconductors: Electronic Structure and Physical Properties*, First ed., World Scientific, USA, 1994.

[36] M. Scheffler, P. Grosse Aachen, Electronic structure of simple deep-level defects in semiconductors, Advances in Solid State Physics, **22** (1982) 010973.

[37] F. D. Auret, Deenapanray, N.K. Prakash, Deep Level Transient Spectroscopy of Defects in High-Energy Light-Particle Irradiated Si, Critical Reviews in Solid State and Materials Sciences, **29** (2004) 1.

[38] W. Shockley, W. Read, Statistics of the Recombinations of Holes and Electrons, Physical Review **87** (1952) 835.

[39] A.A. Garcia, M.A. Barranca, Computerized DLTS system to characterize deep levels in semiconductors, Revista mexicana de física, **48** (2001) 539.

[40] P Blood, J.W. Orton, The electrical characterisation of semiconductors, Reports on Progress in Physics, **41** (1978) 157.

[41] D.V. LANG, Deep-level transient spectroscopy: A new method to characterize traps in semiconductors, Journal of applied physics, **45** (1974) 3014.

[42] S. M. Sze, K.K. Ng, *Physics of Semiconductor Devices*, Third ed., John Wiley & Sons, New Jersey, 2007.

[43] H. Czichos, T. Saito, L. Smith, *Springer Handbook of Metrology and Testing*, Second ed., Springer, Berlin Heidelberg, 2011.

[44] F.C. Beyer, 'Deep Levels In SiC', Ph.D. Thesis, Linkoping University, Linkoping, 2011.

[45] Y. Zohta, M.O. Watanabe, On the determination of the spatial distribution of deep centers in semiconducting thin films from capacitance transient spectroscopy, Journal of Applied Physics **53** (1982) 1809.

[46] W.E. Meyer, 'Digital DLTS studies on radiation induced defects in Si, GaAs and GaN', Ph.D. Thesis, University of Pretoria, Pretoria, 2006.

[47] W. Mtangi, 'Electrical characterization of process, annealing and irradiation induced defects in ZnO', Ph.D. Thesis, University of Pretoria, Pretoria, 2012.

[48] L. Dobaczewski, A. R. Peaker, K.B. Nielsen, Laplace-transform deep-level spectroscopy: The technique and its applications to the study of point defects in semiconductors, Journal of Applied Physics, **96** (2004) 4689.

[49] S.W. Provencher, A constrained regularization method for inverting data represented by linear algebraic or integral equations, Computer Physics Communications, **27** (1982) 217.

[50] J. Weese, A reliable and fast method for the solution of Fredhol integral equations of the first kind based on Tikhonov regularization, Computer Physics Communications, **69** (1992) 99.

CHAPTER 6

Experimental Techniques

6.1 Introduction

The experimental techniques used are explained in this chapter. Firstly, sample cleaning will be described followed by a description of the metal deposition procedure in Sections 6.2 and 6.3 respectively. Sample annealing for both ohmic formation and annealing after irradiation is described in Section 6.4. *I-V* and *C-V* measurement techniques are described in Section 6.5 while the DLTS and Laplace DLTS (L-DLTS) measurements are described in Section 6.6. Lastly, the different particle irradiations done are described in Section 6.7.

6.2 Sample description and cleaning

The 4*H*-SiC used in this study was supplied by Cree Research Inc., and has a doping density of (3.5 – 4.0) × 10^{14} cm^{-3} as determined by *C-V* measurements. The sample has a Si terminating face with 8.05° orientation and an overall thickness of 357 µm of which 19.2 µm is the thickness of the epilayer. The back surface has a doping density of the order of 10^{18} cm^{-3} for ohmic fabrication.

Sample cleaning was done by solution degreasing and etching. Degreasing was achieved through boiling in trichloroethylene (TCE), acetone and methanol for 5-minutes in each solution respectively. This was followed by rinsing in de-ionised water before a 30-second dip in hydrofluoric acid (HF) to remove the native oxide layer. This was followed by rinsing in de-ionised water and a blow-dry using N_2 gas.

6.3 Metal deposition

Both ohmic and Schottky contacts were resistively made. A schematic representation of the resistive deposition system is shown in Figure 6.1. Nickel was used as both the ohmic and Schottky contact metal. Ohmic contacts were fabricated first on the back side of the sample, 1 × 10^{18} cm^{-3} doped side.

In resistive deposition, a crucible containing the metal to be deposited is mounted in a glass jar and connected to a power source. The semiconductor sample is mounted onto a sample

holder inside the glass jar and a vacuum is established. Once the desired vacuum is reached, preferably $\leq 10^{-5}$ mbar, current is passed through the metal crucible. Due to high resistance, the metal starts to melt and evaporate towards the sample as shown in the diagram.it is therefore necessary that only metal with a low melting point are resistively deposited. The sample is first shielded from the evaporating metal. This is important so as to establish a constant and preferably low deposition rate before the sample is subjected to the evaporating metal.

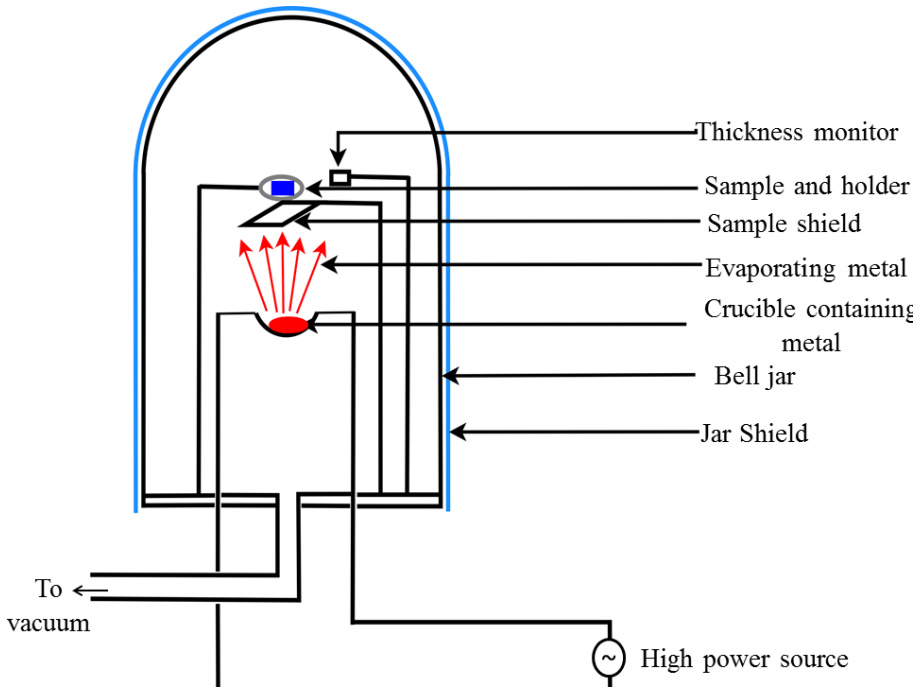

Figure 6.1 Schematic diagram of the resistive evaporation system.

The deposition rate is displayed on an Inficon thickness monitor that is connected to the quartz crystal that is also exposed to the evaporating metal. Once the required deposition rate is reached, the sample shield is removed and the contact deposition on the sample starts.

The whole backside of the sample is exposed to the evaporating metal when making ohmic contacts. During the fabrication of Schottky contacts, the low doped side is mounted on a shadow metal sample holder that only allows circular metal spots – Schottky diodes, to be deposited onto the sample. Schottky diodes with a diameter of 6×10^{-4} m were fabricated in this study. A schematic presentation of typical Schottky diodes is shown in Figure 6.2.

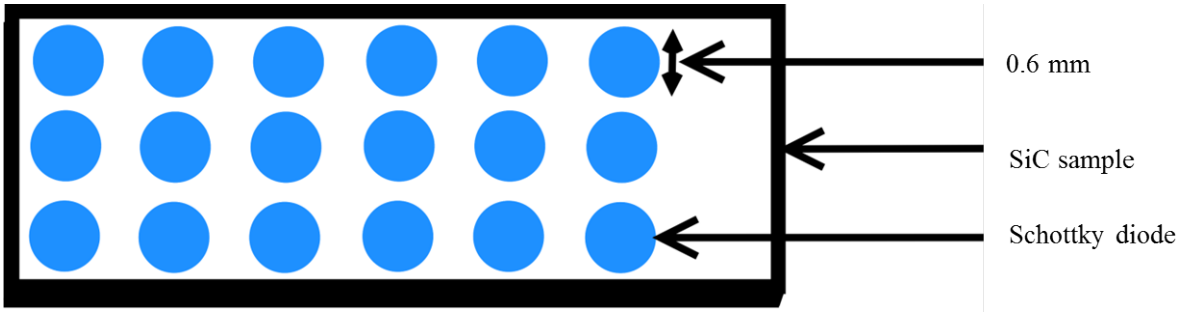

Figure 6.2 Schematic representation of a sample showing fabricated Schottky diodes.

After the fabrication of an ohmic contact, the sample was annealed at 950 °C in argon ambient. The sample was then cleaned following the procedure described in Section 6.2 except that instead of boiling, the samples were rinsed in an ultrasonic bath for three minutes in each solution. The annealing procedure is given in Section 6.4.

6.4 Sample annealing

Sample annealing was done at 950 °C in argon for 15 minutes after ohmic metal deposition. The annealing apparatus is shown by use of a picture in Figure 6.3. A furnace that is capable of annealing at temperatures from 200 °C to 1200 °C is used. The sample is placed on a sample holder which is inside the glass tube and can be moved to different positions of the furnace, to properly position the sample so as to achieve a required temperature. A thermocouple is attached to sample holder for accurate temperature determination.

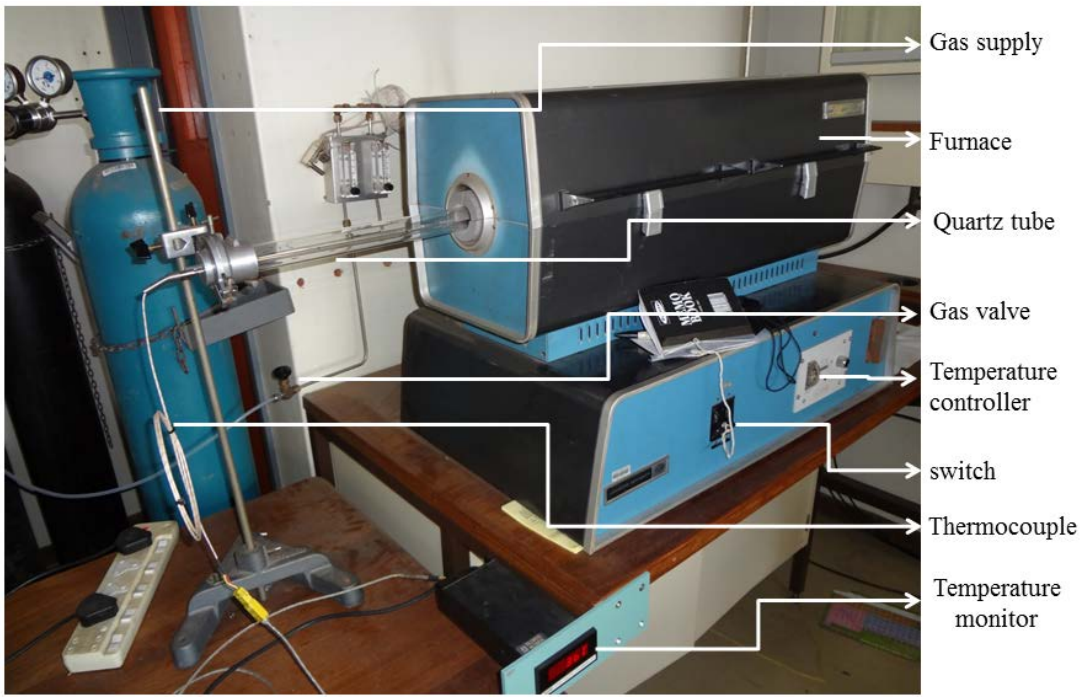

Figure 6.3 Labelled picture of the annealing system.

Also shown in the picture is the gas supply which is linked to the glass tube to ensure the required ambient is obtained during annealing.

Annealing was also performed in steps of 100 °C after irradiation of the diodes. This was done from 100 °C to 700 °C. Although the furnace is designed for annealing from 200 °C, positioning the sample closer to the edge of the furnace enables lower temperature annealing to be achieved.

6.5 *I-V* and *C-V* measurements

I-V measurements were done using a Hewlett Packard pA meter / DC Voltage source 4140B instrument. The instrument allows current measurement from 10^{-15}A with an accuracy of 0.5%. Measurements were carried out in a closed station to ensure there was no illumination from the light. Values of ideality factor, forward and reverse leakage currents, series resistance, saturation current and Schottky barrier height were obtained from *I-V* measurements.

C-V measurements were also carried out in the same closed station using a 4192A LF Impedance Analyzer capable of measuring in the 5 Hz to 13 MHz frequency range. The measurements were performed at a constant frequency of 1 MHz. *C-V* measurements were used to determine the values of the free carrier concentration and Schottky barrier height.

Both *I-V* and *C-V* measurements were recorded by an automated Labview programme.

6.6 DLTS measurements

DLTS and L-DLTS measurements were done by use of the following instrumentation: Laplace card, Boonton 7200 Capacitance Meter, capacitance offset bridge, Lakeshore 332 Temperature Controller, 33120 A Waveform Generator, cryostat, heater, Oscilloscope and a computer. The capacitance meter, temperature controller, pulse generator and the Laplace card were connected to the computer by use of GPIB (IEEE 488-Bus). The connection arrangement of the used instruments is shown in Figure 6.4.

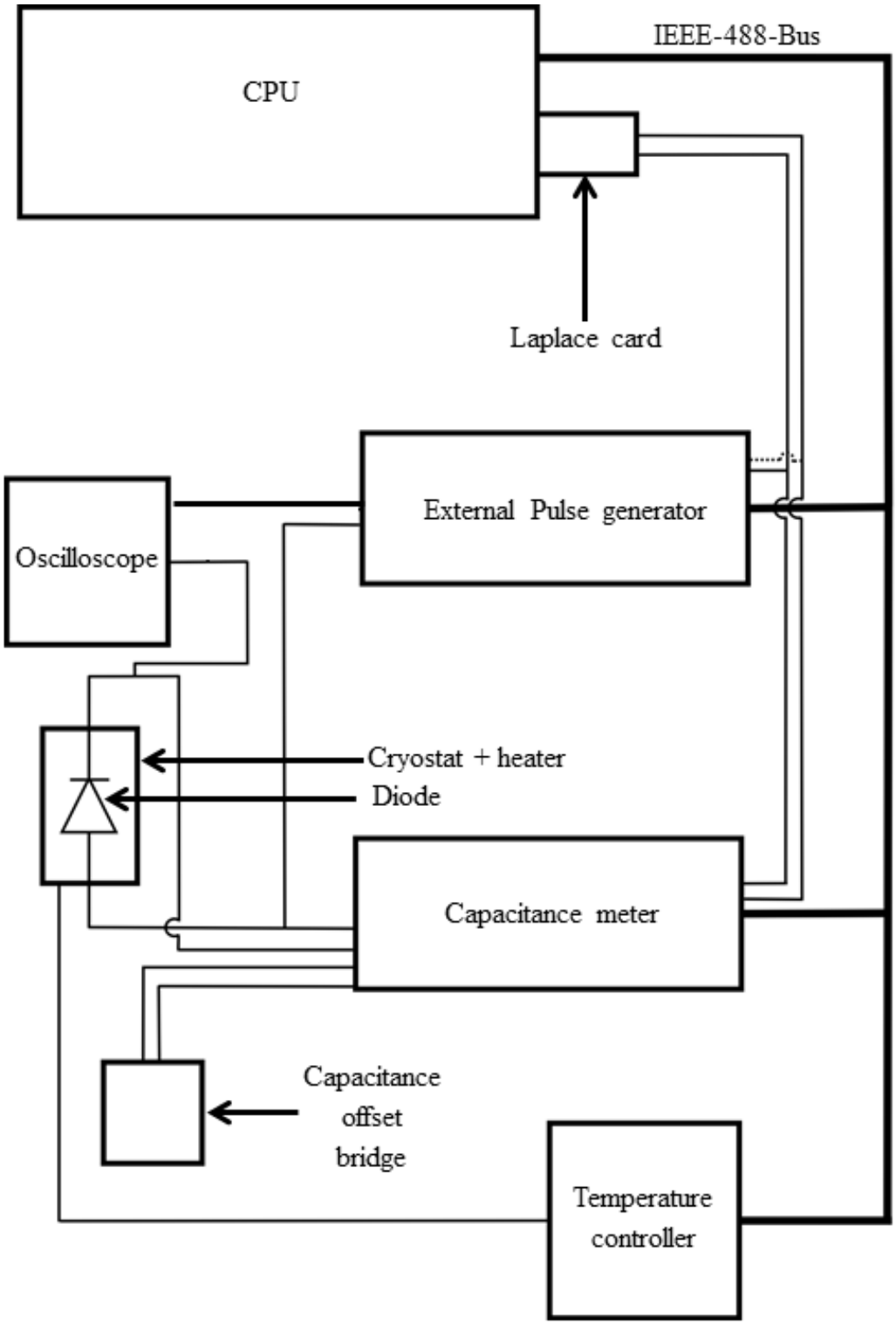

Figure 6.4 Schematic diagram of the L-DLTS and DLTS instrumentation.

The Schottky diode is mounted on top of a heater inside a cryostat kept under very low pressure to avoid condensation. An indium foil is used to separate the sample from the heater. The heater is capable of heating the sample up to temperature of 350 K. A closed cycle

helium cryostat was used for sample cooling so measurements could be done from 30 K to 350 K.

The capacitance meter is connected to the sample by use of two probes, one on the diode and another on the ohmic side (on top of an indium foil). A capacitance offset bridge can be used when necessary to keep the capacitance within a required range. A pulse generator is used to keep the diode under a constant reverse bias and to supply voltage pulses to the diode. The supply voltage pulses have a pulse height and a pulse width that is set as required. The voltage pulse can be viewed on the CRO.

As the temperature is varied and monitored on the temperature controller, voltage pulses are repeatedly supplied to the sample. This leads to successive thermal induced emission of charges by traps if present. A capacitance transient is produced by the DLTS software and displayed on the computer as the temperature is varied. Also displayed on the computer is the DLTS spectrum as the measurements are taken. If a defect is observed from the spectrum, it is necessary to determine accurately the defect signatures by L-DLTS measurements.

L-DLTS measurements are done by stabilising the temperature at a fixed value. The defect emission rate at a particular temperature can then be found. In L-DLTS numerical solutions are obtained by use of three different software procedures [1]. The three different software procedures are based on the same regularization method but differ on the criteria for finding the regularization parameters [1]. The temperature is stabilised at different temperatures and the emission rate at each temperature is obtained leading to the determination of the defect signatures.

6.7 Particle irradiation

After *I-V*, *C-V* and DLTS measurements on the fabricated diodes, the samples were irradiated. Three different forms of particle irradiation were performed: electron, alpha particle and proton irradiation.

6.7.1 Electron and alpha particle irradiation

Electron and alpha particle irradiation were done by use of radioactive foils. In both cases, the radioactive foil was placed on top of the sample in a way that the emitted electrons / alpha particles were directed onto the diodes. A schematic cross section of the irradiation of the diodes is shown in Figure 6.5.

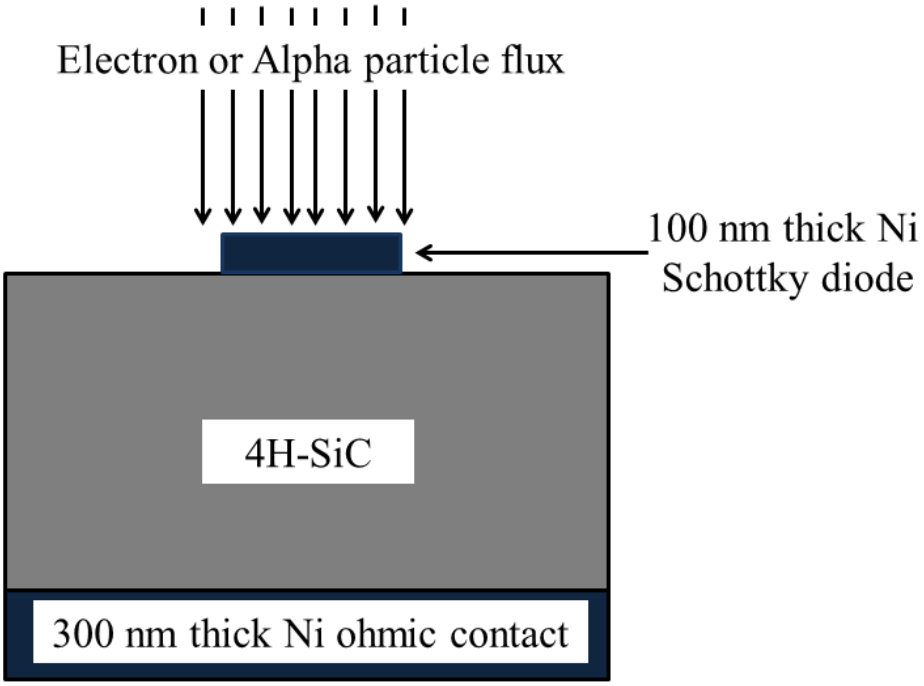

Figure 6.5 Cross sectional schematic diagram of a diode being irradiated by either electrons or alpha particles.

Alpha particle irradiation was done by use of a 5.4 MeV Am-241 radioactive source. The sample used has a fluence rate of 7.1×10^{6} cm-^{2} s^{-1}. Irradiation was done first for 15 minutes, which is equivalent of fluence of 6.4×10^{9} cm^{-2}. *I-V*, *C-V* and DLTS measurements were done after each irradiation. The diodes were then irradiated for another 15 minutes and 30 minutes until a total fluence of 2.6×10^{10} cm^{-2} was achieved, i.e. after 60 minutes of irradiation while the same measurements were repeated after each irradiation.

Electron irradiation was achieved by use of a 546 keV strontium radioactive source with a fluence rate of 6.8×10^{9} cm^{-2} s^{-1}. The samples were irradiated in steps of 2 hours (= 4.9×10^{13} cm^{-2}) until a total cumulative time of 22 hours (= 5.4×10^{14} cm^{-2}) was reached. *I-V*, *C-V* and DLTS measurements were done after each irradiation.

6.7.2 Proton irradiation

Proton irradiation was done using an AN-2000 van der Graaff accelerator. Protons were accelerated onto the diodes with energy of 1.6 MeV. Irradiation was only achieved with fluence of 1.0×10^{12} cm^{-2} before and after *I-V*, *C-V* and DLTS measurements.

References

1. L. Dobaczewski, A. R. Peaker, and K.B. Nielsen, *Laplace-transform deep-level spectroscopy: The technique and its applications to the study of point defects in semiconductors.* Journal of Applied Physics. 96, 2004. **96**(9): p. 4689.

CHAPTER7

Results and discussion

7.1 Introduction

This chapter gives the *I-V*, *C-V* and DLTS results obtained before and after electron, alpha particle and proton irradiations. Isochronal annealing was done on the particle irradiated diodes to study the effect of annealing irradiated samples on diode characteristics as well as to study the annealing dynamics of the irradiation induced defects.

To be able to attribute changes that result from annealing irradiated diodes to irradiation only, unirradiated diodes were annealed and *I-V*, *C-V* and DLTS measurements were done. It was observed that annealing in the temperature range 100 °C ≤ T ≤ 700 °C does not lead to noteworthy changes in the diode ideality factor, SBH or in the reverse leakage current. The free carrier concentration as determined from *C-V* measurements was also observed to remain relatively constant as well in the same temperature range. After annealing the samples at 700 °C, the diodes were observed to become highly resistive.

DLTS measurements were also carried out with annealing up to 600 °C. There were no changes on the DLTS spectra after annealing. Any changes of the *I-V*, *C-V* and DLTS characteristics after particle irradiation and annealing will therefore be as a result of effects of irradiation.

7.2 Electron irradiation results

7.2.1 Introduction

4*H*-SiC samples were irradiated with electrons at different fluence from 4.9×10^{13} cm^{-2} up to 5.4×10^{14} cm^{-2}. *I-V*, *C-V* and DLTS measurements were carried out after each irradiation. The effect of irradiation on the diodes was evaluated from *I-V* measurements results: ideality factor, SBH, reverse leakage current and series resistance. Changes in the free carrier concentration were determined from *C-V* measurements. The SBH was also determined from *C-V* measurements carried out at 1 MHz. DLTS measurements were done in the temperature range $30K \leq T \leq 350K$. Measurements were done before irradiation, after irradiation and after annealing.

7.2.2 Current-voltage results and discussion

The thermionic emission model was assumed in the analysis of *I-V* measurements to obtain the ideality factor, Schottky barrier height, reverse leakage current and the series resistance. The model given by Equation 3.43 gives the current density which is converted into current by multiplying current density by the diode area. Equation 3.43 is then modified to $I = AA^*T^2 exp(-\Phi_{Bn}/k_BT)[exp(\beta V) - 1]$, A being the diode area.

7.2.2.1 The ideality factor

By assuming that thermionic emission was the dominant current transport mechanism across the Schottky barrier, ideality factors were obtained using Equation 3.47 and performing a linear fit on the forward semi-logarithmic *I-V* curves, Figure 7.1. Before irradiation, the ideality factor was obtained as 1.046. This value is close to unity and therefore confirms that thermionic emission is indeed the dominant charge transport mechanism. Electron irradiation was done starting from fluence of 4.9×10^{13} cm^{-2}. As the electron irradiation fluence was increased from 4.9×10^{13} cm^{-2} to 5.4×10^{14} cm^{-2}, there was no marked increase in the ideality factor. Usually if there are electrically active defects that are introduced by irradiation, there could be generation recombination effects and the ideality factor would increase. A closer look at the *I-V* curves shows that there is an increase in the current at lower voltages after irradiation. This possibly results from a contribution of generation recombination current transport mechanism. The possibility of defects being introduced cannot be ruled out on the basis of a non-increasing ideality factor. Introduced defects if any may not have a noticeable

effect on current transport. The obtained ideality factor values with increasing irradiation fluence are shown in Table 7.1

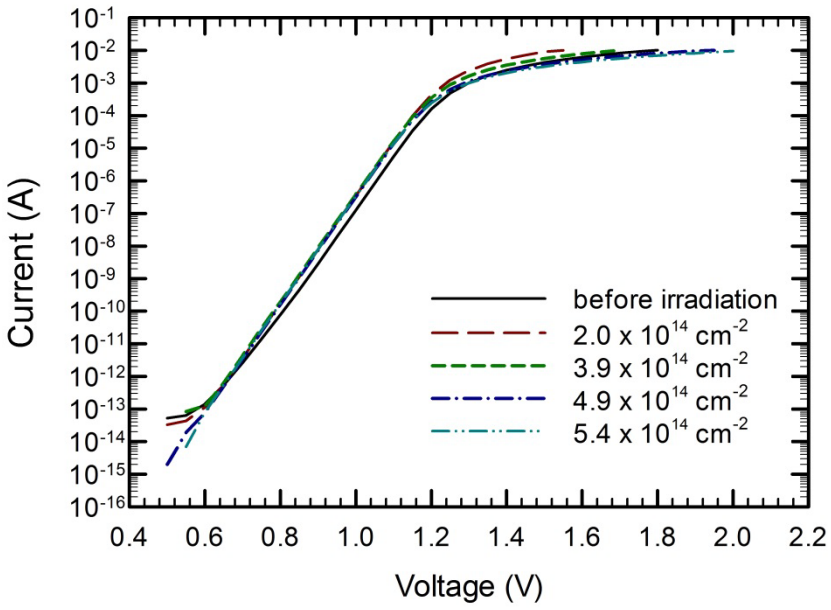

Figure 7.1 Semi-logarithmic I-V curves as a function of electron irradiation fluence up to a fluence of 5.4×10^{14} cm^{-2}. All steps were measured although only certain measurements are shown in this plot.

7.2.2.2 Schottky barrier height (SBH)

According to the Schottky-Mott theory, Equation 3.1, an ideal Schottky barrier height, Φ_{Bn} is given by $e\Phi_{Bn} = e(\Phi_m - \chi_{sc})$, where Φ_m is the metal work function and χ_{sc} is the semiconductor electron affinity. The experimental work function of nickel is 5.35 eV [1] while the electron affinity of 4*H*-SiC is 3.1 eV [2]. The ideal Schottky barrier height for Ni/4*H*-SiC is therefore 2.25 eV. The value obtained from *I-V* measurements before irradiation is 1.620 eV which is lower than that predicted by the classical Schottky-Mott theory. It therefore follows that there are other factors, mostly likely the presence of interface states that lead to a non-ideal SBH. To see if a metal/semiconductor contact can be described by the Schottky-Mott / Bardeen theory, that is the Fermi-level pinning described in Section 3.2.2, several metals can be used to obtain the interface index ($S = \partial\Phi_{Bn}/\partial\Phi_m$) [2-4]. Rocaforte *et al* [2] determined the interface index for 4*H*-SiC to be 0.41, a value which shows the presence of partial Fermi-level pinning. $S = 1$ shows perfect Schottky-Mott behaviour while $S = 0$ means there is complete Fermi level pinning [2].

Another reason why the ideal Schottky barrier height is not realised is the inhomogeneity of the metal-semiconductor interface [5, 6]. Because of the inhomogeneity, the SBH values obtained have a Gaussian distribution about a mean value.

The SBH remained relatively the same with irradiation without showing a general pattern, increase or decrease, in response to the increasing irradiation fluence. The obtained values are given in Table 7.1.

7.2.2.3 Reverse leakage current

The reverse leakage current density can be obtained from equation 3.43 given in section 3.5.1 by replacing the voltage, V with a negative voltage value V_R [7]. Equation 3.43 would then reduce to the expression for saturation current, $J_s = A^*T^2 \exp(-\Phi_{Bn}/k_BT)$. This equation shows that the reverse leakage current is a strong function of temperature and the SBH.

The reverse current was measured from 0 V to -50 V. Very low values of reverse leakage current were obtained with that before irradiation being 1.2×10^{-14} A at -5 V. This value increased to 1.0×10^{-10} A at -50 V. The low leakage current values obtained are a result of the high SiC SBH. The leakage current only shows an increase with irradiation at low voltages of up to -10 V. The increase in the reverse leakage current with increasing irradiation fluence is possibly due to the creation of generation-recombination centres as a result of atomic displacements.

At higher voltages the reverse current does not vary with fluence up to a fluence of 5.4×10^{14} cm^{-2}. Semi-logarithmic curves of reverse leakage current at different irradiation fluences are presented in Figure 7.2.

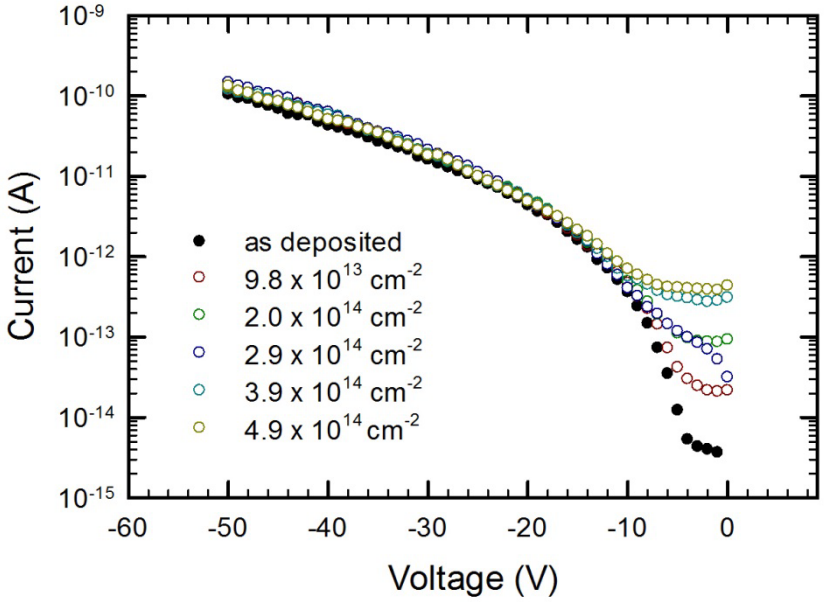

Figure 7.2 Semi-Logarithmic curves of the reverse leakage current measured up to -50V as function of electron irradiation up to a fluence of 4.9 × 10^{14} cm^{-2}. All steps were measured although only certain measurements are shown in this plot.

The leakage current values obtained increase with increasing voltages. This is due to the Schottky barrier lowering discussed in Section 3.2.3. As the reverse voltage increases, the electric field increases leading to Schottky barrier lowering since the barrier lowering directly depends on the electric field, equation 3.18. The dependence of the electric field, Ɛ on the voltage is given by the relation [8] $\mathcal{E} = \sqrt{[2eN_D/\varepsilon_r\varepsilon_0](V_R + V_{bi})}$.

7.2.2.4 Series resistance

In Schottky diodes, the series resistance is obtained by modifying Equation 3.43 to $J_{S\to M} = A^*T^2 exp(-\Phi_{Bn}/k_BT)[exp(e(V - IR_s)/nk_BT) - 1]$. The series resistance measured in Schottky diodes is a sum of two contributions, R_{epi} and R_{sub} where R_{epi} is a component of the epilayer while R_{sub} is a component of the substrate [9, 10]. There substrate resistance is usually negligible and the epilayer resistance is obtained from $R_{epi} = Th_{epi}/[eN_D\mu(N_D)A]$, where Th_{epi} is the epitaxial layer thickness, N_D is the epilayer active dopant and μ is the electron mobility [9].

Before irradiation the series resistance, R_s was obtained as 47 Ω, which is a low value showing desirable Schottky diodes. After irradiation at lower fluences of 9.8 × 10^{13} cm^{-2}, the resistance decreased to 20 Ω before increasing to 63 Ω at fluence 4.9 × 10^{14} cm^{-2}. The cause

for the initial decrease in resistance still has to be investigated further. Change in resistance with irradiation fluence is shown in Figure 7.3.

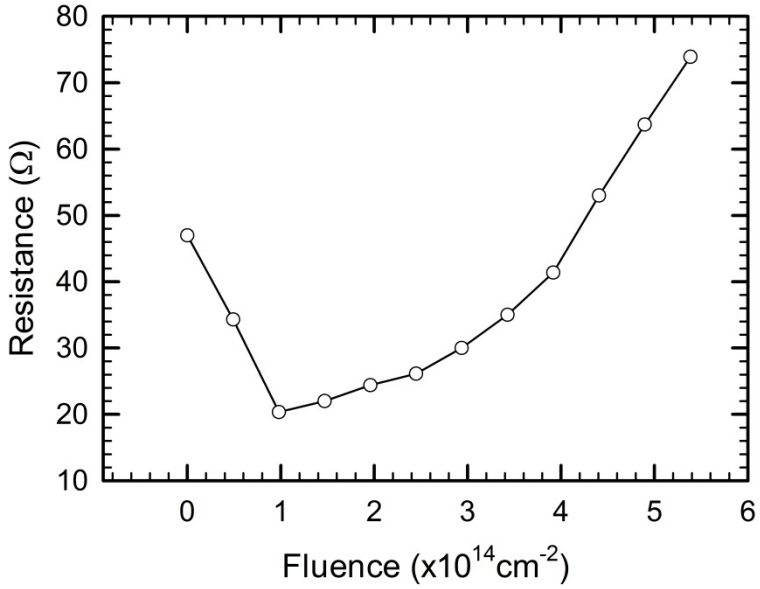

Figure 7.3 The variation of series resistance with electron irradiation to fluence of 5.4×10^{14} cm^{-2}.

The increase in resistance with irradiation is due to a decrease in the active carrier concentration that results from irradiation. The decrease in resistance that is observed at lower irradiation fluences is in agreement with an initial increase in the free carrier concentration that is observed for the same fluences, Figure 7.5.

7.2.2.5 I-V results conclusion

The close to unity ideality factor values obtained show that the thermionic emission process is the dominant current transport mechanism in the investigated Schottky diodes. These close to unity values also means the fabricated Schottky diodes are of high quality. Lower leakage current values were also obtained, and these are a function of large SBH that are a characteristic of SiC. Irradiation did not significantly change these parameters, a sign that the degradation due to electron bombardment was not severe. Only a small increase was observed in series resistance after irradiation, changing from 47 Ω before irradiation to 63 Ω after irradiation. The ideality factors, SBHs, reverse leakage current values and resistance values obtained before and after electron irradiation are summarised in Table 7.1.

Table 7.1 *I-V* parameters obtained from room temperature measurements for as deposited diodes and with irradiation to a fluence of 5.4×10^{14} cm^{-2}. Not all values are presented in this table.

Fluence (cm^{-2})	Ideality factor ±0.02	SBH (eV) ±0.03	Reverse Current (A) (at -5V)	Resistance (Ω)
0	1.05	1.62	1.2×10^{-14}	47
4.9×10^{13}	1.05	1.61	2.1×10^{-14}	33
9.8×10^{13}	1.04	1.59	4.2×10^{-14}	25
2.0×10^{14}	1.05	1.61	1.1×10^{-13}	34
2.9×10^{14}	1.04	1.60	1.1×10^{-13}	36
3.9×10^{14}	1.04	1.60	3.2×10^{-13}	41
4.9×10^{14}	1.04	1.60	4.1×10^{-13}	63
5.4×10^{14}	1.04	1.60	5.2×10^{-13}	74

7.2.3 Capacitance-voltage (C-V) results and discussion

The effects of electron irradiation on the free carrier concentration were evaluated using *C-V* measurements. The free carrier concentration, N_D and the SBH, Φ_{Bn} were determined from the slope and the intercept of the graph of $1/C^2$ against V respectively. The free carrier removal rate was obtained from the slope of $\Delta(N_D - N_A)/\emptyset$, $\emptyset$ being the fluence and ΔN_D being the change in the free carrier concentration. SRIM simulations were also carried out in order to correlate the amount of vacancies created by irradiation with the compensation observed from *C-V* measurements.

7.2.3.1 The SBH

Following Equation 3.28, the SBH can be obtained from the voltage intercept of the graph of $1/C^2$ against external voltage, V_{ext} taking into account the built in voltage, V_{bi} and $\beta^{-1} = (k_B T)/e$. The $1/C^2$ curves obtained before and after irradiations are shown in Figure 7.4. Before irradiation the SBH was obtained as 2.13 eV. This value is larger than the one obtained from *I-V* measurements and is much closer to the Schottky-Mott predicted value of 2.25 eV. This is because the effect of an inhomogeneous interface does not affect the SBH produced from *C-V* measurements.

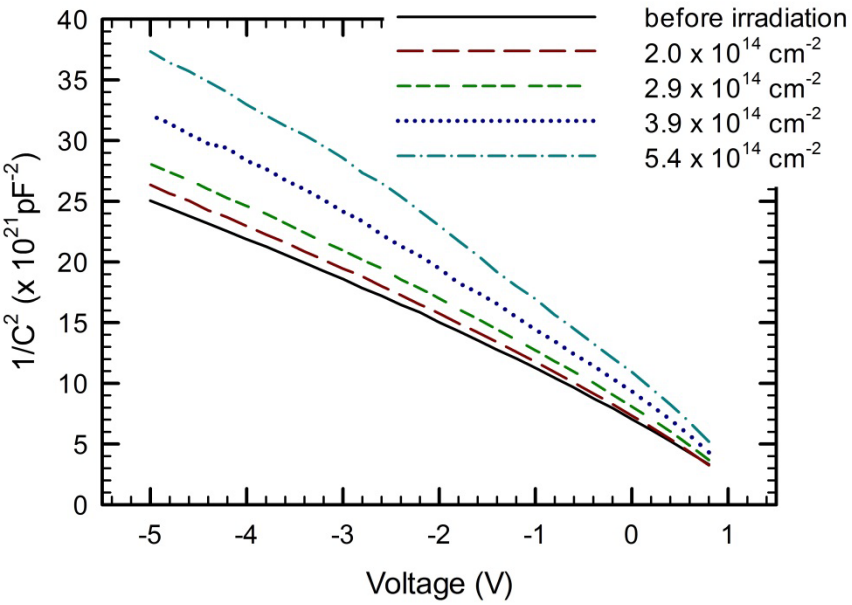

Figure 7.4 Curves of $1/C^2$ against Voltage obtained after different electron irradiation fluences.

After irradiation the Schottky barrier height only had a slight increase reaching 2.19 eV after irradiation with a fluence of 2.9 $\times 10^{14}$ cm^{-2}. It can also be seen from Figure 7.4 that there is a small but progressive upward shift of the curves with irradiation leading to higher voltage intercepts. The SBH however then decreases to 2.14 eV after irradiation at fluence of up to 4.9 $\times 10^{14}$ cm^{-2}. Overall, there is a slight increase in the SBH showing only limited degradation of the Schottky diodes due to electron irradiation.

7.2.3.2 Free carrier concentration

The free carrier concentration is obtained from the slope of the $1/C^2$ curves shown in Figure 7.4. Before irradiation this value was obtained as 4.6 $\times 10^{14}$ cm^{-3}. After irradiation at fluence of 9.8 $\times 10^{13}$ cm^{-2}, the free carrier concentration increased to ~ 4.9 $\times 10^{14}$ cm^{-3} before a gradual decrease to ~ 3.0 $\times 10^{14}$ cm^{-3} at a fluence of 5.4 $\times 10^{14}$ cm^{-2}. A graph of the change in free carrier concentrations as a function of the irradiation fluence is shown in Figure 7.5.

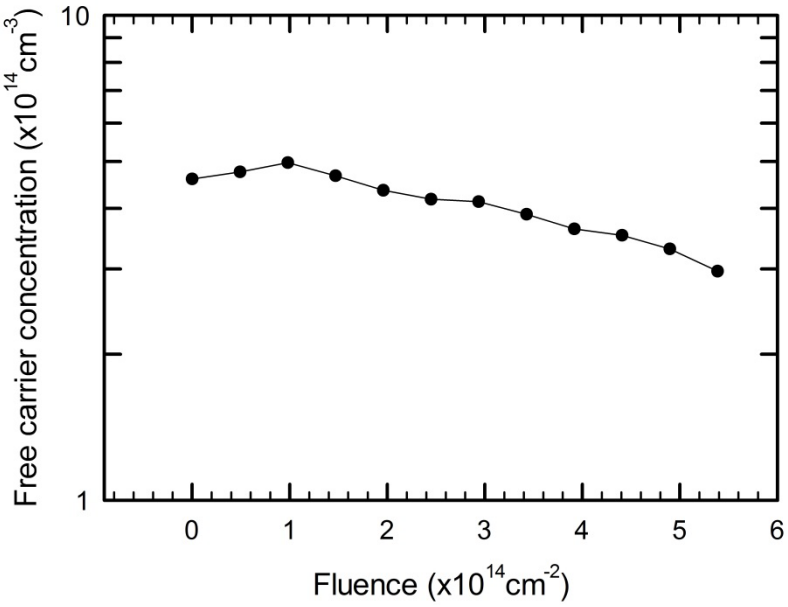

Figure 7.5 The change in the free carrier concentration as a function of the electron irradiation fluence up to a fluence of 5.4 × 10^{14} cm^{-2}. The N_D values were obtained at a depth of 3.5 μm below the M-S interface.

The reduction in the free carrier concentration with irradiation is an indicator that vacancies were created by irradiation and these have an effect of compensating the free carriers. SRIM simulations were carried out and predict a vacancy concentration of ~2 × 10^{11} cm^{-1} at 3.5 μm.

7.2.3.3 Free carrier removal

Carrier removal by irradiation can be as a result of the introduction of compensating acceptors or due to deactivation of donor impurities by interacting with mobile intrinsic defects such as vacancies and interstitials [11]. The free carrier removal rate, η is obtained from the relation $\eta = \Delta(N_D - N_A)/\emptyset$, where ∅ is the fluence and $N_D - N_A$ is the free carrier concentration [12]. It follows that the slope of the graph of $\Delta(N_D - N_A)$ against∅, Figure 7.6 gives the free carrier removal rate. The free carrier rate was obtained as 0.37 cm^{-1} for 546 keV electrons.

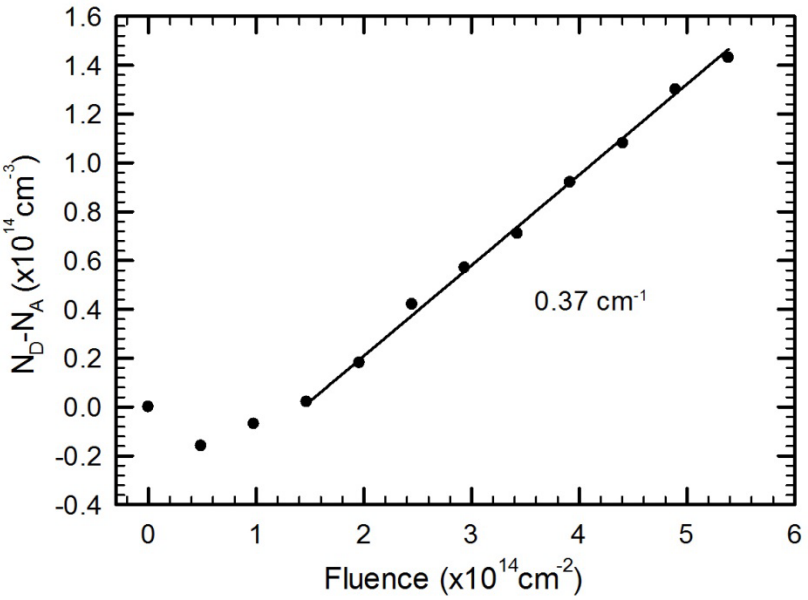

Figure 7.6 Free carrier removal rate graph obtained from the linear region of ΔN_D versus fluence.

The free carrier removal rate obtained here is a very low value which shows that SiC is indeed a radiation hard material. Previous studies [13] produced equally low removal rates of $\leq 0.1\ cm^{-1}$ from electron irradiation of 1 MeV energy.

7.2.3.4 C-V results conclusions

The *C-V* results obtained show very little changes in the diode characteristics. The Schottky barrier height remained relatively unchanged after electron irradiation with fluences of up to 5.4×10^{14} cm^{-2}. The free carrier concentration decreased from 4.6×10^{14} cm^{-3} before irradiation to 3.0×10^{14} cm^{-3} leading to a low carrier removal rate of 0.37 cm^{-1}.

7.2.4 DLTS results and discussion

DLTS was carried out on the as-prepared samples in the 30 – 350 K temperature range. A reverse bias of 5 Volts was maintained while filling voltage pulses of $-1\ V$ were applied with a pulse width of $1\ ms$. Capacitance-temperature measurements were also carried out in the same temperature range as DLTS measurements to enable normalization of the obtained spectra. The obtained DLTS spectra for the as-prepared samples, Figure 7.7 show the presence of four defect levels labelled $E_{0.10}$, $E_{0.12}$, $E_{0.18}$ and $E_{0.69}$ defect levels. These have activation energies 0.10 eV, 0.12 eV, 0.18 eV and 0.69 eV, calculated from the Arrhenius

plots of Figure 10. Arrhenius plots are obtained according to the explanation given in section 5.7.

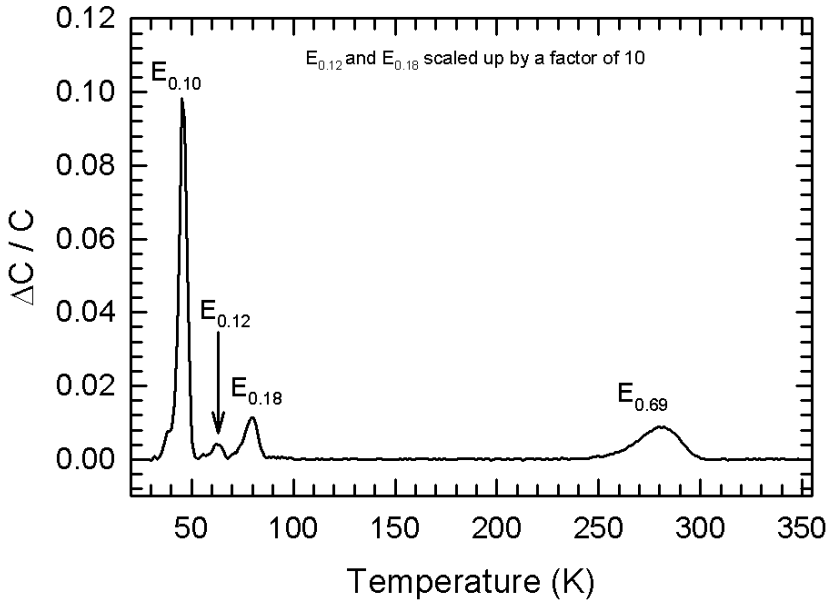

Figure 7.7 DLTS spectra for the as deposited sample. Spectra taken at -5V, and rate window of 2.5 s^{-1}.

The $E_{0.10}$ defect has been attributed to nitrogen dopants occupying cubic sites [14, 15]. When occupying a hexagonal site in 4*H*-SiC, this defect level is expected to have an activation energy of approximately 0.050 eV [16, 17]. This level is the nitrogen donor responsible for the *n*-type doping in SiC.

The $E_{0.12}$ and $E_{0.18}$ levels are related to a transition metal titanium [18, 19]. To within experimental error, Achtziger *et al* [18] observe and attribute the $E_{0.12}$ defect level to titanium impurity. A defect level with energy 0.18 eV has also been reported and associated with a titanium impurity [19]. The $E_{0.12}$ and $E_{0.18}$ levels could both be a single defect occupying different geometrical positions in the material, where it is seen as $E_{0.12}$ when occupying a hexagonal site while it is seen as $E_{0.18}$ when occupying a cubic lattice site [18].

The $E_{0.69}$ defect level is largely agreed to be of intrinsic nature although there is no agreement on the exact structure of the defect. The possible structure of the defect has been attributed to a carbon vacancy, V_C [20], a silicon vacancy, V_{Si} [21], a nitrogen impurity next to a carbon interstitial, I_C+N [22], a silicon antisite-silicon vacancy complex, C_{Si}-V_{Si} [23] or a silicon carbon antisite pair, C_{Si}-Si_C [23]. Several studies with low energy electron irradiation however eliminate the role of silicon for a possible explanation of the structure of this defect.

Hemmingsson *et al* [24] did measurements on electron irradiated SiC and show the defect concentration to increase with irradiation. This rules out the possible silicon participation since the displacement energy for silicon is much higher than that supplied by low energy electrons. Carbon vacancies and / or interstitials are therefore possibly linked to the structure of this defect since carbon is lighter and hence can be displaced by low energy electrons as compared to silicon. Nitrogen and phosphorous doped SiC has been studied by Bergman *et al* [25] to establish the possible inclusion of nitrogen in the structure of the defect. It was realized that the concentration of the defect actually increases after electron irradiation in samples that are phosphorous doped when compared to those that are nitrogen doped. This means that nitrogen cannot be related to the structure of the defect. While the exact structure of the defect is uncertain, recent experiments have however eliminated silicon participation leaving carbon vacancies, interstitials and carbon related complexes as the most probable candidates for the defect.

7.2.4.1 Irradiation results

The samples were then irradiated with electrons from a fluence of $4.9 \times 10^{13} cm^{-2}$, equivalent of 2hours irradiation at a dose rate of $6.8 \times 10^{9} cm^{-2} s^{-1}$, to a fluence of $5.4 \times 10^{14} cm^{-2}$(= 22 hours irradiation), in steps of two hours. DLTS measurements were carried out after each irradiation and the normalized spectra are presented in Figure 7.8. For a clearer presentation, only the spectra obtained after irradiation at $9.8 \times 10^{13} cm^{-2}$, $2.0 \times 10^{14} cm^{-2}$, $2.9 \times 10^{14} cm^{-2}$, $3.9 \times 10^{14} cm^{-2}$, $4.9 \times 10^{14} cm^{-2}$ and $5.4 \times 10^{14} cm^{-2}$ are presented together with the as-prepared spectra for comparison.

It is seen from the spectra obtained with irradiation that new defects are introduced by electron irradiation. The introduced defects are labelled $E_{0.42}$, $E_{0.62}$ and $E_{0.76}$, as usual the subscripts representing the activation energies of the respective defect levels. Irradiations done at cumulative fluences enabled a closer analysis of the evolution of the defects.

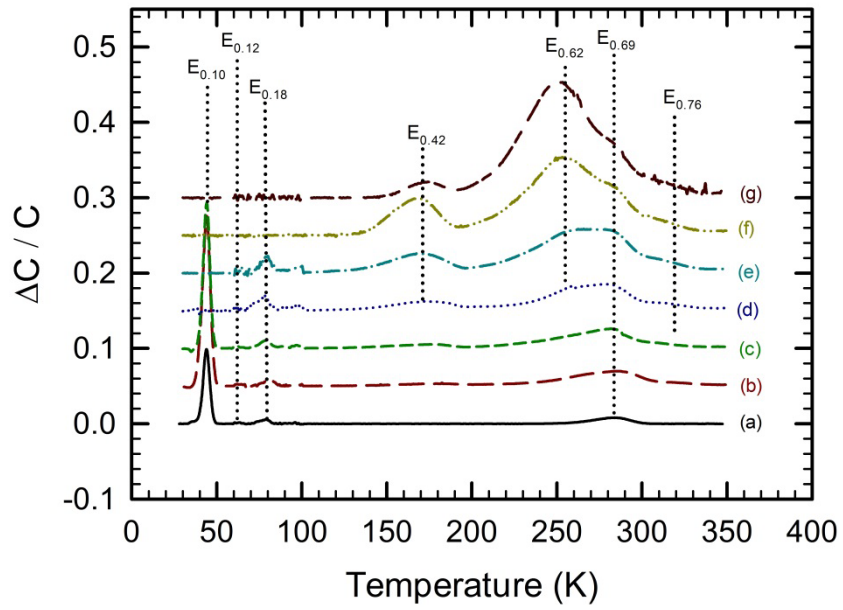

Figure 7.8 Spectra produced at different electron fluence irradiations. (a) as prepared, (b) 9.8×10^{13} cm^{-2} , (c) 2.0×10^{14} cm^{-2} (d) 2.9×10^{14} cm^{-2}, (e) 3.9×10^{14} cm^{-2}, (f) 4.9×10^{14} cm^{-2} (g) 5.4×10^{14} cm^{-2}.

The signatures of defect level $E_{0.62}$ were determined using Laplace-DLTS and the obtained spectra are shown in Figure 7.9. Arrhenius plots plotted using equation 5.13, Figure 7.10, were used to calculate the activation energies and apparent capture cross sections of the defects both before and after electron irradiation.

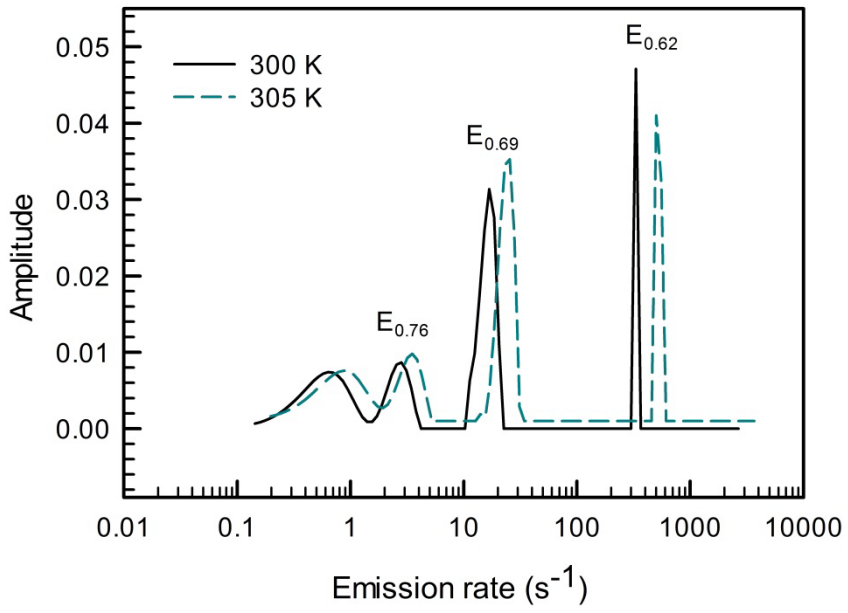

Figure 7.9 Laplace-DLTS spectra showing emission rates of levels $E_{0.62}$, $E_{0.69}$ and $E_{0.76}$.

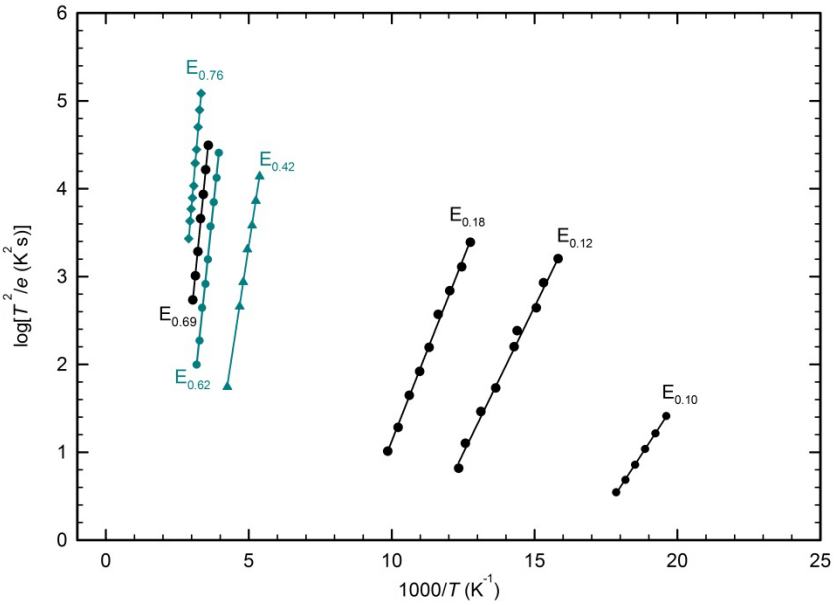

Figure 7.10 Arrhenius plots of the defects obtained before and after electron irradiation.

7.2.4.1.1 $E_{0.42}$

A similar defect level has been reported [26] after electron irradiation and room temperature annealing for nine months. The defect was reported to show acceptor-like behaviour. The decrease in the free carrier concentration shown in Figure 7.5 indicates an increase in compensation with increasing fluence suggesting the acceptor-like behaviour of introduced deep levels as well. Nava *et al* [27] attributes a similar defect level to be a silicon vacancy. In contrast, Storasta et al suggests a similar defect level with an activation energy of 0.41 eV could be more related to a carbon vacancy, split interstitial or antisites after low energy electron irradiation [21]. The $E_{0.42}$ defect is observed after irradiation to fluence of only $1.5 \times 10^{14} cm^{-2}$ with a concentration of $3.8 \times 10^{12} cm^{-2}$. After the fluence was increased to $4.9 \times 10^{14} cm^{-2}$, the concentration of this defect level was observed to increase to $6.2 \times 10^{13} cm^{-2}$. An exponential increase in the concentration of the $E_{0.42}$ defect level is shown in Figure 7.11. This is an indication that defect $E_{0.42}$ is not as simple defect.

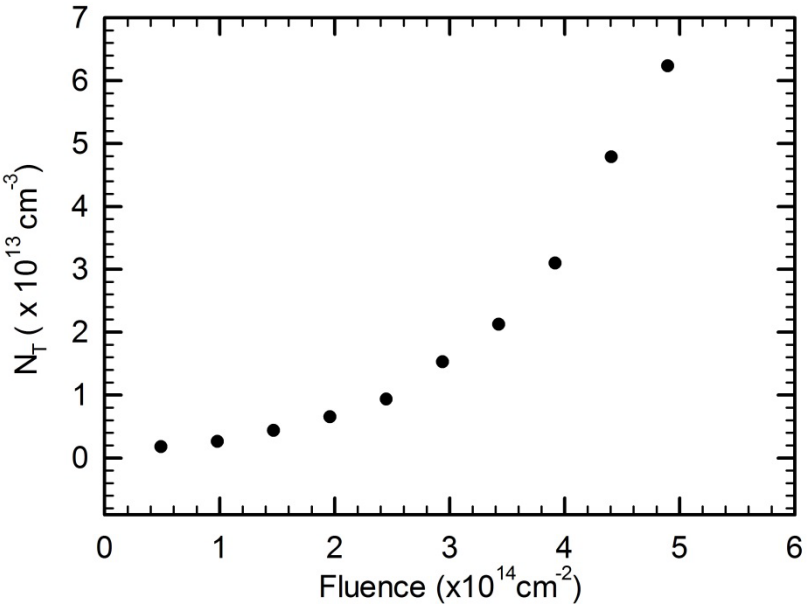

Figure 7.11 Increase in concentration of the $E_{0.42}$ defect with increasing electron fluence.

7.2.4.1.2 $E_{0.62}$ and $E_{0.69}$

The $E_{0.62}$ defect is clearly observed after a fluence of up to $2.9 \times 10^{14} cm^{-2}$. This defect level has a high capture cross section of $2 \times 10^{-14} cm^2$, as compared to that of the $E_{0.69}$ level, $8 \times 10^{-15} cm^2$. A closer look show a loss in symmetry of the DLTS peak due to a superimposition of the $E_{0.62}$ level but in very low concentrations.

$E_{0.69}$ increased in concentration with increasing electron fluence. Commonly known as the Z_1/Z_2 defect, the $E_{0.69}$ defect is of intrinsic nature [24, 28, 29]. It is mostly linked to a carbon vacancy, carbon interstials and / or complexes of carbon vacancies and interstitials [24, 26, 29]. Carbon requires less displacement energy compared to silicon. The increase in the concentration of this defect is therefore easier to comprehend as irradiation is expected to create carbon vacancies and interstitials.

7.2.4.1.3 $E_{0.76}$

In addition to $E_{0.42}$ and $E_{0.62}$, another deep level is introduced by electron irradiation at $E_c - 0.76\,eV$, with a capture cross section of 1.0 $\times 10^{-14}$ cm^2. This defect appears as a shoulder of $E_{0.69}$ on the high temperature side. The structure of this defect has not been reported in literature despite its presence having been reported after electron and proton irradiation [26, 30]. However, since this defect is introduced by irradiation, it could be related

to carbon vacancies, silicon vacancies, carbon or silicon interstitials, carbon or silicon antisites or complexes of the above mentioned possibilities.

7.2.4.1.4 $E_{0.10}$, $E_{0.12}$ and $E_{0.18}$

There was no noticeable effect of electron irradiation on defect levels $E_{0.12}$ and $E_{0.18}$. Level $E_{0.10}$ on the other hand was completely suppressed by electron irradiation after a fluence of $2.9 \times 10^{14} cm^{-2}$. This level is believed to be nitrogen related defect occupying a cubic site thus the suppression can be directly linked to the reduction in free carrier concentration that is observed from *C-V* measurements. The defect activation energies, apparent capture cross sections and the defect concentrations are presented in Table 7.2.

Table 7.2. Activation energy E_T, apparent capture cross section σ_{app} and concentration N_T of the observed defects.

Defect label	E_T (eV)	σ_{app} (cm^2)	N_T (cm^{-3})
$E_{0.10}$	0.10 ±0.01	1×10^{-13}	9.1×10^{13}
$E_{0.12}$	0.12 ±0.01	7×10^{-15}	2.2×10^{11}
$E_{0.18}$	0.18 ±0.01	6×10^{-15}	5.4×10^{11}
$E_{0.42}$	0.42 ±0.03	8×10^{-15}	$*6.2 \times 10^{13}$
$E_{0.62}$	0.62 ±0.02	2×10^{-14}	-
$E_{0.69}$	0.69 ±0.02	8×10^{-15}	$*9.3 \times 10^{13}$
$E_{0.76}$	0.76 ±0.03	1×10^{-14}	$*4.9 \times 10^{13}$

* Concentration value obtained after irradiation at fluence of 4.9×10^{14} cm^{-2}

7.2.4.2 Annealing of irradiated diodes

After irradiation to a total fluence of $5.4 \times 10^{14}\ cm^{-2}$, the diodes were then isochronally annealed in steps of 100 ºC in flowing argon to a maximum temperature of 600 ºC. The annealing was done at each temperature for 15 minutes and the same DLTS measurements were repeated after each anneal. The normalized DLTS spectra obtained are shown in Figure 7.12.

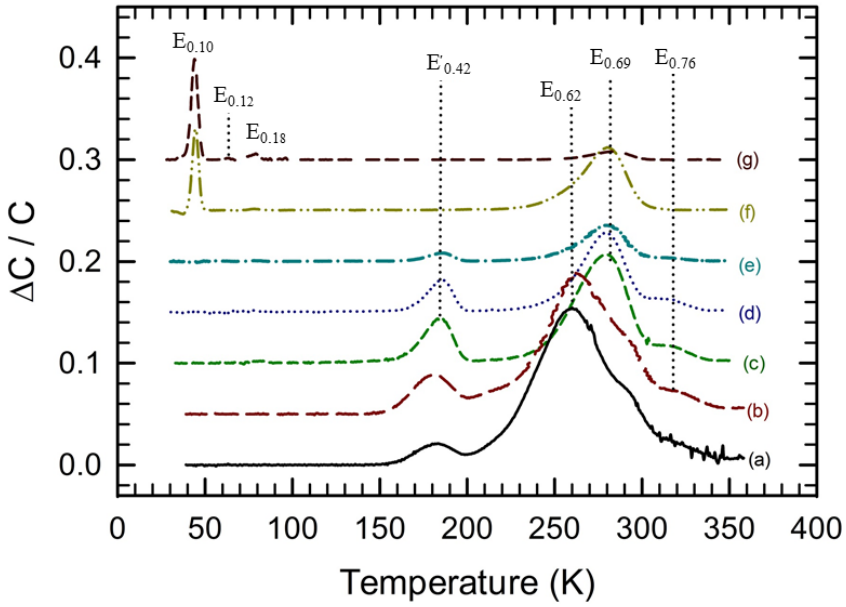

Figure 7.12 DLTS spectra obtained after different annealing steps. The spectra obtained before and after irradiation at 5.4 × 10^{14} cm^{-2} are also shown for comparison. (a) after irradiation, (b) 100 °C, (c) 200 °C, (d) 300 °C, (e) 400 °C, (f) 500 °C and (g) as prepared. The 500 °C and 600 °C spectra were similar hence the 600 °C spectrum is not shown.

The first change resulting from the heat treatment is observed on the $E_{0.62}$ level. The concentration of the defect is lowered greatly after annealing at 200 °C for only 15 minutes. After 200 °C, the level annealed out. It can be seen from this that the $E_{0.62}$ level is very unstable. While the $E_{0.69}$ level concentration reduces with annealing, after annealing at 500 °C, the level still has more concentration compared to the as-deposited values.

The $E_{0.42}$ and $E_{0.76}$ defect levels show a decrease in concentration with annealing but were only annealed out completely after a 500 °C anneal. It is interesting that these defects have the same annealing behaviour. It is possible that the two act as annealing sinks to the same type of mobile defects or they require the same annealing sink hence the same annealing temperature [21].

The effect of annealing on levels $E_{0.12}$ and $E_{0.18}$ was not noticeable due to the low concentration of the defects. Level $E_{0.10}$ which had been completely suppressed by irradiation shows recovery after annealing at 500 °C. The reason why irradiation suppresses this level with a reversal from annealing remains to be investigated.

7.2.4.3 DLTS results conclusion

Electron irradiation up to fluence of 5.4 × 10^{14} cm^{-2} introduced three defect levels $E_{0.42}$, $E_{0.62}$ and $E_{0.76}$. The level $E_{0.62}$ was annealed out at a low temperature of 200 °C. Levels $E_{0.42}$ and

$E_{0.76}$ were relatively stable up to annealing temperatures of 400 °C although the concentrations were reduced progressively. After annealing at 500 °C, these levels were completely annealed out. Level $E_{0.10}$ which is a nitrogen impurity was completely suppressed by irradiation but was recovered after annealing at 500 °C.

7.3 Alpha-particle irradiation results

7.3.1 Introduction

Alpha particle irradiation using a radioactive Am-241 source was done on the samples to fluence of 2.6×10^{10} cm^{-2} (this fluence corresponds to 60 minute irradiation). *I-V*, *C-V* and DLTS measurements were carried out both before and after irradiation. Results are also presented for measurements done with annealing of the irradiated diodes up to 600 °C from 100 °C. The free carrier removal rate was determined from *C-V* measurements.

7.3.2 Current-voltage results

I-V characteristics of the nickel Schottky contacts before and after alpha particle irradiation are shown in Figure 7.13. A linear forward *I-V* curve for the as deposited diodes is obtained. This shows that the thermionic emission model can be successfully used in explaining the current transport mechanism across the metal-semiconductor interface. The ideality factor before irradiation was obtained as 1.05. Such an ideality factor that is close to unity shows that any other transport mechanism that may be present is negligible.

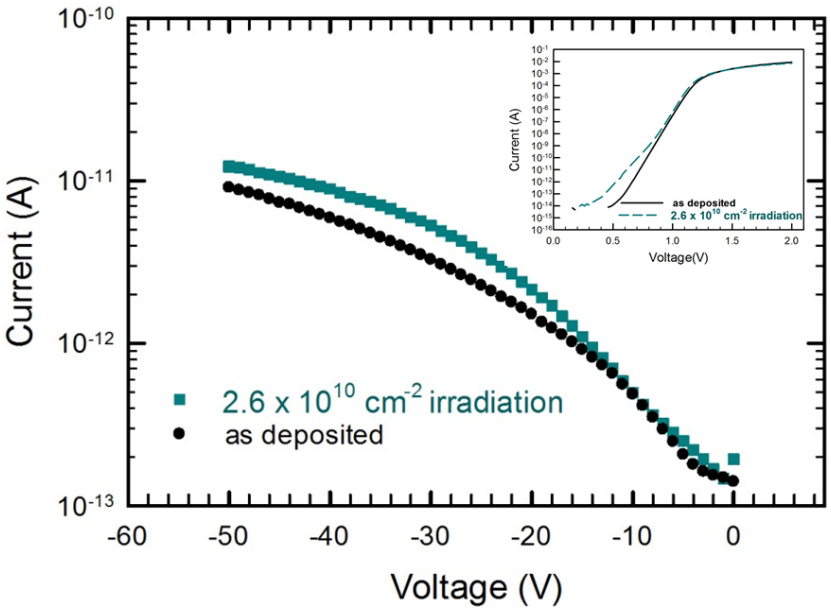

Figure 7.13 Reverse and forward (Insert) semi-logarithmic *I-V* curves before and after irradiation with 5.4 MeV alpha particles up to a fluence of 2.6×10^{10} cm^{-2}. Intermediate fluence curves are not plotted.

The forward *I-V* curve obtained after irradiation deviates from linearity at lower voltages. This is possibly due to the fact that irradiation produced defects may lead to generation recombination current hence the non-linearity at low voltages. The ideality factor was obtained as 1.35 after irradiation. This value is fairly large and shows that indeed there could be a contribution of generation recombination current.

Measured at -50 V, the reverse leakage current increased from 9.1×10^{-12} A before irradiation to 1.2×10^{-11} A after irradiation with fluence of 2.6×10^{10} cm^{-2}. At lower voltages, up to -20 V, the reverse leakage remains relatively constant comparing the as-deposited and the irradiated data. The increase in the reverse leakage current can be directly attributed to defect creation where introduced generation recombination centres are responsible for the increase in the leakage current.

The diode maintained good rectification even after irradiation indicating the high resistance of SiC to radiation damage. The ideality factor values, close to unity even after irradiation, indicate charge transport mechanism across the Schottky barrier dominated by the thermionic emission.

7.3.3 Capacitance-voltage results

C-V measurements were performed to obtain the change in free carrier concentration with irradiation and annealing of irradiated diodes. The free carrier removal rate was estimated

from the change in free carrier concentration during irradiation. The SBH was also determined from *C-V* measurements.

7.3.3.1 SBH and free carrier concentration

The SBH before and after irradiation were obtained from the voltage intercept of the $1/C^2$ vs. *V* curves. Due to the non-linear nature of the curves, the -2 V ≤ V ≤ 0 V part of the curve was considered in determining the SBH. The SBH before irradiation was obtained as 1.86 eV and increased to 2.02 eV after irradiation at fluence of 2.6 × 10^{10} cm^{-2}. The increase in the SBH can be seen from Figure 7.14 where the voltage intercept of the $1/C^2$ vs. *V* curve increases after irradiation. There were no major change in the curves at intermediate irradiation fluences.

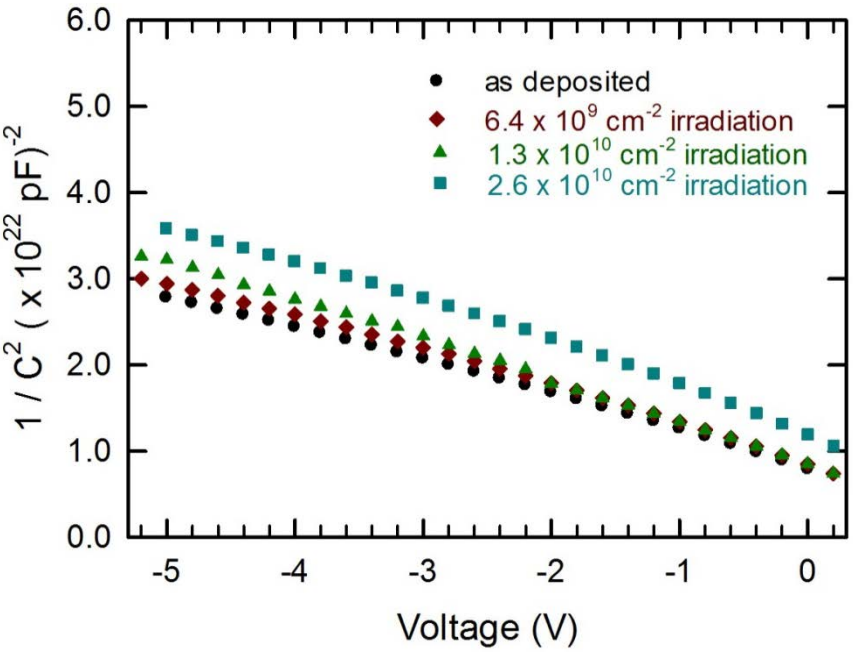

Figure 7.14 Graph of 1 / C^2 against Voltage before and after irradiation with 5.4 MeV alpha particles.

The free carrier concentration was observed to change from 4.9 × 10^{14} cm^{-3} before irradiation to 2.9 × 10^{14} cm^{-3} after irradiation at fluence of 2.6 × 10^{10} cm^{-3}. Non-linear curves of $1/C^2$ against voltage, Figure 7.14 shows that the free carrier concentration is not constant below the metal-semiconductor junction. This is also shown by the depth profiles, Figure 7.16, discussed later.

7.3.3.2 Free carrier removal rate

The free carrier removal rate was determined for 5.4 MeV alpha-particles after irradiation at three different fluences up to 2.6 × 10^{10} cm^{-2} as 15 101 cm^{-1}. Previous studies with 8 MeV protons on 4H-SiC lead to a free carrier removal rate of 116 cm^{-1} [13]. This value is lower since protons are less massive compared to alpha particles. It is substantially largeer than the value obtained after electron irradiation in this study, Section 7.2.3.3. The graph used for the calculation of carrier removal rate due to alpha particle irradiation is shown in Figure 7.15.

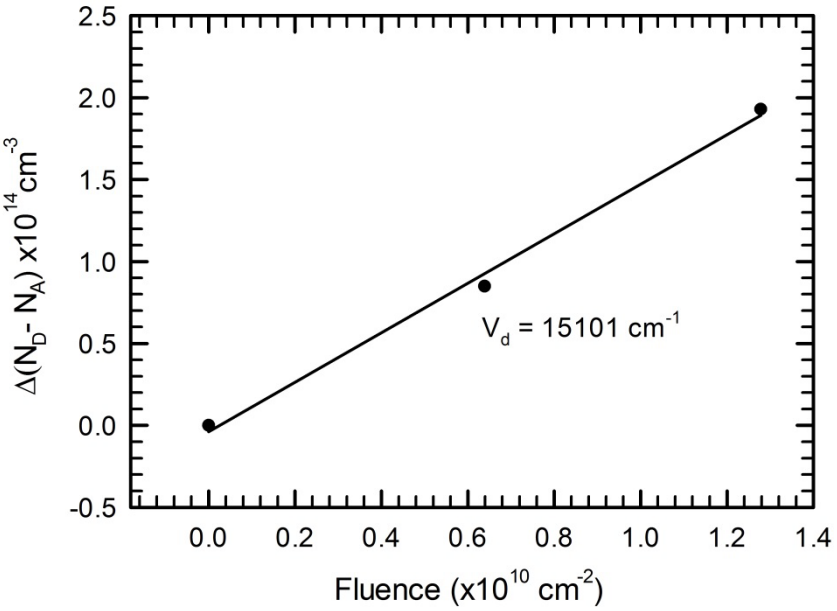

Figure 7.15 Free carrier removal rate graph for 5.4 MeV alpha-particles.

Equation 4.3 can be used to explain the large carrier removal rate produced by alpha-particle irradiation compared to the obtained values for electron irradiation. Alpha particles have a larger mass compared to electrons and more energy (in this study) hence the transferred energy is expected to be higher. More damage is also expected from the alpha-particle irradiations due to cascade collisions that are expected as a result of a larger transferred energy.

7.3.3.3 Free carrier concentration with annealing

The free carrier concentration was analysed as the irradiated diodes were annealed in argon in steps of 100 °C in the temperature range 100 °C ≤ T ≤ 600 °C. The depth profiles obtained

before irradiation, after irradiation at fluence of 2.6×10^{10} cm^{-2} and at different annealing temperatures are shown in Figure 7.16.

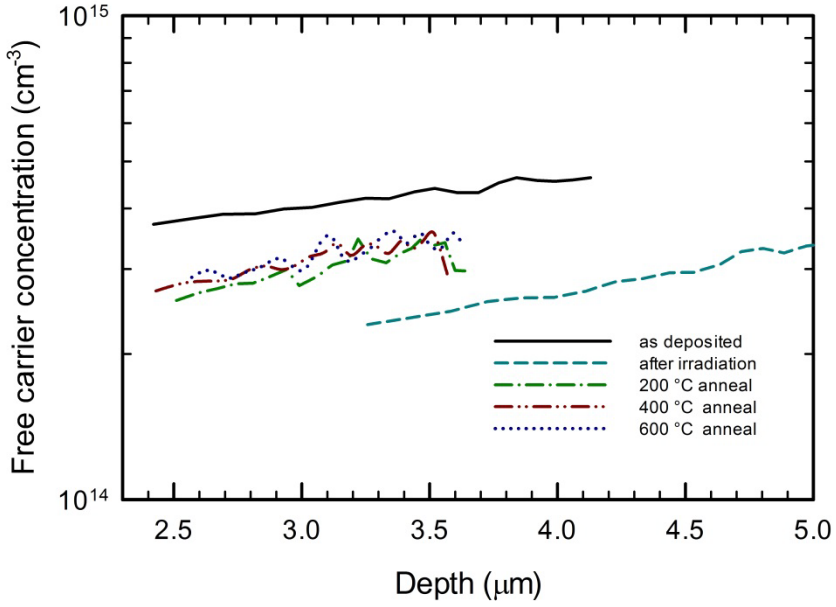

Figure 7.16 The free carrier concentration determined by *C-V* measurements before irradiation, after irradiation at 2.6×10^{10} cm^{-2}, and with annealing up to 600 °C.

The free carrier concentration increased after annealing at 200 ˚C from a depleted profile obtained after irradiation. Further annealing up to 600 °C does not lead to increased recovery in the region probed by *C-V* measurements.

7.3.4 Conclusions on I-V and C-V results

Alpha particle irradiation to fluence of 2.6×10^{10} cm^{-2} lead to minimum degradation of diode characteristics. The SBH from both *I-V* and *C-V* measurements increased to some extent after irradiation while the ideality factor remained close to unity. There was a reduction in the free carrier concentration due to irradiation and some recovery was realised after annealing at 200 °C. No further recovery at higher annealing temperatures of up to 600 °C was realised. A large carrier removal rate was calculated compared to the value obtained from electron irradiation, this is expected. Table 7.3 summarises the *I-V* and *C-V* parameters obtained with alpha-particle irradiation.

Table 7.3 Diode characteristics before and after 5.4 MeV alpha particle irradiation to fluence of 2.6×10^{10} cm^{-2}.

	n	Φ_{IV}(eV)	Φ_{CV}(eV)	I_R [A] (at -50 V)	Free carrier density (cm^{-3})
Before irradiation	1.05	1.21	1.86	9.0×10^{-12}	4.9×10^{14}
After irradiation	1.35	1.28	2.09	1.2×10^{-11}	2.9×10^{14}

The degradation of the diodes that has been reported from *I-V* and *C-V* results is most probably due to the creation of defects as a result of irradiation. DLTS results are presented in section 7.3.5.

7.3.5 DLTS results and discussion

The DLTS spectra obtained from the as deposited diodes is exactly the same as those presented for electron irradiation, Figure 7.7, showing the presence of four energy levels, $E_{0.10}$, $E_{0.12}$, $E_{0.18}$ and $E_{0.69}$. The nature of these defects has been discussed in section 7.2.4.

After irradiation with 5.4 MeV alpha particles, DLTS measurements were carried out in the temperature range 30K ≤ T≤ 350K. The diodes were then annealed in steps of 100 °C up to 600 °C, the normalized spectra obtained is shown in Figure 7.17

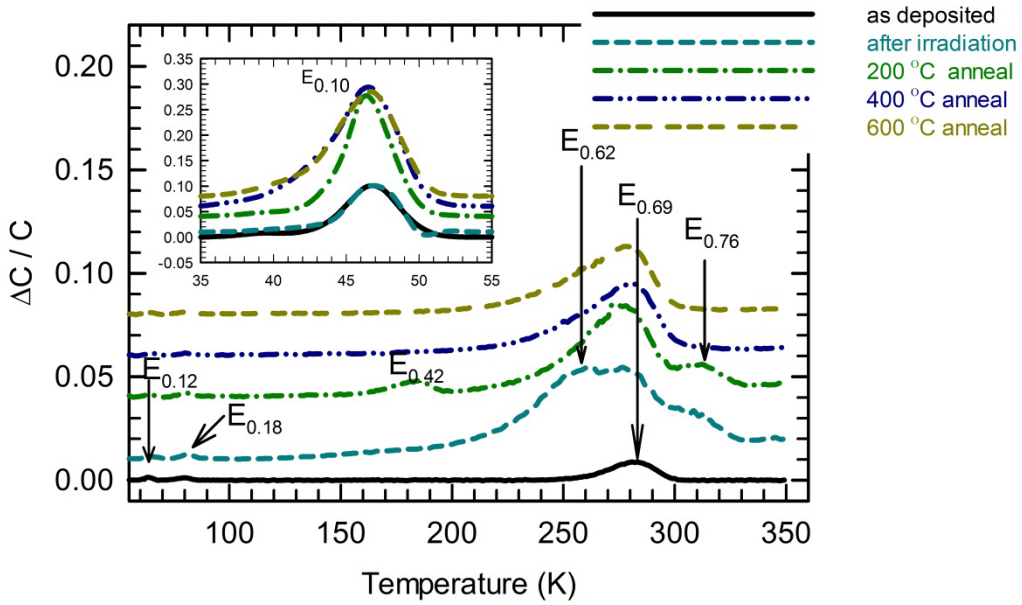

Figure 7.17 DLTS spectra showing change in concentration of $E_{0.10}$, insert and $E_{0.69}$ after irradiation.

7.3.5.1 $E_{0.69}$

As can be seen from Figure 7.17, there is a marked increase in the concentration of level $E_{0.69}$ after irradiation. It is also seen from the spectra obtained after irradiation that level $E_{0.69}$ does not only increase in concentration but also becomes broader. This is an indication that another level with almost similar activation energy might be superimposed on $E_{0.69}$. Electron, proton and alpha particle irradiations performed on SiC has been shown to introduce similar defects but of different concentrations [31]. It is therefore possible that this defect, although

not characterized can be linked to the $E_{0.62}$ level that was observed after electron irradiation, section 7.2.4. Hemmingsson *et al* [32] reported that the defect is composed of two closely spaced levels that have negative U behaviour. Asghar *et al* [33] shows that the defect, generally referred to as the Z_1 defect is present as a single defect, but is transformed into Z_1/Z_2 after 5.48 MeV alpha particle irradiation. This is due to the superimposition of a new defect which is attributed to a silicon vacancy, the Z_2 defect [33]. The increase in the concentration of defect $E_{0.69}$ observed in this study can support the possibility that there is a new defect that is superimposed on level $E_{0.69}$. The high energy of used alpha particles also enables the creation of silicon vacancies. The broadening of level $E_{0.69}$ reduces progressively with annealing from 200 °C to 600 °C. The concentration of the peak is also observed to reduce but remains higher after annealing at 600 °C compared to that before irradiation.

L-DLTS measurements were done varying the voltage pulse height to obtain the concentrations of $E_{0.69}$ and $E_{0.76}$ at different depths using Equations 5.21 and 5.22, which takes into consideration the λ effect. The depth profiles are given in Figure 7.18 together with the profile obtained before irradiation for $E_{0.69}$, for comparison. It is seen from the graph that the concentration of both defects is constant in the investigated depth range. This is in agreement with the prediction of SRIM simulations where the vacancy concentration is constant to a depth of ~ 18 μm.

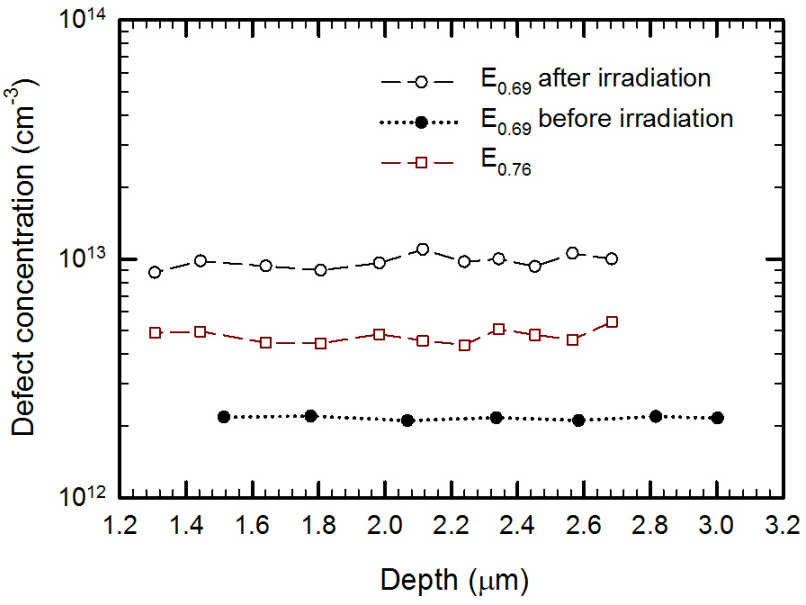

Figure 7.18 Depth profiles for levels $E_{0.69}$ and $E_{0.76}$. The concentration of $E_{0.69}$ is presented before and after alpha-particle irradiation to fluence of 2.6×10^{10} cm^{-2} and that of $E_{0.76}$ is obtained after irradiation.

7.3.5.2 $E_{0.76}$ and $E_{0.42}$

In addition to the broadening of level $E_{0.69}$, another peak appearing as a shoulder on the higher temperature side of $E_{0.69}$ was observed. The diodes were then annealed and no relevant change in the spectra was observed after annealing at 100 °C. After annealing at 200 °C, the shoulder could be seen more clearly and was characterised. Another defect, $E_{0.42}$ level was observed at temperatures ~ 175 K (using a 2.5 s^{-1} rate window). Arrhenius plots obtained from L-DLTS for both the as-deposited and irradiation induced defects are shown in Figure 7.19.

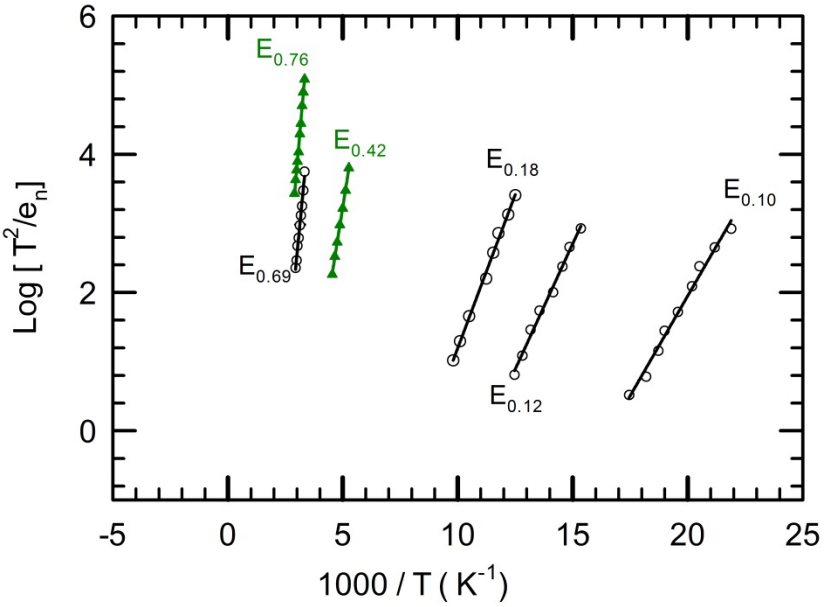

Figure 7.19 Arrhenius plots obtained using L-DLTS. Plots with empty circles represent defects present before irradiation.

The defect appearing as a shoulder of $E_{0.69}$ was found to have activation energy of E_C-0.76 eV. This is the same activation energy for level $E_{0.76}$ that was observed after electron irradiation, section 7.2.4. It is however difficult to compare the concentrations of the two since the diodes had to be annealed first after alpha particle irradiation, thus the concentration would be expected to decrease. Consequently the concentration after annealing at 200 °C was obtained as ~ 4.0×10^{13} cm^{-3} compared to 5×10^{13} cm^{-3} obtained after electron fluence of 5.4×10^{14} cm^{-2} without annealing. The apparent capture cross section area obtained after both the irradiations are comparable.

Level $E_{0.42}$ was observed after annealing the irradiated samples at 200 °C. The level has activation energy of E_C-0.42 eV, the same as $E_{0.42}$ observed after electron irradiation. The only difference is that after alpha particle irradiation the samples had to be annealed first

before the defect could be observed. The concentration was obtained as 2.8×10^{13} cm^{-3} which is lower than that obtained after electron irradiation, but this is possibly a result of annealing.

After annealing at 400 °C, both $E_{0.42}$ and $E_{0.76}$ were annealed out. The two defect levels were annealed out at the same temperature, the same scenario that was observed after electron irradiation. The theories that the two defects either act as annealing sinks for the same type of mobile defects or they require the same type of annealing sink are supported by the results of alpha particle irradiation.

7.3.5.3 $E_{0.10}$

A rather unexpected result was observed on level $E_{0.10}$. After alpha particle irradiation at fluence of 2.6×10^{10} cm^{-2}, the concentration remained unchanged but an increase to nearly four times the original value was observed after annealing at 200 °C. The concentration then remained unchanged after annealing at 600 °C. The diodes became highly resistive after annealing at 700 °C. While the $E_{0.10}$ level is a nitrogen impurity, it is not clear what the cause of the increase in concentration after irradiation is. This finding is also in contrast to the result obtained after electron irradiation where the concentration reduces with irradiation to below detectable limits before some recovery with annealing.

7.3.5.4 DLTS results conclusion

A strong correlation was found between the defects produced by alpha particle irradiation and those produced by electron irradiation. Levels $E_{0.42}$ and $E_{0.76}$ were clearly observed after annealing irradiated diodes at 200 °C and were both annealed out at 400°C. Level $E_{0.10}$ increases in concentration after irradiation and annealing at 200 °C. The parameters obtained from DLTS measurements are summarised in Table 7.4

Table 7.4 Activation energies, apparent capture cross sections and concentrations of as grown and irradiation induced defects observed by DLTS in 4H-SiC after 5.4 MeV irradiation and annealing.

Trap level	$E_c - E_t$(eV)	σ_{app} (cm^2)	N_T before irradiation (cm^{-3})	N_T after irradiation (cm^{-3})	Attribution
$E_{0.10}$	0.10 ±0.01	7×10^{-14}	9.4×10^{13}	2.0×10^{14}	N impurity - [15]
$E_{0.12}$	0.12±0.01	1×10^{-14}	2.2×10^{11}	2.1×10^{11}	Ti impurity- [29]
$E_{0.18}$	0.18±0.01	1×10^{-14}	5.4×10^{11}	5.4×10^{11}	Ti impurity- [18, 19]
$E_{0.42}$	0.42±0.03	1×10^{-15}	-	2.8×10^{13}	V_{Si} - [34]
$E_{0.69}$	0.69±0.02	2×10^{-14}	1.2×10^{13}	9.4×10^{13}	Z_1/Z_2 - [22]
$E_{0.76}$	0.76±0.03	5×10^{-14}	-	$*1.0 \times 10^{13}$	-

* Value obtained after irradiation and annealing at 200 °C

7.4 Proton irradiation results

7.4.1 Introduction

Proton irradiation was done to fluence of 1.0×10^{12} cm^{-2} with 1.6 MeV accelerated protons. The diodes became highly resistive immediately after irradiation and hence had to be annealed before further measurements could be done. Annealing was performed in steps of 100 °C from 125 °C to 725 °C. *I-V*, *C-V* and DLTS results obtained before irradiation and after irradiation and annealing are presented. The free carrier removal rate and the defect introduction rates were not determined since only single proton fluence was used in the irradiation.

7.4.2 Current-voltage results

I-V measurements obtained before proton irradiation show good rectification of the fabricated diodes with an ideality factor of 1.15. A low resistance value of 32 Ω was obtained and the SBH was obtained as 1.42 eV. Forward and reverse semi-logarithmic *I-V* curves obtained before irradiation and after proton irradiation and subsequent annealing are shown in Figure 7.20. It can be seen from the as deposited curve that the current changes by about twelve orders of magnitude between -2V and +2V, a sign of good rectifying diodes.

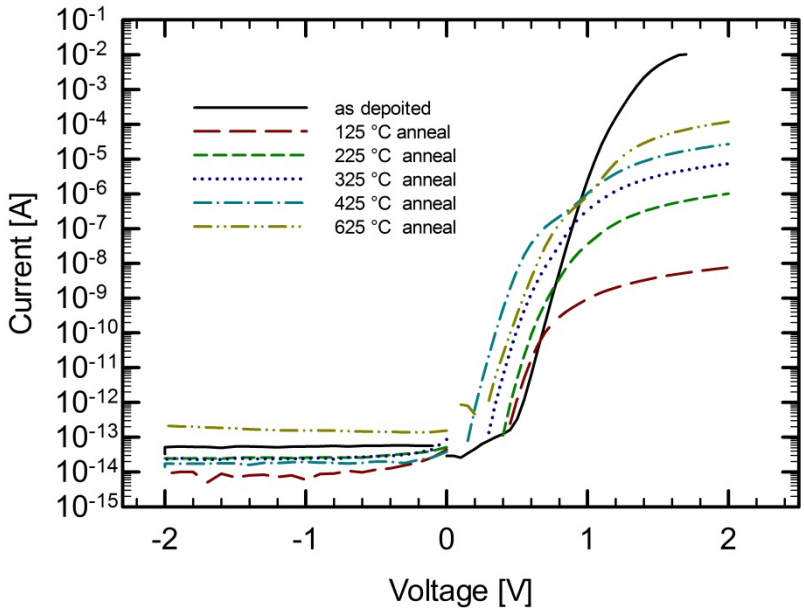

Figure 7.20 Semi-Logarithmic forward and reverse I-V curves obtained before irradiation and after irradiation and annealing from 125 °C to 625 °C.

After irradiation there was severe degradation of the diode properties and the diodes had to be annealed before measurements. This was mainly due to an increase in series resistance. After annealing at 125 °C, the *I-V* curve obtained shows that the rectification was still reduced, with the current measured at 1.7 V being only 7.8×10^{-9} A compared to 1.1×10^{-2} A obtained before irradiation at the same voltage. The forward current increased with annealing temperature to 6.4×10^{-5} A at 1.7 V. Although this value is still lower than the as deposited value, considerable rectification was retained with increasing annealing temperature after irradiation. There is an increase in the forward current observed on proton irradiated diodes compared to the as deposited diodes at low voltages, < 1V. This is possibly due to the contribution of generation recombination current resulting from atomic displacements created by proton bombardment.

The increasing forward current was accompanied by a subsequent decrease in series resistance, Figure 7.21. The resistance decreases from ~ 0.7 MΩ after annealing at 225 °C to ~ 600 Ω after annealing at 625 °C. Consequently the forward current increased from 5.4×10^{-9} A to 6.4×10^{-5} A after respective annealing temperatures.

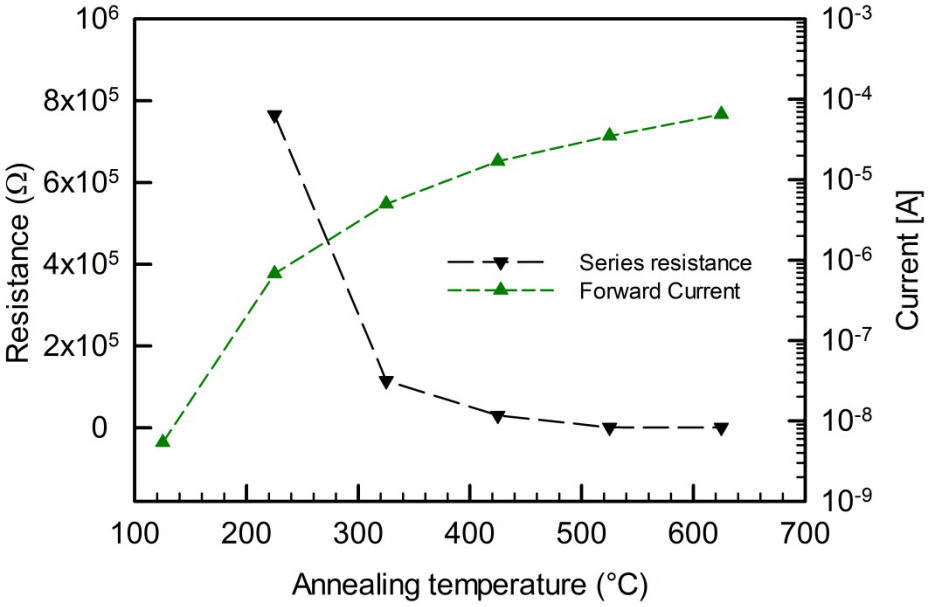

Figure 7.21 Effect of annealing on series resistance and forward current measured at 1.6 V after proton implantation at fluence of 1×10^{12} cm^{-2}.

There was no significant change in the reverse leakage current after irradiation and after subsequent annealing, measured up to -2V. The reverse leakage current remained generally below the values obtained before irradiation. Several authors have reported decreases in reverse leakage current in 4*H*-SiC after proton irradiation [35-38]. While the introduction of generation recombination centres by particle irradiation is expected to be associated with an increase in reverse leakage current, it is also possible that proton irradiation anneals out some defects that were otherwise responsible for high leakage current before irradiation [39].

7.4.2 Capacitance-voltage results

The damage induced by proton irradiation was more visible from *C-V* measurements. The effect of compensation is shown in Figure 7.22 where the free carrier concentration was reduced to below detectable values immediately below the metal semiconductor junction. Limited recovery was attained by annealing up to 625 °C where the concentration was obtained as 2.8×10^{14} cm^{-3} around 4 µm below the junction. Annealing at 725 °C led to a reduction in the free carrier concentration.

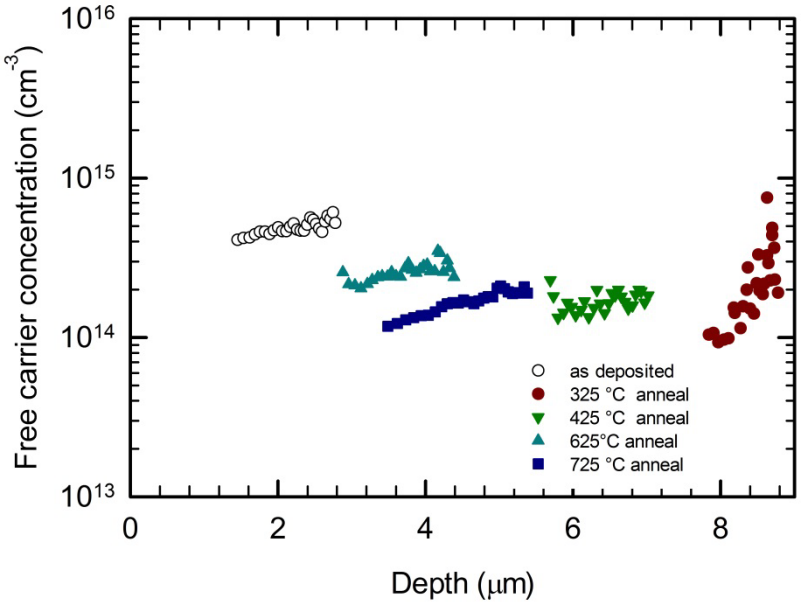

Figure 7.22 Free carrier concentration depth profiles for 1 × 10^{12} cm^{-2} proton irradiated and annealed diodes.

7.4.2.1 Conclusions to I-V and C-V results

Effect of proton irradiation was clearly observable from both *I-V* and *C-V* measurement results. A reduction in the diode rectification was observed and series resistance increased to MΩ ranges after irradiation. An appreciable degree of rectification was achieved through annealing up to 625 °C. The free carrier concentration was reduced and only a small degree of recovery was retained after annealing at 625 °C and annealing at 725 °C lead to a further reduction in the concentration.

7.4.3 DLTS results and discussion

DLTS measurements were obtained after 1 × 10^{12} cm^{-2} proton irradiation and after annealing the irradiated diodes. Shown in Figure 7.23 is the as deposited spectra together with the spectra obtained after annealing the irradiated diodes at 325 °C, 425 °C and at 625 °C. Levels $E_{0.76}$ and $E_{0.42}$ were observed after annealing the irradiated diodes at 225 °C and were still present after a 325 °C anneal.

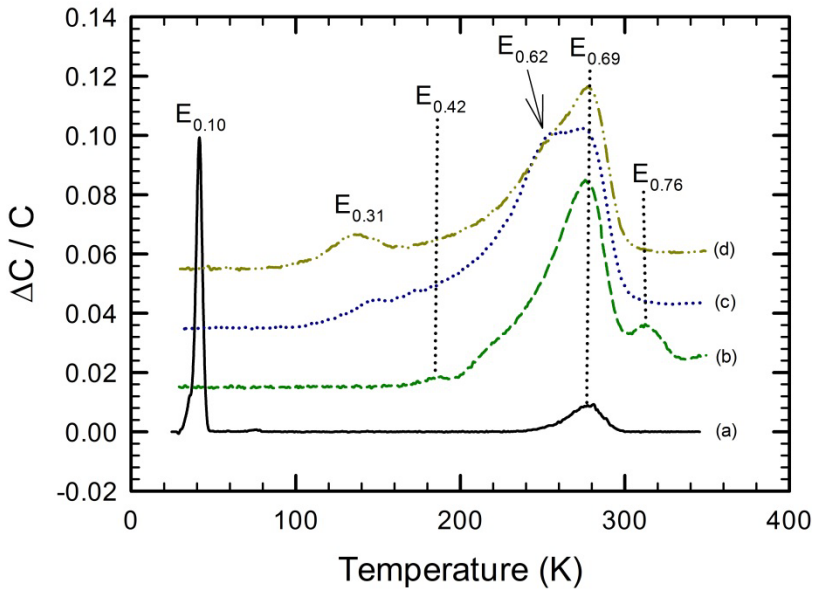

Figure 7.23 DLTS spectra obtained: (a) before irradiation, after proton irradiation to fluence of 1×10^{12} $cm^{-2}$and annealing at (b) 325 °C, (c) 425 °C and (d) 625 °C.

Changes in the spectra were observed after annealing the diodes at 425 °C where level $E_{0.42}$ was annealed out and two new defect levels were observed at 0.31 eV and 0.62 eV. Level $E_{0.62}$ has been observed after electron irradiation and was speculated to be present in the alpha particle irradiated samples due to broadening of level $E_{0.69}$. This defect level has however been observed immediately after irradiation and annealed out at lower temperatures in these irradiations.

Level $E_{0.31}$ on the other hand was not observed after electron and alpha particle irradiations. This level has a low apparent capture cross section of 2×10^{-15} cm^2. This level is stable and is observed to be still present even after annealing the irradiated diodes at 625 °C. A defect level with almost similar activation energy, 0.32 eV has been observed after electron irradiation and attributed to a carbon interstitial [19, 26]. Arrhenius plots used in the calculation of the defect signatures are given in Figure 7.24.

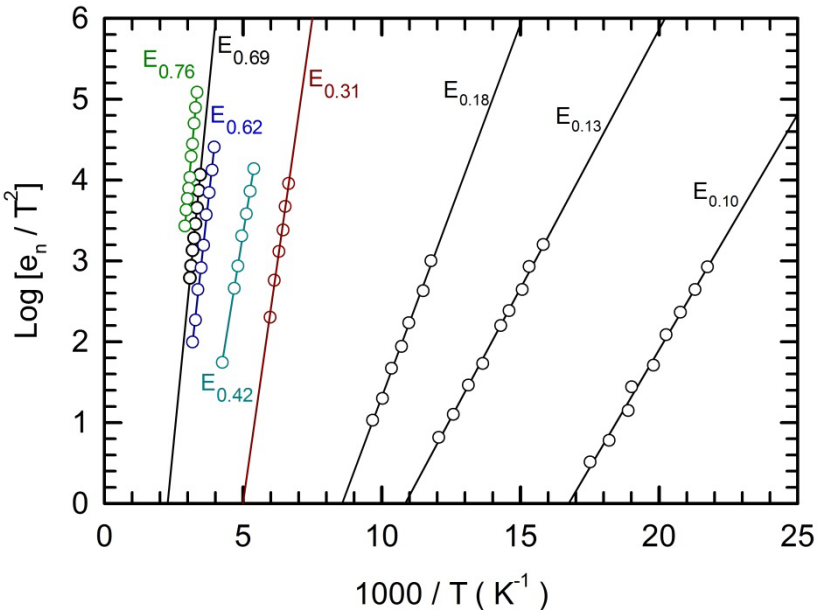

Figure 7.24 Arrhenius plots obtained for defect levels obtained before and after proton irradiation. Plots for $E_{0.42}$, $E_{0.62}$, $E_{0.76}$ and $E_{0.31}$ were obtained after irradiation.

7.4.3.1 Conclusions to DLTS results

In addition to levels $E_{0.42}$, $E_{0.62}$ and $E_{0.76}$ that have been observed after electron and alpha particle irradiation, a new defect level with activation energy 0.31 eV was observed. This level is observed after annealing the irradiated diodes at 425 °C and was still present after annealing at 625 °C.

References

[1] H.L. Skriver, N.M. Rosengaard, H.L. Skriver, N.M. Rosengaard, Surface energy and work function of elemental metals, Physical Review B Condensed Matter, **46** (1992) 7157.

[2] F Roccaforte, F. Giannazzo, V. Raineri, Nanoscale transport properties at silicon carbide interfaces, Journal of Physics D : Applied Physics, **43** (2010) 223001.

[3] J.R. Lince, D.J. Carré, P.D. Fleischauer, Schottky-barrier formation on a covalent semiconductor without Fermi-level pinning: The metal-MoS2(0001) interface, Physical Review B **36** (1987) 1647.

[4] R.T. Tung, Recent advances in Schottky barrier concepts, Materials Science and Engineering: R: Reports, **35** (2001) 1.

[5] H. Benmaza, B. Akkal, H. Abid, J.M. Bluet, M. Anani, Z. Bensaad, Barrier height inhomogeneities in a Ni/SiC-6H Schottky *n*-type diode, Microelectronics Journal, **39** (2008) 80.

[6] J.H. Werner, H.H. Güttler, Barrier inhomogeneities at Schottky contacts, Journal of Applied Physics, **69** (1999) 1522.

[7] B.J. Baliga, Advanced Power Rectifier Concepts, Springer Scientific, New York, 2009.

[8] J.H. Zhao, K. Sheng, R.C. Lebron-Velilla, Silicon carbide schottky barrier diode, International Journal of High Speed Electronics and Systems, **15** (2005) 821.

[9] L. Calcagno, F. La Via, G. Foti, G. Izzo, G. Litrico, Compensation Effects in 7 MeV C Irradiated n-Doped 4H-SiC in, Materials Science Forum, Stafa-Zurich, SUISSE, 2009, pp. 619.

[10] T. Kimoto, T. Urushidani, S. Kobayashi, H. Matsunami, High-voltage (>1 kV) SiC Schottky barrier diodes with low on-resistances, Electron Device Letters, IEEE, **14** (1993) 548.

[11] V.V. Emtsev, A.M. Ivanov, V.V. Kozlovski, A.A. Lebedev, G.A. Oganesyan, N.B. Strokan, G. Wagner, Similarities and distinctions of defect production by fast electron and proton irradiation: Moderately doped silicon and silicon carbide of *n*-type, Semiconductors, **46** (2012) 456.

[12] F.D. Auret, S.A. Goodman, M. Hayes, M.J. Legodi, H.A. van Laarhoven, D.C. Look, Electrical characterization of 1.8 MeV proton-bombarded ZnO, Applied Physics Letters, **79** (2001) 3074.

[13] V.V. Kozlovski, V.V. Emtsev, A.M. Ivanov, A.A. Lebedev, G.A. Oganesyan, D.S. Poloskin, N.B. Strokan, Charge carrier removal rates in *n*-type silicon and silicon carbide subjected to electron and proton irradiation, Physica B: Condensed Matter, **404** (2009) 4752.

[14] T. Kimoto, A. Itoh, H. Matsunami, S. Sridhara, L. L. Clemen, R. P. Devaty, W.J. Choyke, T. Dalibor, C. Peppermüller, G. Pensl, Nitrogen donors and deep levels in high-quality 4H–SiC epilayers grown by chemical vapor deposition, Applied Physics Letters, **67** (1995) 2833.

[15] A. Castaldinia, A. Cavallinia, L. Polentaa, F.Navab, C. Canalic, C. Lanzierid, Deep levels in silicon carbide Schottky diodes, Applied Surface Science, **187** (2002) 248.

[16] C.Q. Chen, J. Zeman, F. Engelbrecht, C. Peppermüller, R. Helbig, Z.H. Chen, G. Martinez, Photothermal ionization spectroscopy of shallow nitrogen donor states in 4H–SiC, Journal of Applied Physics, **87** (2000) 3800.

[17] A.O. Evwaraye, S.R. Smith, W.C. Mitchel, Electrical and Optical Properties of Defects in *N*-Type 4h-SiC, MRS Online Proceedings Library, **410** (1995).

[18] N. Achtziger, W. Witthuhn, Band gap states of Ti, V, and Cr in 4H–silicon carbide, Applied Physics Letters, **71** (1997) 110.

[19] A. Castaldini, A. Cavallini, L. Rigutti, F. Nava, S. Ferrero, F. Giorgis, Deep levels by proton and electron irradiation in 4H–SiC, Journal of Applied Physics, **98** (2005) 053706.

[20] T. Hiyoshi, T. Kimoto, Elimination of the Major Deep Levels in n- and *p*-Type 4H-SiC by Two-Step Thermal Treatment, Applied Physics Express, **2** (2009) 091101.

[21] L. Storasta, J.P. Bergman, E. Janzén, A. Henry, J. Lu, Deep levels created by low energy electron irradiation in 4H-SiC, Journal of Applied Physics, **96** (2004) 4909.

[22] I. Pintilie, L. Pintilie, K. Irmscher, B. Thomas, Formation of the Z1,2 deep-level defects in 4H-SiC epitaxial layers: Evidence for nitrogen participation, Applied Physics Letters, **81** (2002) 4841.

[23] J. Zhang, L. Storasta, J. P. Bergman, N. T. Son, E. Janzén, Electrically active defects in *n*-type 4H–silicon carbide grown in a vertical hot-wall reactor, Journal of Applied Physics, **93** (2003) 4708.

[24] C. Hemmingsson, N.T. Son, O. Kordina, J.P. Bergman, E. Janzen, J.L. Lindstrom, S. Savage, N. Nordell, Deep level defects in electron-irradiated 4H SiC epitaxial layers, Journal of Applied Physics, **81** (1997) 6155.

[25] P. Bergman, E. Janzén, A. Henry, L. Storasta, Investigations of possible nitrogen participation in the Z1/Z2 defect in 4H-SiC, in: Materials Science Forum, **457-460**(2004) 469.

[26] J. P. Doyle, M. K. Linnarsson, P. Pellegrino, N. Keskitalo, B.G. Svensson, A. Scho¨ner, N. Nordell, J.L. Lindstrom, Electrically active point defects in *n*-type 4H–SiC, Journal of Applied Physics, **84** (1998) 1354.

[27] F. Nava, G. Bertuccio, A. Cavallini, E. Vittone, Silicon carbide and its use as a radiation detector material, Measurement Science and Technology, **19** (2008) 102001.

[28] A. Gali, N.T. Son, E. Janzen, Electrical characterization of metastable carbon clusters in SiC: A theoretical study, Physical Review B, **73** (2006) 033204.

[29] T.A.G. Eberlein, R. Jones, P.R. Briddon, Z1/Z2 Defects in 4H-SiC, Physical Review Letters, **90** (2003) 225502-225501.

[30] A. Castaldini, A. Cavallini, L. Rigutti, F. Nava, Low temperature annealing of electron irradiation induced defects in 4H-SiC, Applied Physics Letters **85** (2004) 3780.

[31] A.A. Lebedev, A.I. Veinger, D.V. Davydov, V.V. Kozlovski, N.S. Savkina, A.M. Strel'chuk, Doping of *n*-type 6H–SiC and 4H–SiC with defects created with a proton beam, Journal of Applied Physics, **88** (2000) 6265.

[32] C.G. Hemmingsson, N.T. Son, A. Ellison, J. Zhang, E. Janzen, Negative-U centers in 4H silicon carbide, Physical Review B, **58** (1998) 119.

[33] M. Asghar, I. Hussain, H.S. Noor, F. Iqbal, Q. Wahab, A.S. Bhatti, Properties of dominant electron trap center in *n*-type SiC epilayers by means of deep level transient spectroscopy, Journal of Applied Physics, **101** (2007) 073706.

[34] T.A.G. Eberlein, R. Jones, P.R. Briddon, Z1/Z2 Defects in 4H-SiC, Physical Review Letters, **90** (2003) 225502.

[35] S. Nigam, J. Kim, F. Ren, G.Y. Chung, M.F. MacMillan, R. Dwivedi, T.N. Fogarty, R. Wilkins, K.K. Allums, C.R. Abernathy, S.J. Pearton, J.R. Williams, High energy proton irradiation effects on SiC Schottky rectifiers, Applied Physics Letters, **81** (2002) 2385.

[36] R.D. Harris, A.J. Frasca, M.O. Patton, Displacement damage effects on the forward bias characteristics of SiC Schottky barrier power diodes, IEEE Transactions on Nuclear Science, **52** (2005) 2408.

[37] Z. Luo, T. Chen, A.C. Ahyi, A.K. Sutton, B.M. Haugerud, J.D. Cressler, D.C. Sheridan, J.R. Williams, P.W. Marshall, R.A. Reed, Proton radiation effects in 4H-SiC diodes and MOS capacitors, IEEE Transactions on Nuclear Science, **51** (2004) 3748.

[38] F. Roccaforte, C. Bongiorno, F. La Via, V. Raineri, Tailoring the Ti⁄4H–SiC Schottky barrier by ion irradiation, Applied Physics Letters, **85** (2004) 6152.

[39] F. Nava, E. Vittone, P. Vanni, G. Verzellesi, P.G. Fuochi, C. Lanzieri, M. Glaser, Radiation tolerance of epitaxial silicon carbide detectors for electrons, protons and gamma-

rays, Nuclear Instruments and Methods in Physics Research Section A: Accelerators, Spectrometers, Detectors and Associated Equipment, **505** (2003) 645-655.

CHAPTER 8

Conclusions and future work

8.1 Electron Irradiation Conclusions

Electron irradiation was performed using a 546 keV Strontium source with a fluence rate of 6.8×10^{9} $cm^{-2}s^{-1}$ from fluence of 4.9×10^{13} cm^{-2}. The irradiations were done in steps of 2 hours to a total of 22 hours, corresponding to fluence of 5.4×10^{14} cm^{-2}. *I-V* results obtained during the electron irradiation process indicate that excellent SiC diode characteristics are retained. This is seen in the close to unity ideality factor values, unchanging SBH values, low reverse leakage current and low series resistance values, both before and after irradiation. Overall, the fabricated diodes had excellent current rectification of more than ten decades before irradiation, which was retained after electron irradiation. A low free carrier removal rate was obtained from *C-V* measurements. This was as a result of a small overall reduction of the free carrier concentration in the entire irradiation fluence range.

DLTS revealed the presence of four defect levels, $E_{0.10}$, $E_{0.12}$, $E_{0.18}$ and $E_{0.69}$ before the diodes were irradiated. After irradiation, three new energy levels were observed and these have been labelled as $E_{0.42}$, $E_{0.62}$ and $E_{0.76}$. All the irradiation induced defects were annealed out at temperatures below 500 °C. The concentration of level E0.69 remained high after annealing at 600 ° C compared to the values obtained before irradiation. Level $E_{0.10}$, a nitrogen impurity was completely suppressed by irradiation but was recovered after annealing at 500 °C. Levels $E_{0.12}$, and $E_{0.18}$ were not noticeably affected by electron irradiation.

8.2 Alpha particle irradiation conclusions

Alpha particle irradiation was done to fluence of 2.6×10^{10} cm^{-2} using 5.4 MeV alpha particles from an Am-241 radioactive source. Just as with electron irradiation, there was no marked degradation of the diodes as a result of irradiation. A reduction in the free carrier concentration was observed due to irradiation and some recovery was realised after annealing at 200 °C with no further recovery resulting from higher annealing temperatures of up to 600 °C. A large carrier removal rate, 15 819 cm^{-1} was obtained.

Alpha particle irradiation induced deep levels $E_{0.42}$ and $E_{0.76}$, which were also reported after electron irradiation. These two defects were however only observed clearly after annealing the irradiated diodes at 200 °C, and were annealed out at 400 °C. Levels $E_{0.10}$ and $E_{0.69}$ increased in concentration after irradiation while levels $E_{0.12}$, and $E_{0.18}$ were not noticeably affected by irradiation.

8.3 Proton irradiation conclusions

Proton irradiation was achieved by use of 1.6 MeV accelerated protons to fluence of 1×10^{12} cm^{-2}. A complete picture was not obtained from this study due to a high degree of compensation that resulted from the irradiation. As such, the diodes had to be annealed before taking measurements hence some vital information was lost through annealing. After annealing at 125 °C and higher temperatures, *I-V*, *C-V* and DLTS measurements were taken. A reduction in the diode rectification and a very high series resistance was observed. Significant rectification was attained through annealing up to 625 °C. Significant recovery in free carrier concentration was achieved after annealing at 625 °C.DLTS revealed a new defect level with activation energy E_C-0.31 eV after annealing the irradiated diodes at 425 °C. Levels $E_{0.42}$, $E_{0.62}$ and $E_{0.76}$ which were observed after electron and alpha particle irradiation were also present in proton irradiated diodes.

The defects resulting from electron, alpha particle and proton irradiation was found to be nearly the same, especially by comparing the defects induced by these irradiations. The radiation hardness of SiC was also seen in the low free carrier removal rates and low defect introduction rates, especially after electron irradiation. The SiC used in this study is of low doping concentration, 4×10^{14} cm^{-3}. Greater radiation hardness is even accepted from samples of a higher doping concentration.

8.4 Future work

- Little information was obtained from proton irradiation. It is important that more proton irradiation studies be conducted using several fluences so that values of free carrier removal rate and defect introduction rates can be obtained. One problem why these values were not obtained in this study is because the SiC samples used in the study were of very low doping density. It is therefore necessary to use samples of higher doping densities in such studies.
- It is also important to carry out similar studies as those done in this study but using SiC samples of varying doping densities. Values of doping dependent free carrier removal can then be obtained.
- The origin of most defects observed in this study remains speculated. It is important to apply other defect study techniques in order to have more understanding of the origin of these defects. These techniques include electron-paramagnetic resonance, transmission cathodoluminescence, positron annihilation, etc.